Numerical Simulation on the Urban Warming Induced by Land Use Modification during Recent 30 Years

Numerical Simulation on the Urban Warming Induced by Land Use Modification during Recent 30 Years

A Dissertation Submitted to
the Graduate School of Life and Environmental Sciences,
the University of Tsukuba
in Partial Fulfillment of the Requirements
for the Degree of Doctor of Philosophy in Science

Toshinori AOYAGI

Abstract

This dissertation figures out the local climate change (especially focusing on temperature change) induced by land use modifications during recent 30 years, utilizing the numerical atmospheric simulation technique.

Firstly, an urban multilayer radiation scheme was developed for the first step of this study in order to investigate how a three-dimensional structure such as an urban canyon can affect urban surface warming. The complete consideration of multiple scattering of shortwave and long-wave radiation using the radiosity method is an important feature of the present scheme. A brief description of this scheme is presented, followed by evaluations that compare its results with observations of the effective albedo and radiative temperature for urban blocks. Next, we calculate the urban surface warming potential (USWP), defined as the difference between the daily mean radiative temperature of urban surfaces including their canyon effects, and the daily mean temperature of a flat surface with the same material properties, under a radiative equilibrium state. Assuming standard material properties (albedo and emissivity of 0.4 and 0.9, respectively), we studied the sensitivity of the USWP to various aspect ratios of building heights to road widths. The results show that the temporally-averaged surface temperature of an urban area can be higher than that of a flat surface. In addition, we determined the overestimation of the effective temperature of urban surfaces induced by the overestimation of the radiation distribution to the walls when one uses a single-layer scheme for urban block arrays that have a low sky-view factor less than around 0.5.

Secondly, a single-layered square prism urban canopy (SPUC) scheme for the Japan Meteo-

rological Agency nonhydrostatic model (JMA-NHM) was developed. This scheme considers the urban canopy layer with square prism shaped buildings. The basic concept of this scheme is similar to that of the conventional energy balance models for an urban canyon structure. The scheme presented here, however, differs slightly from them in its representation of the bulk resistance circuit and some treatments of radiation processes as well as by considering the water reservoir on building surfaces. A comparison between the SPUC scheme and the existing slab scheme of the JMA-NHM was made on summer days in the Tokyo Metropolitan area. The SPUC run more accurately reproduced the expected behavior of the urban canopy effect than did the slab run. The effective albedo was smaller in the SPUC run than in the slab run (the upward shortwave radiation of the SPUC run was smaller than that of the slab run). The heat fluxes in the SPUC run, however, showed worse performances. Adequate parameter settings (especially concerning latent heat fluxes) are needed in the SPUC run. The mean bias errors of the surface air temperature during nighttime were less negative and slightly improved in the SPUC run than in the slab run.

Finally, the warming trend in Kanto-Koshin area during a 30-year period (1976-2006) was estimated. The warming trends at AMeDAS stations were estimated to a little less than 1.3 $^{\circ}$ C / 30 years as seasonal averages in both summer and winter. These warming trends were considered to include the trends of large-scale and local-scale warming effects. Because a regional climate model with 20-km resolution without any urban parameterization could not well express the observed warming trends and their daily variations, we investigated whether a mesoscale atmospheric model with an urban canopy scheme could express them. To make the simulations realistic, we used 3 sets of real data: National Land Numerical Information datasets for the estimation of the land use area fractions, anthropogenic heat datasets varying in space and time, and GIS datasets of building shapes in the Tokyo Metropolis for the setting of building aspect ratios. The time integrations over 2 months were executed for both summer and winter. A certain level of correlation was found between the simulated temperature rises and the observed warming trends at the AMeDAS stations. The daily variation of the temperature rises in urban grids

was higher at night than in the daytime, and its range was larger in winter than in summer. Such tendencies were consistent with the observational results. From additional sensitivity analyses, we figured out the classic and some unexpected features of urban warming, as follows: (1) Land use distribution change (mainly caused by the decrease of vegetation cover) had the largest daytime warming effect, and the effect was larger in summer than in winter; (2) anthropogenic heat had a warming effect with 2 small peaks owing to the daily variation of the released heat and the timing of stable atmospheric layer formation; and (3) increased building height was the largest factor contributing to the temperature rises, with a single peak in early morning.

Keywords: Urban warming, Radiative equilibrium, Radiosity method, Mesoscale model, Urban canopy, Urbanization, Land use, Anthropogenic heat

Contents

List of Tables

List of Figures

Chapter 1

Introduction

"Human activity changes climate" is a common phrase, recently. In terms of the global climate, there are undeniable facts like the destruction of the polar ozone layer induced by the anthropogenic enormous emission of chlorofluorocarbon gases, and the global warming trends attributing to increasing emission of carbon dioxide. As for the continental scale, it is well known that the expansion of semiarid land area induced by the excess grazing at Mongolia causes the increase of dust emission to the free atmosphere and it may affect the growth of yellow sand phenomena ('Kosa' in Japanese) frequency in the leeward Japan. The influences of anthropogenic aerosol emission caused by the rapid industrial development in China should influence the atmospheric quality and total radiation modification in Japan.

The climate changes induced by human activities can be felt easily in the more immediate local and micro climatic sense than such larger scales. The influences of urbanization on the abnormally high temperature in summer days and active convections over urban area, which have attracted attention in recent years, are good examples.

1.1 Urban Warming

The 'urban warming', which is the positive temperature trend that accompanies urbanization (determined from long-term observations at the same observatory), has recently attracted attention although the concept of the 'urban heat island', which reflects the temperature difference between urban and rural areas, is widespread in urban climate studies. Fujibe (2009) estimated the urban warming rate of the annual mean temperature at Tokyo, the most urbanized city in Japan, to be 3.1 °C century^{-1} by using observational data from 1906 to 2006. This trend is notably larger than for non-urbanized areas; for example, the trend is about 0.6 °C century^{-1} at Hachijo Island, 300 km south of Tokyo. Such larger trends in urbanized cities can be explained by the causes of heat island phenomena, on which many urban climate studies have targeted (see Arnfield (2003) and Kanda (2007) for organized reviews). It is easy to imagine that such local and micro climate changes will be mainly caused by the modifications of the lower boundary layers, in particular, the significant modification of land surfaces. Although there is no doubt that the increase of anthropogenic heat release is one of the major factors, urban morphological change is also an important factor in urban warming. Other factors such as thermal admittance and Bowen ratio change, however, are considered to be less important because the dominant land use type has already been urban surfaces in big cities for decades.

1.2 Radiative Effect of Urban Morphological Change on Urban Warming

As Grimmond et al. (2010) mentioned, the consideration of urban morphology provides better performance for reproducing urban energy balances. There are two main effects of urban morphology. One is the radiation distribution, which is an important factor for the estimation of net radiation on urban surfaces. The other is the change of momentum and heat fluxes from the urban surfaces (Ratti et al. 2002; 2006). Although these effects are complexly intertwined, Johnson et al. (1991) and Oke et al. (1991) succeeded independently in determining the radiative

effects on the heat island intensity assuming an idealized no-wind condition, i.e., no fluxes from the surfaces. Along with their supposition, in this study, we try to extract the radiative change effect on urban warming. In analogy to their 'maximum heat island intensity', we propose a new index called the 'urban surface warming potential' (USWP), which is the differential between the daily mean radiative temperature of urban surfaces and that of flat surfaces composed of the same material with the urban surfaces at an equilibrium state produced only by radiation balances. The USWP can be used as an index of the theoretical maximum warming rate. For the USWP estimation, the estimations of effective albedo and effective emissivity induced by urban morphology are critical. To estimate such radiative effects, a sophisticated radiation scheme is used. Multiple scattering of both short- and longwave radiation and radiative energy conservation must be considered. Multi-layered walls in the vertical direction are needed if very deep urban canyons are considered.

Regarding shortwave radiation, Aida and Gotoh (1982) built a simple canyon model to investigate radiative modifications in urban canyons and showed that the albedo decrease in an urban setting was caused by multiple reflections of incident radiation between canyon walls or between a canyon wall and the bottom surface. In recent years more accurate calculations of shortwave interactions between urban surfaces have become available as the computational environment has improved. Using refined urban radiation models, Kondo et al. (2001) and Kawai and Kanda (2003) calculated effective albedo for various three-dimensional urban geometries. Their calculated values were consistent with the observed values of Aida (1982) . Kanda et al. (2005b) also developed a simple model that calculates radiative interactions for regularly arranged buildings, which showed good performance for the reproduction of effective albedo. As for longwave radiation, Oke et al. (1991) simulated a nighttime heat island using an urban radiation model developed by Johnson et al. (1991) . They concluded that an urban radiation model must represent the urban/rural difference in the sky-view factor at the ground so as to reproduce the surface urban heat island at night if the model includes processes of longwave interactions between urban walls and the ground. On the other hand, for a larger view of urban surfaces,

Kobayashi and Takamura (1994) showed with their Monte Carlo simulation model that multiple reflections of longwave radiation between urban surfaces tend to increase upward longwave radiation emissions at the top of the urban canyon as compared to a flat surface if the material of the surfaces is not black. Although other urban radiation schemes that consider both short- and longwave radiation have been proposed by Sakakibara (1996) , Masson (2000) , Kusaka et al. (2001) , Martilli et al. (2002) , and so on, these schemes treat limited multiple reflections or simple single-layer urban walls.

Against this background, Oliveira Panão et al. (2007) proposed a matrix calculation technique for solving the short- and longwave net radiative balance of a 3-d urban structure. Their model was based on the radiosity method, which was formerly applied to 2-d infinitely long urban canyon systems by Harman et al. (2004) , and was able to calculate the exact net radiation flux by taking an infinite number of multiple reflections into consideration. They also demonstrated that the matrix method greatly reduces the calculation time because it separates time dependent variable vectors and time independent coefficient matrices. They used the method to calculate the effective albedo and effective emissivity of urban blocks, and their evaluated effective albedo was in good agreement with field data of Aida (1982) . They also calculated the increase of emissivity in the urban system. Their scheme is very suitable for the present study because of its full consideration of multiple scattering and complete treatment of radiative energy conservation.

1.3 Urban Canopy Parameterization for a Mesoscale Atmospheric Model

The representation of urban surfaces in mesoscale model is traditionally achieved by setting a smaller albedo for roads, larger thermal capacity or thermal inertia, and smaller soil water content as compared with values for vegetation surfaces. This approach has been successfully employed in operational numerical weather prediction models (Best 2005 ; Liu et al. 2006 ; Saito et al. 2006). By considering anthropogenic heat release, the additional heat flux to the atmosphere can

be added to the model with distribution representing populations and human activities. However, in order to express the complexity of radiation distribution and flux circuits among the various surfaces in a landscape of buildings, it is necessary to utilize the concept of urban canopy scheme of at least single-layered one (Masson 2000 ; Kusaka et al. 2001). As the resolution of the mesoscale model increases, urban canopy schemes are expected to more accurately represent the thermal and radiative environment inside the urban canyon.

Several urban canopy schemes were previously proposed for incorporation into mesoscale models, including an urban tile scheme for the operational numerical weather prediction model of the U.K. Met Office (Best 2005), a town energy balance by Masson (2000) for Meso-NH (Lemonsu and Masson 2002), a simple single-layer urban canopy model by Kusaka et al. (2001) for the Weather Research and Forecasting model (WRF), and an urban parameterization scheme by Martilli et al. (2002) for MM5 (Dupont et al. 2004 ; Otte et al. 2004) and WRF (Chen et al. 2010). Some of the schemes have been compared and validated based on in situ observation of the street canyons of some cities, such as Mexico City, Vancouver, and Marseille (Masson et al. 2002 ; Lemonsu et al. 2004 ; Dupont and Mestayer 2006 ; Hamdi and Schayes 2007). As for the validation study based on the Vancouver data, Grimmond et al. (2010) recently wrote up the results of an international urban model comparison gathering up 33 urban parameterization schemes. Those comparative experiments were performed using off-line land surface models and showed good agreement with observational results with respect to radiation balance and surface energy balance. However, there are relatively few reports on the evaluation of schemes coupled with mesoscale atmospheric models. On the basis of a 2-year simulation, Best (2005) reported the reduction of bias and root mean square errors of temperature by using an urban parameterization scheme with the Met Office operational mesoscale model, that is a limited area version of the Unified Model (Cullen 1993). Holt and Pullen (2006) performed a 1-month simulation using a WRF model coupled with the single- and multi-layer urban canopy schemes of Kusaka et al. (2001) and Brown and Williams (1998) respectively and compared the results with observational data from around the New York City Metropolitan area. Dupont et al. (2004) compared three

schemes (roughness approach slab scheme, roughness approach mosaic surface scheme including an urban canopy scheme of single-layered, and drag-force approach mosaic surface scheme including a multi-layer urban canopy scheme) with observational data above Philadelphia, in Pennsylvania, U.S.A. Zhang et al. (2008) recently tried to attach simple urban canopy model of Kusaka et al. (2001) to the Regional Atmospheric Modeling System (RAMS) and checked reproduction of heat island intensities in China. Although the last two reports validated the surface air temperature and calculated the root mean square errors, the evaluation spanned only a few days.

The effect of urbanization on local meteorological phenomena has been the subject of much research in Japan. For example, studies have examined the effect of the heat island on rising trends of surface air temperature (Fujibe 2009) and the effect of urbanization on rainfall events (Kanae et al. 2004 ; Fujibe et al. 2005). Several previous numerical studies attempted to reproduce the urbanization effects of the Tokyo Metropolitan area. Kondo et al. (2005) reproduced the daily changes of surface air temperature and surface winds by coupling a multi-layer urban canopy scheme to their mesoscale model. Matheson and Ashie (2008) tried to estimate the effect of urbanization on rainfall events around the Tokyo Metropolitan area, using their mesoscale model called the Local Circulation Assessment and Prediction System (LOCALS) whose urban land surface scheme was a simple slab type. Their case studies suggested that urbanization can increase or decrease rainfall in urban area depending on the surrounding atmospheric conditions. They also mentioned in their conclusions that the urban canopy parameterization is needed in order to improve lower biases of surface air temperature during the nighttime. Recently, Kusaka et al. (2009) just performed three August simulations on 2002, 2003, and 2004 with WRF using their urban canopy model for the Tokyo Metropolitan area and they showed the potential usage of urban canopy scheme for the climatic simulations.

The Japan Meteorological Agency nonhydrostatic model (JMA-NHM) is also an effective tool for both operational numerical weather prediction (Saito et al. 2006) and regional climate modeling in the framework of a climate change study (Sasaki and Kurihara 2008). The JMA-NHM has been used in a wide range of studies including hi-resolution simulation (Seino et al.

2004 ; Mashiko et al. 2009), and thus application to urban modeling is expected. However it has not contained so far any parameterization scheme for stereoscopic urban canopy structures. The implementation of at least single-layered urban canopy scheme to the JMA-NHM is increasingly needed for urban climate researches in Japan.

As mentioned above, there have already been several single-layered urban parameterization schemes attached to mesoscale models. Most of the schemes were designed for two-dimensional infinitely long street canyons. Meanwhile, an urban parameterization scheme considering rather three dimensional morphology of buildings is more suitable than the two-dimensional schemes for cities like Tokyo metropolitan area, where urban landscape comprises buildings with various shapes and heights. The scheme of Kanda et al. (2005a) was designed for ideal cubic concrete blocks and was validated with the outdoor scale model called COSMO. However some part of them can be simplified and some part shall be extended for the mesoscale models. Incorporating the direction of a building's four walls is not necessary in a mesoscale model, because the orientations of building walls at the mesoscale grid size (around several kilometers) can be considered random. The reduction of facets has some advantages on the computational costs because the facets have some layers to solve heat conduction equations. The simpler calculation of shortwave radiation, i.e., estimation of shading patterns, is preferable because the calculation will be operated on nearly each time steps. On the other hand, water availabilities from roof and wall should be extendedly considered in the evaporation process when we use the scheme under any weather conditions including cloudy and rainy cases.

1.4 Surface Air Temperature Trends during 30 years

Surface air temperature warming trends derived from long-term observations in Japan are well known. The trends reflect the global warming baseline shift, but the magnitude of the shift, especially in urban areas, is obviously larger than expected. The excess magnitude is attributed to the so-called urbanization effect, that is, an effect of human activities. Recently, Fujibe (2009) es-

timated urban warming trends over 27 years (from 1979 to 2006) by using observational data from the Automated Meteorological Data Acquisition System (AMeDAS). The study showed that annual mean temperature warming trends ranged from approximately 0.3°C per decade (at AMeDAS observatories surrounded by the smallest population densities) to 0.5°C per decade (at observatories with the largest densities). This analysis suggests an association between urban temperature trends and human activities.

As shown by Fujibe (2010) in a review of urban warming in Japanese cities, the warming effects of urban surfaces are more apparent at night, in particular during the cold season, corresponding to a low mixing depth in the stable surface layer. During the past few decades, however, studies of urban climatology in Japan have taken a strong interest in the midsummer heat load of cities because of its association with an increased risk of heat stroke. He also observed that the region having the greatest temperature increase (more than 1°C per 30 years) in the summer extended from the vicinity of Tokyo to the northwestern corner of the Kanto Plain. This result is consistent with the findings of a decrease in daytime pressure at the center of the Kanto Plain and a shift of wind direction toward the area of lower pressure (Fujibe 1994 , 2003).

Besides observational research, simulation studies of urban climatology have been performed. Using their local climate model, Kimura and Takahashi (1991) assessed the effects of anthropogenic heat load and land use modification from vegetation to urban surfaces on the surface air temperature in the Kanto Plain. Their simulation was performed under atmospheric conditions averaging 36 typical clear summer days. The temperature rise induced by the addition of anthropogenic heat and the modification of land use was estimated to be approximately 3°C (nighttime) and 1°C (daytime) at the center of the Tokyo Metropolitan area. They concluded that the anthropogenic heat load is the main cause of nighttime warming and diminished vegetation is the primary cause of the temperature rise during the daytime. Ichinose et al. (1999) also conducted a numerical simulation with a more detailed and realistic distribution of the anthropogenic heat. Their simulation showed that the surface air temperature could rise by about 1.5°C on a summer day and by about 2.5°C on a winter day, peaking at late evening at the center grid of the heat

distribution.

Kusaka et al. (2000) provided 3 different bottom boundary conditions for their mesoscale model by using land use information from 1900, 1950, and 1985. After performing some sensitivity experiments using the 3 land use scenarios under typical summer atmospheric conditions, they estimated that the warming bias might be about 2 - 3°C over 85 years (1990 - 1985) and about 1 - 2 °C over the later 35 years (1950 - 1985). They also noted that the warm bias areas were distributed around the outer part but not in the center of the Tokyo Metropolitan area.

Kusaka and Kimura (2004a, b) estimated urban canyon effects, such as redistribution of radiation, heat transfers among surfaces in the canyon, and reduction of wind speeds inside the canopy layer, using their 2-dimensional atmospheric model to which they coupled their urban canopy model (Kusaka et al. 2001) . The results of their simulation showed that urban warming could occur by only the canyon effects of urban buildings.

These earlier numerical studies on urban warming succeeded as a sort of sensitivity analysis. Their simulations, however, were carried out under idealized or other clear and calm atmospheric conditions. Therefore, a simple comparison cannot be made between such warming bias predictions and observational temperature trends of the real atmosphere, in which many atmospheric phenomena can occur. The surface changes must be sensitive to the weather conditions. Furthermore, there are possible interactions between urban surfaces and meteorological phenomena, such as cloud generation caused by the urban heat load (Inoue and Kimura 2004, 2007) .

To estimate the sensitivity of land surface modification to urban warming effects more accurately, reproduction experiments with increased realism have recently been employed that use mesoscale models incorporating the concept of urban canopy energy balances coupled to their land surface schemes. Numerical simulations using cloud resolving non-hydrostatic models are mainly performed with realistic initial and boundary conditions based on reanalysis data. Kusaka et al. (2009) tried to reproduce the summer meteorological fields of 2002, 2003, and 2004 by targeting the Weather Research and Forecast model (WRF) onto the Kanto area, and they showed the availability of the WRF model to climatic research. Adachi and Kimura (2010) researched

the urban effects of 10 years of land use modification (from 1987 to 1997) on the nighttime temperatures of cities in the Kanto Plain by conducting simulation with their Terrestrial Environment Research Center version of the Regional Atmospheric Modeling System (TERC-RAMS). They conducted the TERC-RAMS simulations with experimental matrices under the following conditions: 2 surface boundary conditions of 1987 and 1997, 2 atmospheric boundary conditions of the 1980's and 1990's downscaled from Japanese re-analysis (JRA-25) datasets (Onogi et al. 2007) , and atmospheric conditions derived by the pseudo-global warming downscaling method (Kawase et al. 2009) . They pointed out that urban warming during the nighttime (0200 - 0400 LST) in August from 1987 to 1997 might be about 0.3 - 0.4 °C around the center of the Tokyo Metropolitan area. Hara et al. (2010) checked the sensitivity of the atmospheric stability, which will change after global warming, to the urban heat island intensity in winter by a numerical simulation with the WRF model. They showed that the nighttime urban heat island will grow on average in winter as the atmosphere becomes more stratified by future global warming. Although their interest was in the relationship between global warming and the urban heat island, their research showed that the WRF system can be applied to urban climate research on wintertime effects.

Likewise, our intention will be to reproduce the urban warming potential caused by urban growth in recent decades by numerical simulations with our non-hydrostatic atmospheric model. In this paper, we compare the results with observed temperature trends. For a more consistent comparison, we use land use information from the years corresponding to the observational dataset. After evaluating the reproducibility and checking the limitation of the reproduction, we perform some classic sensitivity studies of urban effects, that is, the effects of decreased vegetation area, anthropogenic heat load, and the structural change of urban building canopies.

1.5 Objectives

The overall objective of this study is to figure out how the climatic meteorological fields will be changed by the artificial modification of land surfaces. We will try to figure out the effect of

land surface modification onto the local climate change especially focused on the seasonal mean temperature change, taking great advantages of numerical simulation techniques. The numerical modeling techniques will be used throughout this study. And checking the availability of those methods onto the local climate researches is another objective of this study.

Firstly, focus will be on the surface warming potential induced by the 3-d morphology of urban buildings. A possibility of surface temperature rise only attributed to the 3-dimensional morphology changes will be shown, assuming an ideal situation of the building groups. In order to estimate the changes of radiation balance among the urban building canyons, an urban multilayer radiation scheme will be developed. Using this scheme and some other equations, the relationship between 3-d morphological parameter and the urban surface warming potential will be figured out (Chapter 2).

Secondly in Chapter 3, an urban energy balance scheme, a square prism urban canopy scheme (SPUC), which can express explicitly the radiation and heat budget changes resulting from the morphologies of the urban buildings will be developed and coupled to a mesoscale atmospheric model. Reproduction skills by this newly urban energy balance scheme will be checked in this chapter.

Using this SPUC coupled JMA-NHM, some sensitivity analyses on the urban warming trends affected by the land use changes during this 30 years will be done. The reproducibility of the warming trends comparing the simulation result with the trends derived by observations will be checked. The final goal of this study is set to make the mechanism of urban warming clear by employing further sensitivity studies, taking advantages of the numerical simulations.

Chapter 2

Urban Surface Warming Potential Estimated by an Urban Multilayer Radiation Scheme

2.1 Urban Multilayer Radiation Scheme

The aim of this chapter is to determine the maximum temperature increase induced only by radiative distribution changes caused by the 'Manhattanization' of urban buildings. To estimate the effects of radiation modifications, a precise radiation scheme that considers full multiple scattering is essential. Some previous studies using the radiosity method (e.g., Sparrow and Cess 1978) have considered full scattering among the surfaces inside an enclosed system and can be applied to 2-d canyons (Harman et al. 2004) and 3-d canopy-like surfaces (Oliveira Panão et al. 2007) imitating real urban buildings. We also apply this method in the present study. Other equations specifying the typical time series of incident direct and diffuse solar radiation, solar zenith angles, etc. are needed to estimate the time evolution of surface temperatures. A heat conduction equation is also needed to forecast the time evolution of the temperatures of surfaces and materials inside each element. Figure 2.1 shows a schematic flow chart of a model combining these schemes.

In this section, we first define surface system configurations that mimic the urban forest of

buildings. Next, the configuration factor that relates each element to the others is explained. This is followed by a brief review of the equations used to estimate the net radiation at each surface with the radiosity method using a matrix approach along with brief explanations of the equations for incident solar radiation and heat conduction to the materials.

2.1.1 Urban Block Configuration

By simulating 3-d surfaces that imitate forests of buildings in real cities, we try to estimate the radiative effects of the surface morphological changes on the average surface temperature. There are roughly two series of imitative configurations used in former studies: 2-d street canyons (Johnson et al. 1981; Arnfield 1982; Martilli et al. 2002; Harman et al. 2004) and 3-d cubic or square prism-like canopies (Kobayashi and Takamura 1994 ; Kanda et al. 2005a, b ; Kondo et al. 2005; Ikeda and Kusaka 2010). The important observational result of Aida (1982) showed that a decrease of effective albedo in a 3-d block system is more significant than in a 2-d canyon system in spite of the former's smaller plane area ratio. Furthermore, anticipating that the radiation scheme developed in this study will be used by recent 3-d urban canopy energy balance models, we select a 3-d one in which identical buildings and streets are regularly arranged (Fig.2.2a).

The cross section of each building is assumed to be a square with width B, the road width is W, and the height of each building is H. The building walls are divided into k vertical layers (Fig.2.2b). We simplified the scheme by considering that the differences among the four walls facing north, east, south, and west can be neglected by assuming that the solar radiation incident to each wall is equal to the average over all solar azimuth angles. Ikeda and Kusaka (2010) recently compared two multilayer urban canopy models, one that takes all four walls of a building separately into consideration and one that uses an average of the four azimuthal faces. The difference between the simulated results of the two models was small, which suggests that the assumption of an average wall works well.

Finally, the energy budget and prediction of the surface temperature are evaluated at k points

on the building wall, one point on the street surface, and one point on the building roof. If we consider a sufficient quantity of building units (Fig.2.2b) to be regularly arranged like Fig.2.2a, the wall elements, ground element, roof element, and sky area element covering the surfaces can be considered to comprise one enclosed system, and we can apply the radiosity method to this urban block configuration.

2.1.2 Configuration Factors

The configuration factor is a very useful concept for considering radiation transfers among plane surfaces in an enclosure. Suppose B_j is the outgoing diffuse radiation from a surface element j. Then Λ_i, the total incoming radiative flux density onto the surface element i, can be estimated using f_{ij}, the configuration factor from element i to j, as

$$\Lambda_i = \sum_{j=1}^{k+3} f_{ij} B_j, \tag{2.1}$$

where the subscripts i, j denote a total of k + 3 elements, namely, the wall elements 1, ..., k, ground element g, roof element r, and sky element s. The so-called 'sky-view factor' is defined in this study as the configuration factor from the ground to the sky, and is denoted by f_{gs}. We can describe this relation in a matrix-vector expression by

$$\vec{\Lambda} = \mathbf{F}\vec{B}, \tag{2.2}$$

where $\vec{\Lambda}$ and $\vec{B}$ are radiative flux density vectors and the matrix $\mathbf{F}$ is a configuration factor matrix with $(k+3)^2$ matrix elements of configuration factors from and to each element. The configuration

factor matrix **F** can be explicitly described as

$$\mathbf{F} = \begin{pmatrix} f_{11} & \cdots & f_{1k} & f_{1g} & f_{1r} & f_{1s} \\ \vdots & \ddots & \vdots & \vdots & \vdots & \vdots \\ f_{k1} & \cdots & f_{kk} & f_{kg} & f_{kr} & f_{ks} \\ f_{g1} & \cdots & f_{gk} & f_{gg} & f_{gr} & f_{gs} \\ f_{r1} & \cdots & f_{rk} & f_{rg} & f_{rr} & f_{rs} \\ f_{s1} & \cdots & f_{sk} & f_{sg} & f_{sr} & f_{ss} \end{pmatrix}. \tag{2.3}$$

2.1.3 Calculation of th Configuration Factors

Although there are $(k + 3)^2$ components in the configuration factor matrix **F**, some of the values are fairly obvious, such as $f_{1r} = f_{2r} = \ldots = f_{kr} = f_{gr} = 0$, $f_{gg} = f_{rr} = f_{ss} = 0$, and $f_{rs} = 1$. The reciprocity law $A_i f_{ij} = A_j f_{ji}$ is also useful for calculating the diagonal elements of the configuration factors, where A_i is the area of element i, because the area of the wall elements is equal in this study, therefore $f_{ij} = f_{ji} (i, j = 1, 2, \ldots, k)$. To calculate the configuration factors between wall elements, one can imagine that the configuration factors among the wall elements are the same if the differences of the levels of wall layers are the same. Thus, the relationship $f_{ij} = f_{1(1+|i-j|)}$ can be applied, for example, $f_{21} = f_{12}$, $f_{22} = f_{11}$, $f_{23} = f_{12}$, $f_{24} = f_{13}$, and so on. This relationship means that we can easily determine configuration factors among all the wall elements once we obtain the configuration factors from the lowest layer to the other wall elements.

The summation of configuration factors from one element to all elements equals 1, which is also useful because the configuration factor from the lowest wall element can be estimated by

$$f_{1g} = \frac{1 - f_{11}}{2}. \tag{2.4}$$

Figure 2.3a shows a viewing image horizontally from the wall center, in which the block

arrays are constructed by only one-layer height blocks. The ground and the sky can be seen as the same configurations although they flip vertical. Thus the summation of configuration factors can be described as $f_{11} + 2f_{1g}$ and this summation equals 1. Figure 2.3b shows a viewing image horizontally from the center of second layer ($i = 2$) of a block array constructed by two-layer blocks (k = 2). We can see the elements of the sky, the second layer itself, the lowest element of the wall, and the ground. The configuration factors of these elements can be estimated as $(1 - f_{11})/2$, $f_{22}(= f_{11})$, $f_{21}(= f_{12})$, and f_{2g}, respectively. The configuration factor from the second layer of the wall to the ground can then be described as

$$\begin{aligned} f_{2g} &= 1 - \frac{1 - f_{11}}{2} - f_{22} - f_{21} \\ &= \frac{1 + f_{11}}{2} - \sum_{j=1}^{2} f_{1j}. \end{aligned} \tag{2.5}$$

The configuration factor can be derived only from the factors from the lowest wall element to the other wall elements. If we apply this relationship to the other layers, the configuration factors from element i to the ground f_{ig} can be derived by

$$f_{ig} = \frac{1 + f_{11}}{2} - \sum_{j=1}^{i} f_{1j}. \tag{2.6}$$

Analytical solutions between small patched elements are used to estimate the configuration factors in this study. Setting up a coordinate system as shown in Fig.2.4, we divided one wall into smaller elements along the x-axis and evaluated whether the faces of the next 10 blocks in the x and y directions can be seen from the small element. For each visible area, we then calculate and sum up configuration factors from the small element to every parallel and perpendicular faces with analytical solution (Siegel and Howell 1981) . Distances and shift lengths in horizontal direction between the small element and the faces are calculated using coordinate values, for examples in the figure, the position of the small element (x_0, y_0), the edge positions of the parallel face (X_1, Y_1) and (X_2, Y_1), the edge positions of the perpendicular face (X_3, Y_3) and (X_3, Y_4). Shift

lengths in vertical direction between the small element and the faces are estimated by height of wall layer and the layer numbers i and j of the small element and the faces, respectively. Finally, we average these values for every small element in the x direction.

2.1.4 Net Radiation on Surfaces

Solutions of radiation exchange in an enclosure composed of diffuse-grey surfaces are well known as the radiosity method (Sparrow and Cess 1978) and the net-radiation method (Siegel and Howell 1981) . Previous studies have applied these methods to urban imitated surfaces (Harman et al. 2004 ; Oliveira Panao et al. 2007). In this section, brief explanations of the radiation scheme of this study using matrix expressions based on these previous studies are presented.

When we use the radiosity method in the shortwave range, we distinguish direct and diffuse components of the solar radiation because the radiosity method treats radiation exchanges among diffusive surfaces in an enclosure. Suppose that K_i is the direct component of the solar radiation to the surface element i and let $\vec{\Omega}_{S0}$ denote a vector whose components are K_l, K_2, $\cdots$, K_k, K_g, K_r,

$$\vec{\Omega}_{S0} = \begin{pmatrix} K_l & \cdots & K_k & K_g & K_r & 0 \end{pmatrix}^T . \tag{2.7}$$

We assume that this direct radiation will be reflected at each surface and become diffused light after the first reflection. Then we can define a diffuse shortwave radiation vector $\vec{\Omega}_{S1}$ expressing the initially emitted diffused light from each surface as

$$\vec{\Omega}_{S1} = \begin{pmatrix} \alpha_l K_l & \cdots & \alpha_k K_k & \alpha_g K_g & \alpha_r K_r & D \end{pmatrix}^T , \tag{2.8}$$

where α_i represents the albedo of surface i and D denotes the diffuse shortwave radiation from the sky. Taking this diffuse radiation vector $\vec{\Omega}_{S1}$ into account, we can estimate the effects of full multiple reflections by using the radiosity method.

Let vectors $\vec{\Lambda}_S$ and $\vec{B}_S$ denote the diffuse solar radiation going into and out from the surface

elements. Then the vector $\vec{B}_S$ can be described with the initial radiation $\vec{\Omega}_{S1}$ and the reflected amount of incoming diffuse radiation $\vec{\Lambda}_S$ as

$$\vec{B}_S = \vec{\Omega}_{S1} + \mathbf{A}\vec{\Lambda}_S, \tag{2.9}$$

where the matrix **A** is a diagonal matrix having albedo α_i of surface i as its diagonal elements except for the sky element:

$$\mathbf{A} \equiv \begin{pmatrix} \alpha_1 & & & & & \\ & \ddots & & & & \\ & & \alpha_k & & & \\ & & & \alpha_g & & \\ & & & & \alpha_r & \\ & & & & & 0 \end{pmatrix}. \tag{2.10}$$

Substituting the relationship of $\vec{\Lambda}_S = \mathbf{F}\vec{B}_S$ into Eq. (2.9) and rearranging $\vec{B}_S$, we can obtain an equation to estimate the outgoing radiation flux density including the infinite scattering of diffuse light among the surfaces in the enclosure:

$$\vec{B}_S = (\mathbf{I} - \mathbf{AF})^{-1}\,\vec{\Omega}_{S1}, \tag{2.11}$$

where the matrix **I** is the unit matrix. Finally, the net shortwave radiation flux density vector $\vec{\Phi}_S$ considering the direct component of solar radiation is obtained by

$$\begin{aligned} \vec{\Phi}_S &= \vec{\Omega}_{S0} + \vec{\Lambda}_S - \vec{B}_S \\ &= \vec{\Omega}_{S0} + (\mathbf{F} - \mathbf{I})\vec{B}_S \\ &= \vec{\Omega}_{S0} + (\mathbf{F} - \mathbf{I})(\mathbf{I} - \mathbf{AF})^{-1}\vec{\Omega}_{S1}. \end{aligned} \tag{2.12}$$

The components of the shortwave irradiation vectors, $\vec{\Omega}_{S0}$ and $\vec{\Omega}_{S1}$, should be calculated at every time step because the shadow area fraction is dependent on the solar zenith angle. We used the vector-tracing method to estimate the irradiation vectors.

For the longwave range, we define the initial irradiation vector $\vec{\Omega}_L$ as

$$\vec{\Omega}_L = \left(\epsilon_1 \sigma T_1^4 \quad \cdots \quad \epsilon_k \sigma T_k^4 \quad \epsilon_g \sigma T_g^4 \quad \epsilon_r \sigma T_r^4 \quad L \right)^T, \tag{2.13}$$

where ϵ_i and T_i represent the emissivity and surface temperature of surface i, respectively, σ is the Stephen-Boltzmann constant, and L denotes the downward longwave radiation from the sky.

Let us denote the longwave radiation going into and out from the surface elements as $\vec{\Lambda}_L$ and $\vec{B}_L$. The vector $\vec{B}_L$ can be expressed with the initial irradiation vector $\vec{\Omega}_L$ and the scattered amount of incoming $\vec{\Lambda}_L$ as

$$\vec{B}_L = \vec{\Omega}_L + (\mathbf{I} - \mathbf{E})\vec{\Lambda}_L, \tag{2.14}$$

where the matrix $\mathbf{E}$ is a diagonal matrix having as elements the emissivity ϵ_i of surface i and the unit value for the sky:

$$\mathbf{E} \equiv \begin{pmatrix} \epsilon_1 & & & & & \\ & \ddots & & & & \\ & & \epsilon_k & & & \\ & & & \epsilon_g & & \\ & & & & \epsilon_r & \\ & & & & & 1 \end{pmatrix}. \tag{2.15}$$

In the same manner as the shortwave range case, we substitute the relationship $\vec{\Lambda}_L = \mathbf{F}\vec{B}_L$ into Eq. (2.14) and rearrange $\vec{B}_L$ to obtain

$$\vec{B}_L = [\mathbf{I} - (\mathbf{I} - \mathbf{E})\mathbf{F}]^{-1} \vec{\Omega}_L. \tag{2.16}$$

Then, the net longwave radiation flux density vector $\vec{\Phi}_L$ can be obtained by

$$\begin{aligned}\vec{\Phi}_L &= \vec{\Lambda}_L - \vec{B}_L \\ &= (\mathbf{F} - \mathbf{I})\,[\mathbf{I} - (\mathbf{I} - \mathbf{E})\mathbf{F}]^{-1}\,\vec{\Omega}_L \end{aligned} \tag{2.17}$$

The translation matrix from $\vec{\Omega}_L$ to $\vec{\Phi}_L$ in Eq. (2.17) contains only three time independent matrices: the configuration factor matrix **F**, the emissivity matrix **E**, and the unit matrix **I**. From these, we could easily estimate the net longwave radiation vector $\vec{\Phi}_L$ if we determined **F** and **E** in the first step of the simulation.

2.1.5 Incident Solar Radiation

A typical time series of solar radiation is needed to estimate radiation transfer among the surfaces inside the urban canyon. The incident angle of direct solar radiation determines the shortwave radiation distribution to each surface element. The ratio of direct to diffuse solar radiation is also one of the important factors for the estimation of effective albedo. The solar zenith angle θ is given by

$$\cos\theta = \cos\omega\cos\delta\cos\phi + \sin\delta\sin\phi, \tag{2.18}$$

where ω represents the hour angle of the true solar time, δ is the declination of the sun, and ϕ is latitude. The hour angle ω can be approximated by using the day of the year d_y from the

equations

$$\zeta \equiv \frac{2\pi}{365}\left(d_y - 1\right), \tag{2.19}$$

$$\begin{aligned} ET =& 0.000075 \\ &+ 0.001868\cos\zeta - 0.032077\sin\zeta \\ &- 0.014615\cos 2\zeta - 0.040849\sin 2\zeta, \end{aligned} \tag{2.20}$$

$$\omega = \frac{(JST - 12)\pi}{12} + \frac{(\eta - \eta_0)\pi}{180} + ET, \tag{2.21}$$

where ζ is the fractional day of the year (in radians), ET is the equation of time (in radians), JST is Japan Standard Time, and η and η_0 are the longitudes (in degrees) of the location and the JST meridian. The declination of the sun δ can be determined from the fractional day of the year ζ by

$$\begin{aligned} \delta =& 0.006918 \\ &- 0.399912\cos\zeta + 0.070257\sin\zeta \\ &- 0.006758\cos 2\zeta + 0.000907\sin 2\zeta \\ &- 0.002697\cos 3\zeta + 0.001480\sin 3\zeta. \end{aligned} \tag{2.22}$$

The global solar radiation G, direct solar radiation K, and diffuse solar radiation D are given by the following semi-experimental relations as described in Oliveira Panão et al. (2007) :

$$G = I_0(0.929 - 0.041T_L)(\cos\theta)^{\frac{T_L+36}{33}}, \tag{2.23}$$

$$M = \frac{1}{\cos\theta}, \tag{2.24}$$

$$K = I_0 \exp\left(\frac{-MT_L}{0.9M + 9.4}\right), \tag{2.25}$$

$$D = G - K\cos\theta, \tag{2.26}$$

where I_0, T_L, and M are the solar constant (1367 W m^{-2}), Linke's turbidity factor (=4.5), and air

mass, respectively. The incident shortwave radiation to each surface, i.e., K_1, K_2, $\cdots$, K_k, K_g, K_r, is calculated using the solar zenith angle θ and the direct solar radiation K.

2.1.6 Prediction of Surface Temperature

As the aim of this study is to determine the response of the surface temperature to radiative distribution changes, forecasting the temperature of surface elements is important. The surface temperature and inner temperature of each element can be calculated from the basic heat conduction equations

$$c_i \frac{\partial T_i(t,z)}{\partial t} = -\frac{\partial G_i(t,z)}{\partial z}, \tag{2.27}$$

$$G_i(t,z) = -\lambda_i(z) \frac{\partial T_i(t,z)}{\partial z}, \tag{2.28}$$

where T and G represent the temperature and energy fluxes, respectively. The volumetric heat capacity and the thermal conductivity are denoted by c and λ. The subscript i indicates each surface element. The depth from each surface is described by z. To resolve these equations, two boundary conditions must be given. One is the energy flux into the surfaces, $G_i(t,0)$. As we neglect any turbulent heat fluxes, the energy flux into the i-th element can be simply estimated as the sum of the i-th components of the net shortwave radiation vector $\vec{\Phi}_S$ and net longwave radiation vector $\vec{\Phi}_L$,

$$G_i(z=0) = \Phi_{S,i} + \Phi_{L,i}. \tag{2.29}$$

The second boundary condition is the setting of the inner boundaries. We assume complete insulation at the innermost boundaries of every surface element so that the inner boundaries would not be energy sinks; otherwise, the surface elements would have some biased temperature other than the equilibrium state established only by downward radiative energies.

2.1.7 Effective Albedo and Effective Emissivity

Estimation of the effective albedo and emissivity induced by the 3-d morphology is needed in order to validate this model with previous observational studies, for example, of Aida (1982) and Kanda et al. (2005b), on the radiative effects on urban morphologies. The effective albedo of a unit grid of urban blocks can be defined as the ratio of the outgoing shortwave energy to the incoming shortwave energy in the unit area. Using the description of the albedo matrix, the effective albedo of the unit grid α_{eff} can be described as

$$\alpha_{\text{eff}} = \frac{\left[\mathbf{F}(\mathbf{I} - \mathbf{AF})^{-1}\vec{\Omega}_{\text{S1}}\right]_{\text{sky}}}{K\cos\theta + D}, \tag{2.30}$$

where K, D, and θ are direct solar radiation, diffuse solar radiation, and zenith angle, respectively. The matrices **F**, **I**, and **A** are the configuration factor matrix, unit matrix, and albedo matrix. The vector $\vec{\Omega}_{\text{S1}}$ is the shortwave irradiation vector after first reflections. The subscript 'sky' indicates the element for the sky.

We define a vector $\vec{\Omega}'_{\text{L}}$, which represents the situation in which each surface element emits longwave energy depending on its temperature and there is no downward longwave radiation from the sky, such that $\vec{\Omega}'_{\text{L}} \equiv \left(\sigma T_{\text{l}}^4 \quad \cdots \quad \sigma T_{\text{k}}^4 \quad \sigma T_{\text{g}}^4 \quad \sigma T_{\text{r}}^4 \quad 0\right)^{\text{T}}$. Emissivity is an index of how much longwave radiation a surface emits compared to the amount of longwave radiation emitted if the surface is assumed to be a black body. Using the vector $\vec{\Omega}'_{\text{L}}$, we can describe the total amount of longwave radiation emitted to the sky (assuming a black body surface) by

$$\Lambda_{\text{black}} = \left[\mathbf{F}\vec{\Omega}'_{\text{L}}\right]_{\text{sky}}. \tag{2.31}$$

Conversely, when we use the emissivity matrix, the outgoing longwave radiation from a grey surface can be described by

$$\Lambda_{\text{grey}} = \left[\mathbf{F}(\mathbf{I} - (\mathbf{I} - \mathbf{E})\mathbf{F})^{-1}\mathbf{E}\vec{\Omega}'_{\text{L}}\right]_{\text{sky}}. \tag{2.32}$$

The effective emissivity ϵ_{eff} can then be estimated by the following equation:

$$\epsilon_{\mathrm{eff}} = \frac{\Lambda_{\mathrm{grey}}}{\Lambda_{\mathrm{black}}} = \frac{\left[\mathbf{F}(\mathbf{I} - (\mathbf{I} - \mathbf{E})\mathbf{F})^{-1}\mathbf{E}\vec{\Omega}'_{\mathrm{L}}\right]_{\mathrm{sky}}}{\left[\mathbf{F}\vec{\Omega}'_{\mathrm{L}}\right]_{\mathrm{sky}}}. \tag{2.33}$$

2.2 Comparison with field data

The model developed in this study is composed of a multilayer urban radiation scheme, a group of equations to determine variables of the solar radiation, and a conventional heat conduction equation. Of these components, understanding the applicability of the radiation scheme is particularly important. For evaluation of the radiation scheme, the experimental results of Aida (1982) and Kanda et al. (2005b), which report on albedo changes induced by the distribution of cubed concrete blocks, are very useful. To evaluate the total performance of this model, the surface temperature observations reported by Kanda et al. (2005a), Kawai et al. (2007), and Kawai and Kanda (2010) can be used as a reference. In this section, a comparative evaluation between these experiments and the simulation results of our model are described.

2.2.1 Reproduction of Effective Albedo

The parameters needed to calculate the effective albedo are solar zenith angles and the direct and diffused solar radiation at each time step. These parameters can be estimated from the latitude, longitude, and the day of year where and when the observations were made (Table 2.1). In addition, some incident angle dependencies of the albedo of a flat plane surface are needed for a comparison with the observational results (Kanda et al. 2005b; Oliveira Panão et al. 2007; Fortuniak 2008), and we use the angle dependencies that the previous studies proposed. The dependencies, however, are only applied to the horizontal surfaces (the ground and the roof). The averaged value of the angle dependent albedo over the zenith angles is used for the vertical walls.

Figure 2.5 shows the effective albedo reproduced with the settings for Aida's experiment arranged by zenith angle of the incident solar radiation. The filled circles are the observational

results, which were digitized from Aida (1982). From the albedo values of 0.25-0.3 for June, it can be seen that the simulated effective albedo decreases as the zenith angle decreases, in good agreement with the observations for zenith angles less than 60°. The simulated effective albedo, however, shows a counter-trend with the observations in the range of over 60°. The parameterization of the albedo dependency on the zenith angle, which is proportional to θ^8 in this range, seems to show a strong effect. A different parameterization for the June case could be selected for better reproduction. As for the January case, the reproduction of the albedo is in good qualitative agreement with the observations of having a minimal albedo value at around $\theta = 65°$ in both the morning and evening. The absolute values, however, are not reproduced well. The daily range of albedo change in the simulation seems to be smaller than for the observed values. The albedo change is brought about mainly by the reflection and scattering of the direct component of the solar radiation. The assumption of typical solar radiation as estimated from Eqs. (2.23) - (2.26) is one of the causes of these errors. The observational data show large differences between the morning and evening in spite of the fixed block configuration throughout the day. The larger albedo change in the relatively clear morning, in which the direct component should be larger, implies the influence of the direct-diffuse ratio of the incident solar radiation.

A comparison of the simulation to the observations of Kanda et al.(2005b) is shown in Fig.2.6. Reproduction of the time variation is good in cases with flat albedo change (summer $\lambda_P = 0.25$ and 0.44, where λ_P is the plane area index), with double minima in the morning and evening (autumn $\lambda_P = 0.25$; winter $\lambda_P = 0.25$), and with one minimum around noon ($\lambda_P = 0.69$ in all seasons). The absolute values of the reproduced albedo are in good agreement with the experimental data except in the two cases of summer $\lambda_P = 0.69$ and winter $\lambda_P = 0.44$. This disagreement can be attributed to cloudy weather conditions, as a nearby meteorological observatory recorded no period of sunshine on either day and even detected weak rainfall for the winter case. A better performance can be obtained if the actual radiation, distinguishing the direct and diffuse components, will be given. With the exception of cases with unknown radiation, these comparative evaluations demonstrate the applicability of our radiation scheme to radiation balance studies of

urban morphologies.

2.2.2 Reproduction of the Surface Temperature

Table 2.2 lists the settings for the simulations of the field experiments reported by Kanda et al. (2005a) , Kawai et al. (2007), and Kawai and Kanda (2010). Their field data were obtained by the 1/50 and 1/5 scale models of the Comprehensive Outdoor Scale Model Experiment (COSMO), respectively. These same settings were used for the thermal properties in our simulations. The treatment of the innermost boundary of the facets was set to one of two situations: fixed to the daily averaged radiative temperature of the field data for all facets, or fully insulated boundary conditions. The former setting, i.e., fixed boundary conditions, represents un-insulated concrete buildings or smaller structures whose facet temperatures influence each other in the form of heat conduction. The latter setting, i.e., fully insulated boundary conditions, represents larger structures whose facets are thermally independent of each other. The downward longwave radiation was set to 290 W m^{-2} for the smaller scale model of Kanda et al. and 300 W m^{-2} for the larger scale model case of Kawai et al.

Figure 2.7a shows the reproduced radiative temperature of the urban structure as a whole. The open circles and black and grey lines are the field data and the model results with the fixed innermost temperature setting and with the fully insulated setting, respectively. The reproduction of the daily average and daily variation of the temperature is fairly good by the fixed temperature setting although there are slight differences with the observed data that are caused by the neglect of sensible heat fluxes in our model. On the other hand, there are cases of considerable under and over estimation in the reproduction of each surface temperature by the insulated setting. The differences can be attributed to the absence of energy sink and source that pull surface temperatures to the innermost temperature. The influence of the boundary treatment clearly appears as differences in the nighttime cooling tendencies. The pulling force by the energy source keeps the radiative temperature of the urban canopy constant while the radiative cooling effect seems to be

stronger in the simulation with the insulated setting. However in Fig.2.7b, the simulation with the insulated setting seems to fit the observational results better. The resemblance between them is clear during the nighttime. These simulations imply that the insulated setting in our model is more applicable to bigger objects that are hollow, like the big 1/5 scale model of COSMO, than to smaller objects that are solid, like the small 1/50 scale model of COSMO.

2.3 Urban Surface Warming Potential (USWP)

By how much will the surface temperature rise or fall on average over the long term induced by the radiative distribution changes caused by numerous concrete buildings being built on flat concrete ground with the same material properties? There are presently many urban energy balance models that consider radiation distribution, turbulent fluxes of momentum and heat, water balances, and so on. The models are mainly used as helpful tools to investigate heat island phenomena, and they have achieved success toward understanding them. However, the research that uses these models seems to be focused on the time evolution differences between the temperatures of vegetated rural and artificial urban land surfaces and on the climatic changes of a single city, and not much attention has been paid to the question above.

We believe that we can image idealized radiation equilibrium without any consideration of turbulent heat fluxes in a potentially warmer or cooler state when we assess climatic long-term changes such as urban warming or cooling. Then the turbulent fluxes only have a role in releasing the charged state by transferring heat between the surfaces and the atmosphere. Based on this approach, in this section we calculate the surface temperature of the radiative equilibrium corresponding to the radiation distribution changes induced by the morphological changes of Manhattanized urban buildings, using the radiation scheme developed in this study.

2.3.1 Definition of the USWP

We wish to determine how the spatially and temporally averaged temperature would change when the morphological configuration of urban blocks changes and whether the average temperature would be higher or lower. First we introduce the effective temperature T_{eff} as the spatially averaged temperature of regular urban block arrays as

$$\sigma T_{\mathrm{eff}}^4 \equiv \sum_i^{\mathrm{k,g,r}} f_{si} \sigma T_i^4 . \tag{2.34}$$

where f_{si} denotes the configuration factor from the sky to the i-th element. The subscript i represents the surface elements of the walls, ground, and roof, which are denoted by k, g, and r, respectively. T_{eff} is the same as the radiative temperature, which can be observed from the sky, if all surface elements are assumed to be black bodies with temperature T_i.

We solve the time evolution of the surface elements by using the foregoing model assuming a typical daily time variation of the incident solar radiation described in subsection 2.1.5 to estimate the temporal average of the surface temperature. The daily variation of the surface temperature will converge to a balanced state (i.e., a radiation equilibrium state) although the temperature has a time evolution as the incident radiation changes. After integrating over sufficient time steps for convergence, we average the temperature values over 24 hours. The temporally averaged value is referred to as the 'equilibrium temperature' and is represented as $\overline{T}$ in this study.

$\overline{T}_{\mathrm{eff}}$ represents the spatially- and temporally-averaged temperature of urban block surfaces. On the other hand, we obtain the equilibrium temperature of the roof $\overline{T}_{\mathrm{r}}$ by performing the same temporal average on the roof temperature. The roof is completely isolated from other facets of the ground and wall elements in sight of the radiation. Therefore, the variation with time of the roof temperature represents that of a flat surface with the same material properties. With this analogy, we define the urban surface warming potential by the difference between $\overline{T}_{\mathrm{eff}}$ and $\overline{T}_{\mathrm{r}}$,

$$\mathrm{USWP} = \overline{T}_{\mathrm{eff}} - \overline{T}_{\mathrm{r}}. \tag{2.35}$$

The surface heat island intensity (SHII), a traditional index of urban heating defined as the temperature difference between urban and rural surfaces, varies in time on the order of days on a periodic basis. Moreover, the amplitude of the SHII can vary over a wide range depending on the thermal inertia of the surfaces, as seen in the simulation results of Oke et al. (1991) and Montávez et al.(2008) . The USWP, however, is theoretically independent of the thermal settings because the temporally averaged temperature is determined only by radiative balance when we omit the heat fluxes. Therefore, this index is very useful for extracting the warming effect of the radiative change caused by urban morphological change. Furthermore, as the USWP is estimated by averaging temporally, it is well suited for the estimation of long-term urban warming, which is usually estimated from the annual mean surface air temperature.

2.3.2 Parameter Settings

First, note that this experiment is sort of a thought experiment that does not reproduce the situations of real cities. With these hypotheses, we set simpler material properties, although they are realistic to some extent. The urban block configuration is considered to be square prisms as described in Fig.2.2a, and the urban surfaces are assumed to be made of concrete.

The albedo of concrete material is set to be 0.4 following Aida (1982) and Kanda et al. (2005b), although dependence on the solar zenith angle is neglected. For longwave radiation, we use an emissivity of 0.9 for each surface element. In previous studies, the typical emissivity of urban materials has been set from 0.8 to 1. Numerical sensitivity studies on longwave radiation inside urban geometries (e.g., Sakakibara 1996; Kobayashi and Takamura 1994; Oliveira Panão et al. 2007; Montávez et al. 2008) used emissivity values in the range 0.8-0.9. Comparative studies of simulation and observations of radiation and heat budgets (e.g., Johnson et al. 1991; Sugawara and Takamura 2006; Hamdi and Schayes 2008) used emissivity in the 0.85-0.98 range. Our emissivity setting of 0.9 is at about the midpoint of these ranges.

For the incident solar radiation settings, the latitude and longitude are set to $\phi = 36°$ and $\eta =$

135°, respectively. The solar declination is set to zero by assuming it is on the day of the equinox. The equation of time is also set to zero for a simple analysis. The downward longwave radiation is set to 250 W m^{-2}, which is a typical average value at the latitude around the day of the spring equinox. The thermal parameters used for forecasting the surfaces and their interior temperatures, i.e., the thickness of the concrete, the volumetric heat capacities, and the thermal conductivities inside every element, are set to values similar to those of Kawai and Kanda (2010) , but are simplified as described in Table 2.3. All of the facet elements are assumed to have the same material properties. This assumption is helpful for understanding the pure effects of radiation changes on the thermal environment of urban blocks. The division of wall layers in the vertical direction is set to 5. Some comparative simulations with single-layer settings, emulating an existing single-layer urban energy balance model (e.g., Kanda et al. 2005a), are also performed.

2.3.3 Results

Figure 2.8a presents a 5-day time series of simulated temperatures made with the urban block configurations of $H = B = W = 10$ m. The data are not shown here, but we noted that the daily range and the daily average of the roof temperature were in good agreement with those observed at the building of the Japan Meteorological Agency under a typical clear sky day of March, although there were some slight differences because of the simplistic parameters and the unconsidered fluxes. From the 24-h running average temperatures (the figure shows 6-h increments with points), it seems a time integration of 5 days is sufficient for the temperatures to reach a radiative equilibrium state in this configuration. In the equilibrium state, the 24-h averaged roof temperatures (described with grey triangles) are the coolest of all the surface elements, and the 24-h averaged temperatures at the bottom wall surface (black dots) are the hottest. The upper wall element has lower temperatures than any other lower element, both in average value and in time-by-time values. These features match the observational fact that the deep street canyons of downtown Phoenix, Arizona, have a warmer layer near the ground, as

reported by Fernando et al. (2010). Shortwave radiation can reach the lower sections of the wall in the daytime in this rather sparse configuration. The emission of longwave radiation, however, is larger from the upper wall layers than from lower ones because the configuration factor to the sky is larger from the upper elements. Thus the lower layers can hold more radiative energy than the upper layers.

In the case of a deeper canyon (H = 50 m, B = 10 m, W = 10 m), the temperature of the lowest wall element does not achieve equilibrium even after 5 days (Fig.2.8b). Because shortwave radiation, which is the largest source of energy, cannot reach the lowest level in a canyon of this depth, the wall surface element at the lowest level should achieve equilibrium only by the residual radiative energy of multiple scattering of shortwave radiation and longwave radiation exchanges among wall surface elements and the ground surface. As a result, the order of the facets from the highest to the lowest surface temperatures is the middle wall, bottom wall, top wall, ground, and roof. Figure 2.9 shows the equilibrium temperatures versus several H/W values representing the deepness of the canyon (B = 10 m, W = 10 m). The bottom wall element (i = 1) has the warmest temperature among all elements with $H/W \leq 3$ and the middle wall element (i = 3) is the warmest as H/W increases higher than 3. The top layer element (i = k = 5) also becomes warmer as H/W increases, and it seems to become warmer than the middle layer if the H/W value becomes large enough. As H/W increases (i.e., the urban blocks get higher and the canyons get deeper), the shortwave radiation of the main energy input does not reach the bottom wall elements. The main part of the shortwave radiation, therefore, can only contribute to raising the temperature of the middle and upper wall elements. Not surprisingly, the equilibrium temperature of the roof surface is completely independent of the H/W configuration because the roof is exposed to the sky in all configurations.

Because many previous studies used the sky-view factor as an index of urbanization, Fig.2.10 summarizes the dependency of the USWP on the sky-view factor. The USWP increases as the sky-view factor decreases for each B/W condition (B/W represents the narrowness of the urban canyon). Furthermore, each B/W line approaches its respective USWP intercept as the limit of

the sky-view factor approaches zero. Another interpretation of this figure is that an urban surface can be warmer by about 3 °C in a climatic sense when the urban city grows vertically with the same width ratio of the buildings to the road, $B/W = 1$ for example, from the point U_0 to U_1 (from 0.8 to 0.5 in terms of the sky-view factor) in the figure. If turbulent fluxes work efficiently to transfer heat between the urban surfaces and the atmosphere above, the air temperature will warm by 3 °C.

In addition, the simulation results with single-layer settings are superimposed on the USWP data. The USWP values with single-layer settings increase linearly as the sky-view factor decreases throughout all ranges of the sky-view factor. The overestimation of the USWP is apparent if the sky-view factor is less than about 0.5. This result is consistent with the results of Ikeda and Kusaka (2010) , who concluded that the errors in the calculation of surface air temperature at a height of 1.0 m could be larger in a single-layer urban canopy scheme as compared with a multilayer one. The overestimation occurs because shortwave radiation can reach lower levels even with a low sky-view factor if we consider walls to be single layered and average the shortwave radiation over the entire wall area. In the multilayer scheme, however, the effective temperature can be estimated more precisely with the individual walls separated vertically.

2.4 Summary

By applying the radiosity method, which considers full multiple scattering in an enclosure composed of diffusive surfaces, an urban multilayer radiation scheme applicable to urban canopy surfaces with a three-dimensional morphology of regularly arranged square prism blocks was developed. The radiation scheme was evaluated by comparison with practical observations of albedo changes induced by arrangement changes of concrete cubes as employed by Aida (1982) and Kanda et al. (2005b) . The evaluations showed the radiation scheme to be in fairly good agreement with these observational results.

Combining this precise radiation scheme with equations specifying the amounts of solar ra-

diation and the conventional heat conduction equation, a simulation model that forecasts the time evolution of each surface element according to variations of the incident solar radiation was assembled. Executing this model, we estimated the effect of changes in radiation distributions on the effective surface temperature of homogeneous concrete surfaces of regular block arrays. The 24-h averaged effective surface temperature in the equilibrium state of the block arrays was estimated to be higher than that of the flat surfaces. From a number of sensitivity simulations of the USWP with various levels of canyon deepness, we determined that the USWP becomes larger as the sky-view factor decreases. That is, urban surfaces can potentially become warmer as urban buildings grow higher even without any change to their material properties. The simulations were conducted with ideal 3-d structures and with very simple surface physical properties as a first step toward understanding the contribution of structural changes to the radiative equilibrium temperature. Our simulations have some limitations in terms of real-world interpretation because we did not consider any turbulent heat fluxes to the atmosphere nor heat conduction between elements. The fluxes tend to facilitate heat exchange between the surfaces and the atmosphere and to decrease the surface temperatures. Heat conduction between elements tends to decrease the temperature differences of the surfaces and can act like the single-layer simulations. Even with these limitations, we hope that these results can contribute to a greater understanding of the effects of structural changes on surface temperature.

Additional simulations with a single-layer wall showed some overestimations in the USWP in the sky-view factor range less than about 0.5. This result suggests the applicability of the urban multilayer radiation scheme to reproduction of precise radiation distributions for highly developed urban canopies.

Table 2.1: Parameters for the comparative simulations with Aida (1982) and Kanda et al. (2005b).

	Aida (1982)	Kanda et al. (2005b)
Latitude, longitude	35.5°, 139.5°	36.0°, 139.7°
Experiment date (day of year)	19 Jan 1979 (19) 22 Jun 1979 (173)	Summer experiment λ_p = 0.25, 10 Jul 2002 (191) λ_p = 0.44, 7 Jul 2002 (188) λ_p = 0.69, 17 Jul 2002 (198) Autumn experiment λ_p = 0.25, 26 Sep 2002 (269) λ_p = 0.44, 24 Sep 2002 (267) λ_p = 0.69, 6 Sep 2002 (279) Winter experiment λ_p = 0.25, 10 Dec 2002 (344) λ_p = 0.44, 9 Dec 2002 (343) λ_p = 0.69, 20 Dec 2002 (354)
Albedo dependencies	$\alpha(\theta) = 0.36 + 0.06\,\theta^2 \quad \theta \leq \frac{\pi}{3}$ $\alpha(\theta) = 0.41 + 0.01\,\theta^8 \quad \frac{\pi}{3} < \theta$	$\alpha(\theta) = 0.519282 - 0.329635\cos\theta$ $+0.309507\cos^2\theta - 0.122024\cos^3\theta$
Averaged albedo	0.43	0.41

Table 2.2: Parameters for the simulations of surface temperature comparing with the experiments reported by Kanda et al. (2005a), Kawai et al. (2007), and Kawai and Kanda (2010).

	Kanda et al. (2005a)	Kawai et al. (2007) and Kawai and Kanda (2010)
Latitude, longitude	34.6°, 136.5°	36.0°, 139.7°
Experiment date (day of year)	30 Oct 2003 (303)	Autumn 9 days of 2006 (303) is used for simulations
Albedo dependencies	$\alpha(\theta) = 0.519282 - 0.329635\cos\theta + 0.309507\cos^2\theta - 0.122024\cos^3\theta$	$\alpha(\theta) = 0.097 + 0.194\,\theta - 1.627\,\theta^2 + 5.127\,\theta^3 - 7.225\,\theta^4 + 4.683\,\theta^5 - 1.113\,\theta^6$
Averaged albedo	0.41	0.16
Emissivity	0.98	0.89
Thickness	0.075 m	0.1 m
Volumetric heat capacity	2.48 MJ m^{-3} K^{-1}	2.34 MJ m^{-3} K^{-1}
Thermal conductivity	0.5 W m^{-1} K^{-1}	1.06 W m^{-1} K^{-1}
Treatment of boundary condition	16°C/insulated	24°C/insulated
Downward longwave radiation	290 W m^{-2}	300 W m^{-2}

Table 2.3: Parameters of the walls, ground, and roof on the simulation of USWP.

Albedo	0.4
Emissivity	0.9
Thickness	0.2 m
Volumetric heat capacity	2.0 MJ m^{-3} K^{-1}
Thermal conductivity	1.0 W m^{-1} K^{-1}
Downward longwave radiation	250 W m^{-2}

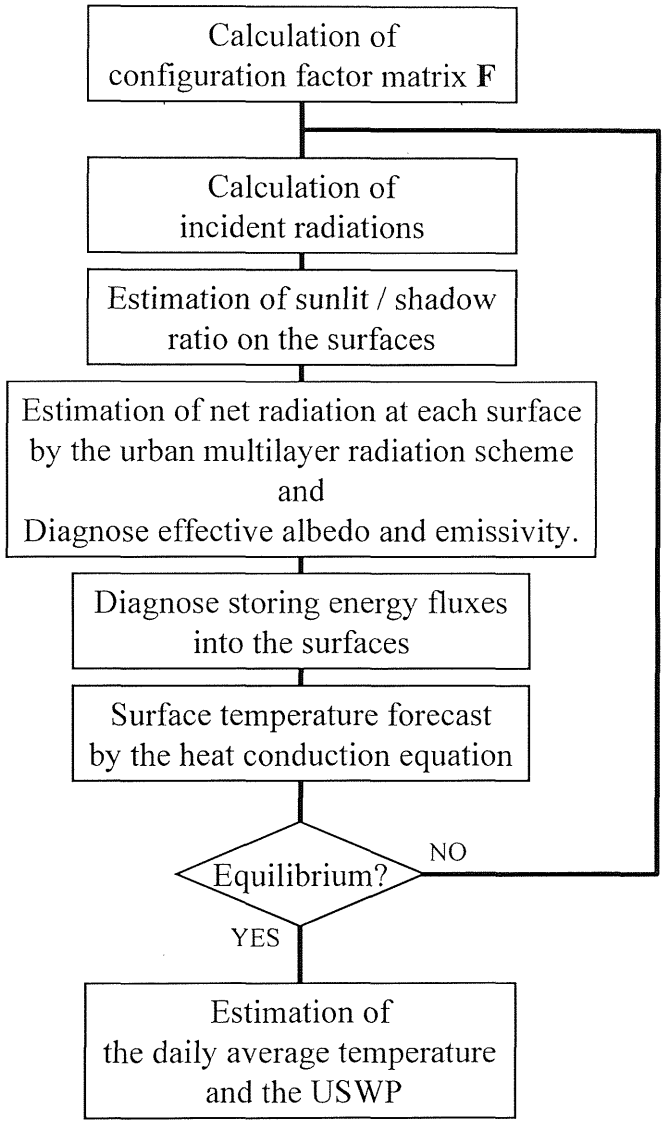

Figure 2.1: Schematic flow chart of the simulation model introduced in this study.

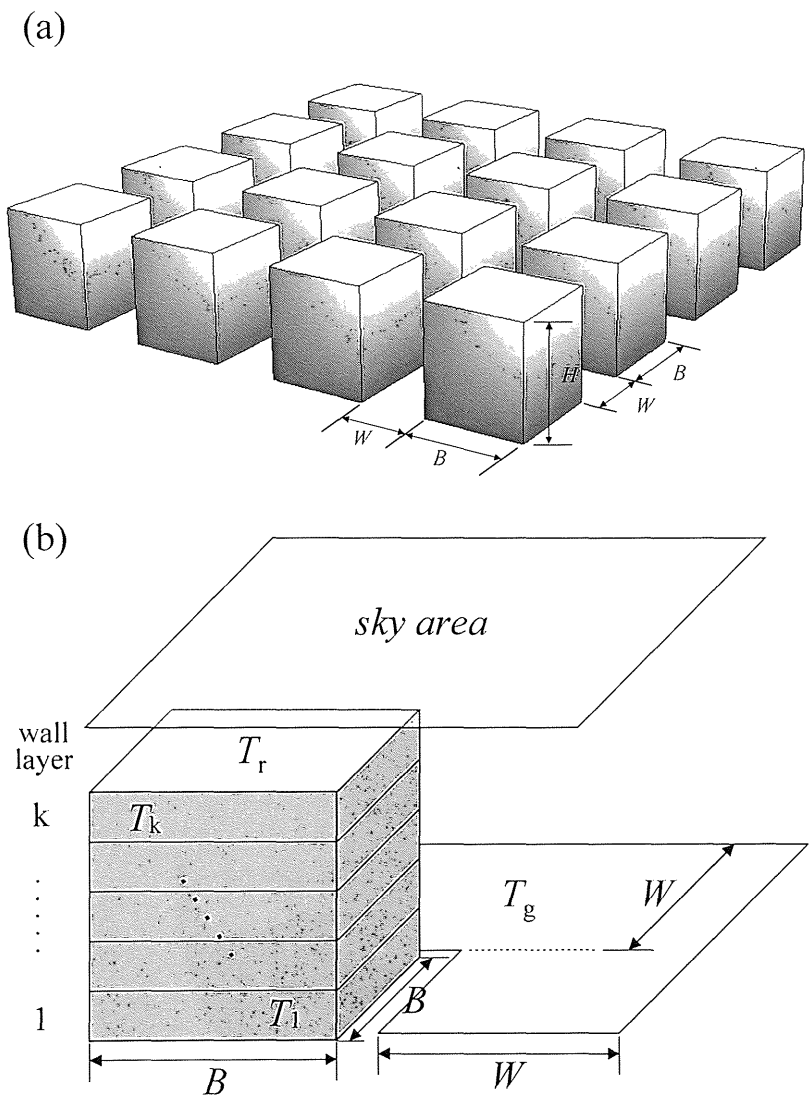

Figure 2.2: Schematic layout of (a) regular block arrays and (b) elements in a unit grid. H and B represent the height and width of the blocks, and W is the ground (street) width. T denotes the surface temperature of each element. Subscripts $1, \cdots,$ k denote the wall elements (layeres), and r and g denote roof and ground elements, respectively.

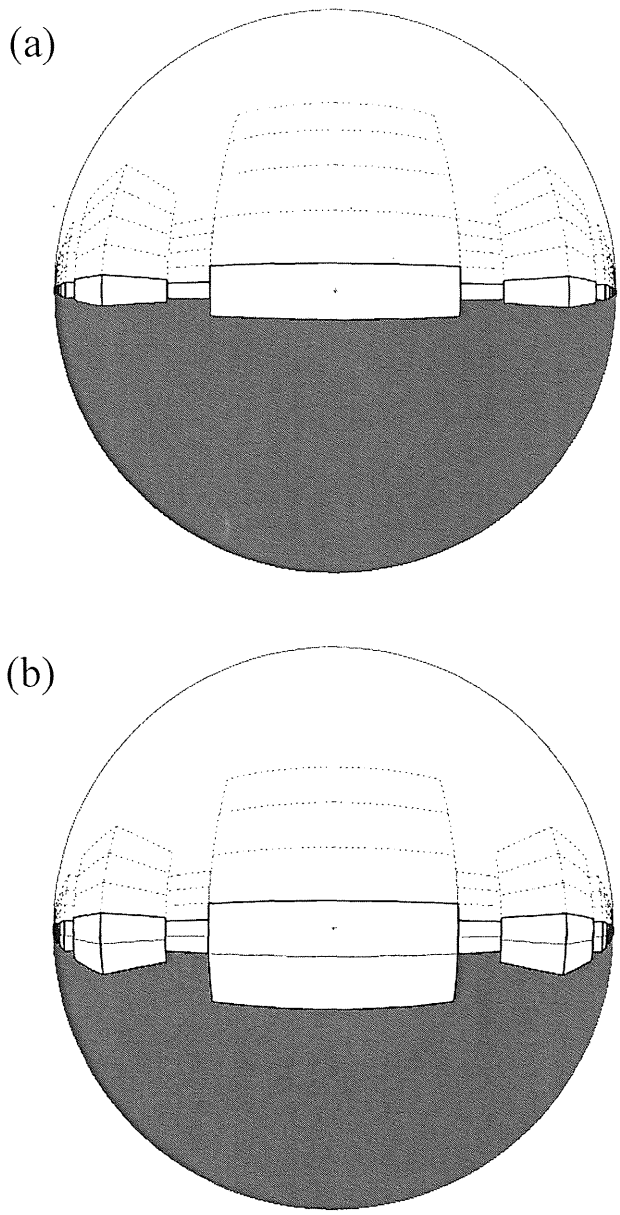

Figure 2.3: A fisheye viewing image horizontally from the centre of (a) the lowest wall layer and (b) a second wall layer. *Dotted lines* show wall layer envelopes of 5-layer block model. *Thick lines* describe (a) one layer height model and (b) two layers height model. *Light and dark grey areas* represent the sky and the ground, respectively

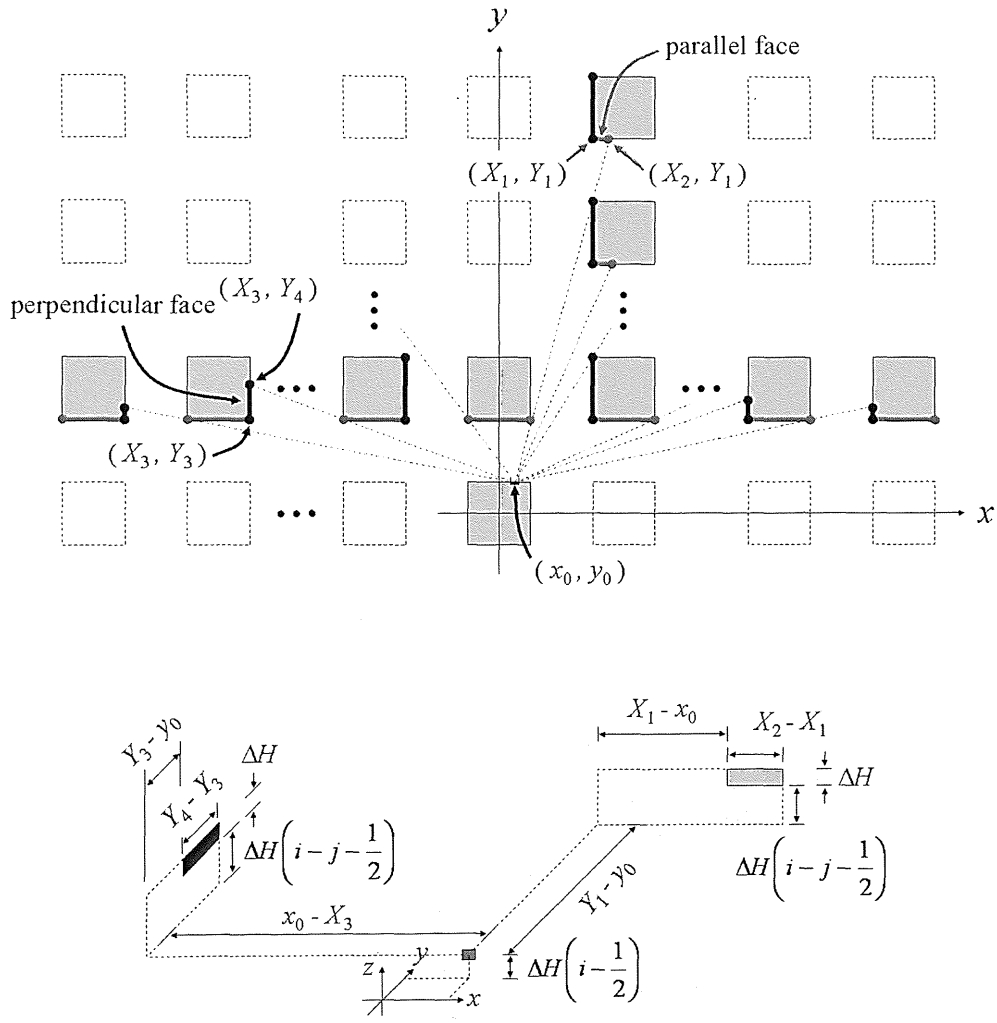

Figure 2.4: The coordinate system and images used for configuration factor calculations. The *black* and *grey* line segments represent perpendicular and parallel block faces that can be seen from (x_0, y_0)

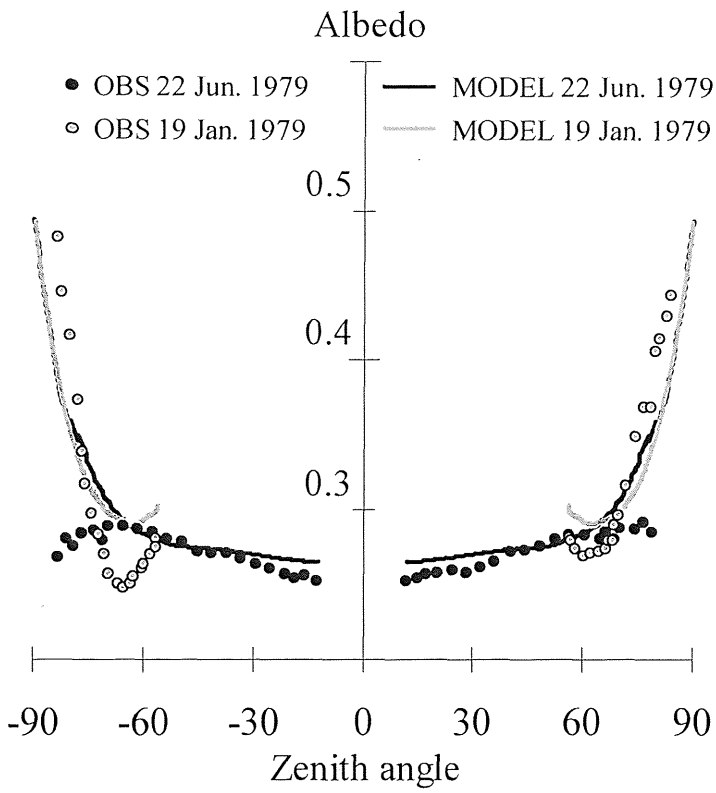

Figure 2.5: The albedo changes of urban blocks simulated for the observational results of Aida (1982). Dots are digitized values from Aida (1982). The solid lines represent the simulated data of the present radiation scheme. The negative values in zenith angles represent the morning data.

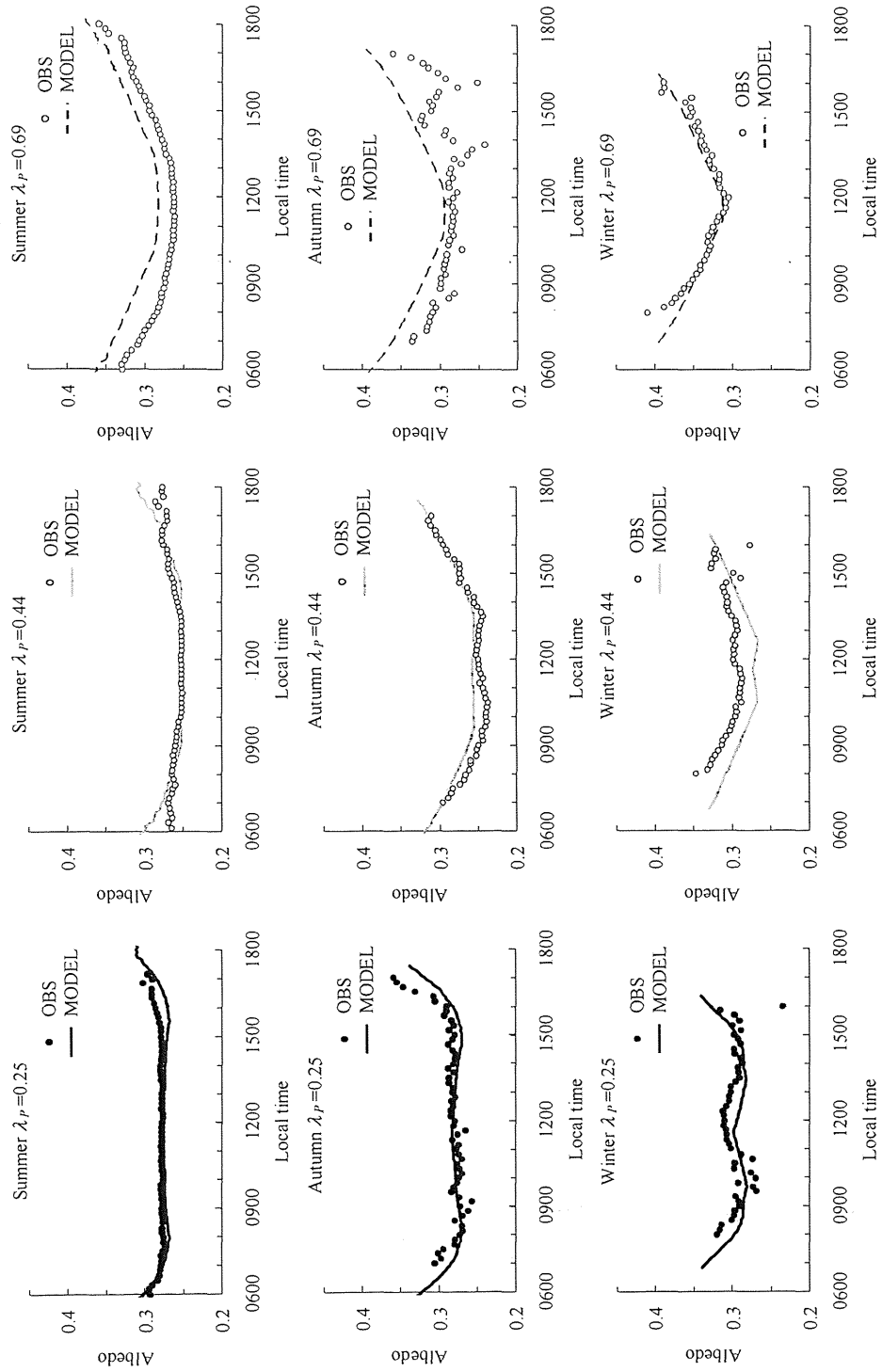

Figure 2.6: The albedo changes of urban blocks simulated for the observational results of Kanda et al. (2005b). Dots are digitized values from Kanda et al. (2005b). The solid lines represent the simulated data of the present radiation scheme.

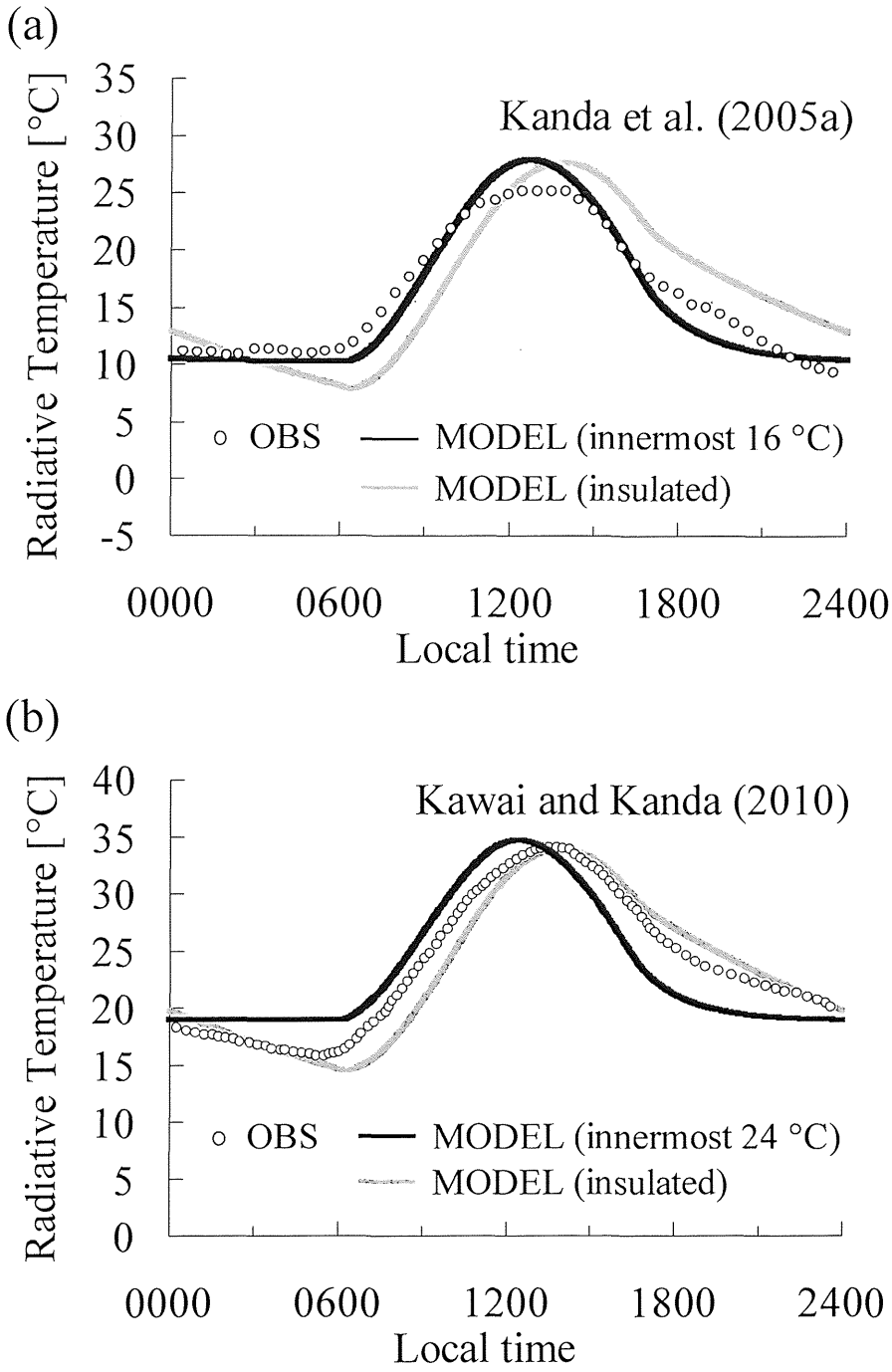

Figure 2.7: The reproduction of radiative temperature simulated for the observational results of Kanda et al. (2005a), Kawai and Kanda (2010). *Open circles* represents the observed values digitized from Kanda et al. (2005a) and Kawai and Kanda (2010). The *solid lines* represent the simulated data of the present model.

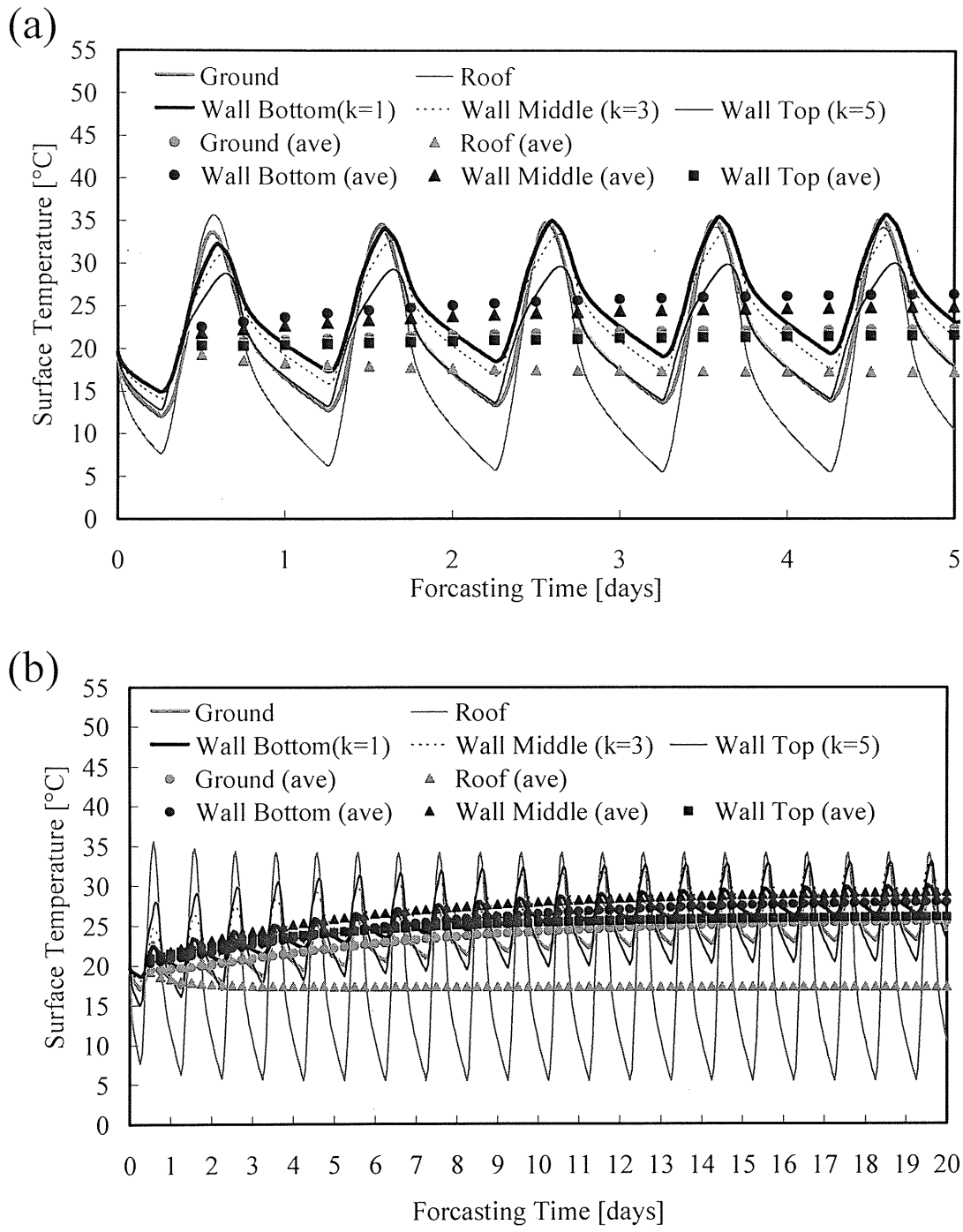

Figure 2.8: Time series of simulated temperatures of the lowest (i = 1), middle (i = 3), and top wall elements (i = 5) and the ground and roof elements: (a) H = 10 m, B = 10 m, W = 10 m, (b) H = 50 m, B = 10 m, W = 10 m. *Each mark* indicates running 24-h average temperatures at an interval of 6 h.

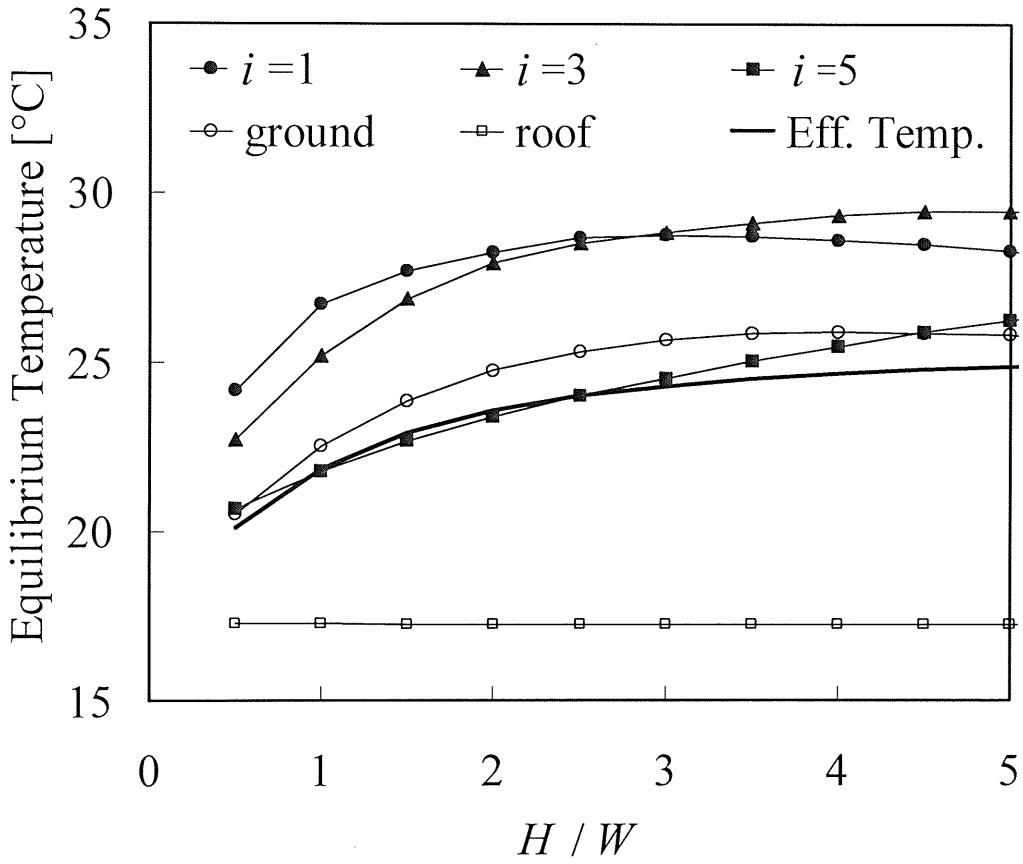

Figure 2.9: Running 24-h average equilibrium surface temperatures as a function of H / W. The temperature of the lowest ($i = 1$), middle ($i = 3$), and top ($i = 5$) wall elements and the ground and roof elements are shown. The effective surface temperature of the block arrays is also shown.

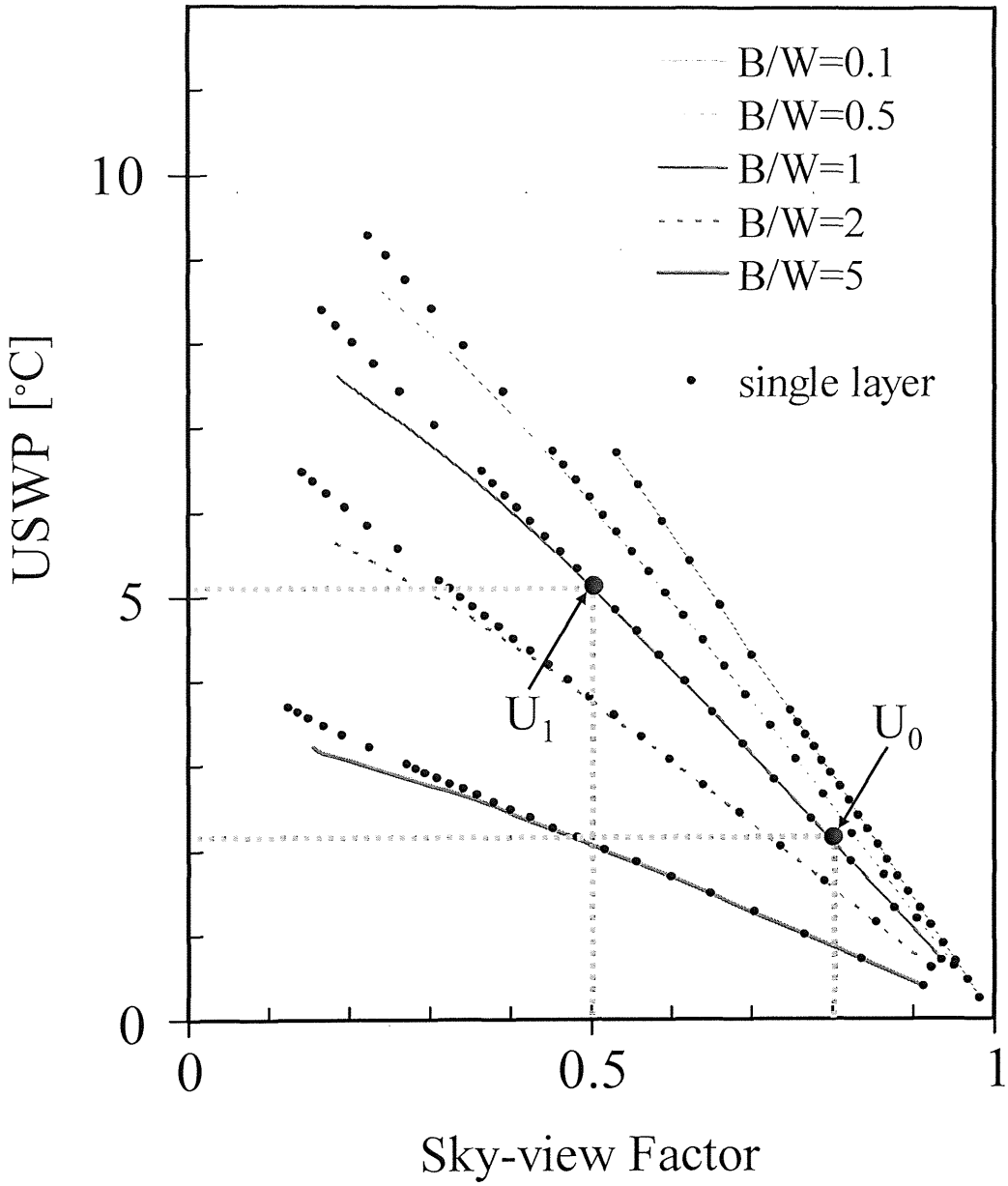

Figure 2.10: The USWP as a function of the sky-view factor with superimposed the results of a single-layer calculation. The points U_0 and U_1 represent two urban states. Moving from U_0 to U_1 means urban growth on verticalization with the same building area.

Chapter 3

Development of A Square Prism Urban Canopy (SPUC) Scheme for Mesoscale Atmospheric Models

3.1 A Square Prism Urban Canopy (SPUC) Scheme

In the previous chapter, we figured out the urban surface warming by radiation budget change only induced by the morphological modification of urban buildings. The derived warming rate, however, is just a warming "potential" under an ideal situation that there is no heat transfer between the urban surfaces and the air above. If we want to estimate the warming effect more realistically, an energy balance scheme which can consider heat transfer effect and exhaust heat effect in addition to the radiation effect is needed. As we reviewed in Chapter 1, many ideas of urban canopy parameterization have been proposed, by which such effects of urban surfaces can be estimated comprehensively. In this chapter, details of newly developed urban canopy scheme for the JMA-NHM will be described and the performances and limitations of the scheme will be checked.

3.1.1 Definition of Urban Building Array

In this study, the SPUC scheme was designed as part of the land surface scheme in the JMA-NHM mesoscale model. The concept of an urban canopy is based on the vegetation canopy scheme of Deardorff (1978) . The urban canopy layer consists of the lowest atmospheric layer and urban canopy elements (typically buildings or houses). Surface exchanges of heat and momentum affected by the canopy elements are described in the urban scheme. The present SPUC scheme assumes a uniform building array with a building area density equivalent to the actual grid average. The modeled buildings in a grid are all square prisms of the same shapes that are distributed regularly, not staggered. The geometrical image is shown in Fig. 3.1. The variables H, B, and W represent building height, building width, and width of the ground between buildings, same as in the chapter 2. The conventional parameters, frontal area index λ_f and plane area index λ_p can be written with these geometric variables as

$$\lambda_f = \frac{BH}{(B+W)^2} \tag{3.1}$$

$$\lambda_p = \frac{B^2}{(B+W)^2} \tag{3.2}$$

The physical properties of buildings are set to uniform values. The momentum fluxes are estimated by a roughness parameter approach, as in ordinary slab schemes, but the radiation processes and heat fluxes are more detailed in the SPUC scheme.

The radiation distributions are calculated assuming that the shapes of buildings are square prisms, as in Kanda et al. (2005b). The sky-view factor is calculated from the settings of height and width of the buildings and width of the road. We define the sunlight factor as the sunlit area fraction at the ground. The sunlight factor also includes a parameter for the solar zenith angle. The SPUC scheme does not distinguish the azimuthal angles of the walls. This means the sunlight factor is calculated by averaging the values of the calculation with 360° rotating azimuthal directions of the regular building arrays. The interception of precipitation by the buildings and

water storage on the surfaces of the buildings are also considered. Therefore, the latent heat fluxes from building surfaces can be calculated.

3.1.2 Circuits of heat fluxes

The present SPUC scheme is similar to existing single-layered canopy schemes in several aspects, although it differs from them in the representation of the circuit configuration of heat fluxes. Figure 3.2 shows the conceptual schematic of the flux circuit. The equations for the sensible heat and the latent heat flux exchange are as follows:

$$\begin{aligned}\rho c_{\mathrm{p}} C_{\mathrm{h\_a}} U_{\mathrm{a}}(T_{\mathrm{af}} - T_{\mathrm{a}}) = {} & \rho c_{\mathrm{p}} S_{\mathrm{f}} C_{\mathrm{h\_r}} U_{\mathrm{af}}(T_{\mathrm{r}} - T_{\mathrm{af}}) \\ & + \rho c_{\mathrm{p}} S_{\mathrm{f}}(WAI - 1) C_{\mathrm{h\_w}} U_{\mathrm{af}}(T_{\mathrm{w}} - T_{\mathrm{af}}) \\ & + \rho c_{\mathrm{p}}(1 - S_{\mathrm{f}}) C_{\mathrm{h\_g}} U_{\mathrm{af}}(T_{\mathrm{g}} - T_{\mathrm{af}}) \\ & + Q_{\mathrm{s}}\end{aligned} \tag{3.3}$$

$$\begin{aligned}\rho L C_{\mathrm{q\_a}} U_{\mathrm{a}}(q_{\mathrm{af}} - q_{\mathrm{a}}) = {} & \rho L \delta_{\mathrm{r}} S_{\mathrm{f}} C_{\mathrm{q\_r}} U_{\mathrm{af}}[q_{\mathrm{s}}(T_{\mathrm{r}}) - q_{\mathrm{af}}] \\ & + \rho L \delta_{\mathrm{w}} S_{\mathrm{f}}(WAI - 1) C_{\mathrm{q\_w}} U_{\mathrm{af}}[q_{\mathrm{s}}(T_{\mathrm{w}}) - q_{\mathrm{af}}] \\ & + \rho L \beta(1 - S_{\mathrm{f}}) C_{\mathrm{q\_g}} U_{\mathrm{af}}[q_{\mathrm{s}}(T_{\mathrm{g}}) - T_{\mathrm{af}}] \\ & + Q_{\mathrm{l}}\end{aligned} \tag{3.4}$$

where S_{f} is the area fraction of the buildings, which is equal to the plane area index, λ_{p}. ρ, c_{p}, and L are the air density, heat capacity of the air, and latent heat of vaporization, respectively. C_{h} and C_{q} represent bulk coefficients of sensible and latent heat. The subscriptions a, r, w, and g here represent the bulk coefficients between the lowest atmospheric layer and the canyon air, between roof surface and the canyon air, between wall surface and the canyon air, and between the ground and the canyon air, respectively. U_{a} and U_{af} are wind velocities at the lowest atmospheric layer and inside the canyon. T represents temperature and its subscriptions a, af, r, w, and g mean the temperatures of the lowest atmospheric layer, the air inside the canyon, roof surface, wall surface,

and of the ground surface, respectively. q represents specific humidity with the same meanings of the subscriptions of T. $q_s(T)$ represents the saturated specific humidity at temperature T. δ and β represent the wet area ratio (explained in the following section) and the evaporation efficiency, respectively. Q_s and Q_l are the anthropogenic sensible heat and the anthropogenic latent heat released to the atmosphere. The area of walls is controlled by the wall area index WAI, defined as the ratio of (roof area + total wall area) to (roof area). It can be linked to the geometric parameters H and B, or λ_f and λ_p as

$$WAI = 1 + 4\frac{H}{B} = 1 + 4\frac{\lambda_f}{\lambda_p} \tag{3.5}$$

If the aspect ratio of height/width of the building is small (i.e., long, square buildings), WAI becomes small, whereas for tall buildings such as skyscrapers, WAI increases.

In the present formulation, the total of heat fluxes exchanged between each facet and the canyon air balances the flux between the canyon air and the overlying atmospheric layer. In this SPUC scheme, a main difference from other urban canopy schemes is the flux path from the roof to the canyon air. Other canopy schemes usually assume a flux line from the roof directly to the lowest level of the atmosphere. This concept basically assumes that constant flux layers are formed between reference level of the atmosphere and roof surface, and between the reference level of the atmosphere and the canyon air, respectively. Those schemes well represent situation of urban canopy with rather uniform building heights. In actual cities such as Tokyo from mesoscale point of view, however, the buildings heights are so dispersed that the mean roof level lies within the canopy layer; therefore, we assume that the routes of heat fluxes from all facets, including the roof, pass through the canyon air. Thus, the flux is exchanged between the canopy surfaces and the atmosphere via the canyon air.

The azimuth direction of walls is not taken into account in this SPUC scheme, because the actual orientations of buildings can be considered random in the model grid. Therefore, this scheme has only one temperature for the walls: the azimuthally averaged value. The displacement height,

which is an effective ground level, is currently set to;

$$z_{af} = S_f H \tag{3.6}$$

3.1.3 Wind velocity inside the canyon

The wind velocity in the canyon, U_{af}, is given by the following equation:

$$U_{af} = \tau S_f u_* + (1 - S_f) U_a \tag{3.7}$$

which is from the vegetation canopy scheme by Deardorff (1978). The variable τ controls the wind velocity in the canopy layer. The constant value of $\tau = 0.83$ based on the observation of forest canopies is used. Although it is noted that there are much room for improvement on description of this term, Eq. (3.7) quantitatively represents wind speed variation in the canopy layer with area fraction of the buildings. That is, the velocity U_{af} approaches the velocity of the lowest atmospheric layer U_a when the building coverage is small. U_{af} approaches roughly the friction velocity, u_*, when the building area fraction becomes large.

3.1.4 Bulk coefficient for heat fluxes

The bulk coefficients C_{h_r} for the roof and C_{h_w} for the walls, which determine the fluxes from roof and walls, are given as:

$$C_{h\_r} = C_{h\_w} = 0.01\left(1 + \frac{0.3}{U_{af}}\right) \tag{3.8}$$

(Deardorff 1978). For consistency with the expression of wind velocity U_{af} from the vegetation canopy scheme, we also use the bulk coefficient of Deardorff (1978) as the default value.

The coefficient between the canyon air and the lowest atmospheric layer, C_{h_a}, is calculated by the conventional surface scheme taking account of the Monin-Obukhov similarity theory (MOST). The scheme of Beljaars and Holtslag (1991) is utilized in the present surface scheme

of the JMA-NHM. The bulk coefficient between the ground and the canyon air, C_{h_g}, is set to the same value as C_{h_a}. Although we can apply the MOST to the layer between the canyon air and the ground, the Obukhov's stability parameter $\zeta(= z/L)$ will be nearly zero ($\zeta \simeq 0$) at any time when we apply it to such a thin layer. Then we set the bulk coefficient between this thin layer equals to the coefficient between the canyon air and the lowest level of the atmosphere in order to get the features 'stable' or 'unstable' atmospheric conditions. In this research, C_{q_a}, C_{q_r}, C_{q_w}, and C_{q_g} which represent the coefficients for moisture are set to be equal with corresponding coefficients for heat, C_{h_a}, C_{h_r}, C_{h_w}, and C_{h_g}, respectively.

3.1.5 Sky-view factor

We define the sky-view factor as the area-averaged ratio of the orthogonally projected area of the sky (residual area of the shaded area by any canopy elements) to that of the celestial sphere from grid cells of the ground. Figure 3.3 is a schematic illustration of the sky-view factor calculation. The area on the celestial sphere shaded by objects such as buildings is projected onto the horizontal plane orthographically. Then the sky-view factor from one grid cell at the ground, s_{vf}, is defined as

$$s_{vf} = \frac{\pi r^2 - S_{\text{object}}}{\pi r^2} = 1 - \frac{S_{\text{object}}}{\pi r^2} \tag{3.9}$$

By using the coordinate system shown at the top of Fig. 3.4, we can obtain the elevation angle, Θ, which represents the envelope curve of a building's roof and walls as the function of the azimuth angle, ϕ. The sky-view factor is calculated by the integration of $\Theta(\phi)$,

$$\begin{aligned} S_{\text{object}} &= \int_0^{2\pi} \int_0^{\Theta(\phi)} r^2 \sin\Theta \cos\Theta d\Theta d\phi \\ &= \frac{r^2}{4} \int_0^{2\pi} [1 - \cos 2\Theta(\phi)] d\phi \end{aligned} \tag{3.10}$$

$$s_{vf} = 1 - \frac{1}{4\pi} \int_0^{2\pi} [1 - \cos 2\Theta(\phi)] d\phi \tag{3.11}$$

The ground area between the buildings and intersection space are divided in 10 × 10 grid boxes, and the area-weighted average of the sky-view factors is calculated from all the small patches (see Fig. 3.4, bottom).

3.1.6 Sunlight factor at the ground

The SPUC scheme calculates the radiation distribution between the roof, walls, and ground, assuming the shape of the buildings to be square prisms. In the calculation of the shortwave radiation, the ratio of sunlight area at the ground (hereafter referred to as sunlight factor of the ground; s_{IG}), which is calculated from the zenith angle of the sun, is the most important parameter. Kanda et al. (2005b) proposed the calculation scheme of sunlit-shadow distribution, which was designed to calculate the distribution of shortwave radiation to six facets: the roof, the road, and the walls at four azimuthal directions. In the present scheme, however, only grid-averaged wall temperature regardless of the facet is considered. Therefore, we consider only how much sunlight reaches the ground. The shape of a building's shadow on the ground depends on the zenith angle and azimuth angle of the sun, as well as the density of the buildings. The calculation of s_{IG} is carried out around 360° with the fine pitch interval (in this study set to 1°) of azimuthal angles. The calculation is performed while taking into account whether the shadow reaches the neighboring building. By calculating s_{IG} at every time step, the SPUC scheme can realistically represent the shortwave radiation entering each of the surface materials. The walls receive a larger amount of shortwave radiation than the ground around dawn and at dusk, whereas at noon more shortwave radiation enters the ground than the walls.

Variables H, B, W, θ, and ϕ represent the height of the building, width of the building, width of the road (see Fig. 3.3), zenith angle of the sun, and the azimuth angle of the sun using due east as the reference direction, respectively. For simplicity, we now consider regular building arrays, in which the building widths are larger than road widths ($B > W$). We also consider only one neighboring building, which the shadow from one building reaches. Consideration of azimuth

angles from 0° to 45° is sufficient because of the grid's symmetrical property. Thus, the shadowing pattern can be separated into four cases, which are described in Fig. 3.5: (i) the shadow does not reach any neighboring buildings; (ii) the shadow reaches the building to the west but does not reach those to the northwest or north; (iii) the shadow reaches two neighboring buildings, those to the west and northwest; and (iv) the shadow reaches three neighboring buildings, those to the west, northwest, and north.

The sunlight factor for each case is calculated as follows:

(i) $H\tan\theta\cos\phi < W$ and $H\tan\theta\sin\phi < W$,

$$s_{IG} = \frac{1}{W^2 + 2BW}\left[W^2 + 2BW - BH\tan\theta(\cos\phi + \sin\phi)\right], \tag{3.12}$$

(ii) $H\tan\theta\cos\phi \geq W$ and $H\tan\theta\sin\phi < W$,

$$s_{IG} = \frac{1}{W^2 + 2BW}\left[W^2 + BW - (B + W)H\tan\theta\sin\phi + W^2\tan\theta\right], \tag{3.13}$$

(iii) $H\tan\theta\cos\phi \geq W$, $H\tan\theta\sin\phi \geq W$, and $W/tan\phi \geq B$,

$$\begin{aligned} s_{IG} = \frac{1}{W^2 + 2BW}\Bigg[&\left(\frac{W}{\tan\phi} - H\tan\theta\cos\phi + W\right)(W\tan\phi - H\tan\theta\sin\phi + W) \\ &+ \left(\frac{W}{\tan\phi} - B\right)(H\tan\theta\sin\phi - W)\Bigg] \end{aligned} \tag{3.14}$$

(iv) $H\tan\theta\cos\phi \geq W$, $H\tan\theta\sin\phi \geq W$, and $W/\tan\phi < B$,

$$s_{IG} = \frac{1}{W^2 + 2BW}\left(\frac{W}{\tan\phi} - H\tan\theta\cos\phi + W\right)(W\tan\phi - H\tan\theta\sin\phi + W) \tag{3.15}$$

In cases (iii) and (iv), we assume s_{IG} equals 0 if the shadow reaches over the neighboring buildings ($H\tan\theta\sin\phi > B + W$ or $H\tan\theta\cos\phi > B + W$).

Equation (3.15) overestimates the sunlight factor when $B < W$ and underestimates it when the shadow reaches farther buildings. The resultant estimation error, however, is so small as to be

negligible. Therefore, Eqs. (3.12) to (3.15) are used to calculate the sunlight factor in the present study. An example of the time series of s_{lG} is shown in Fig. 3.6. As the aspect ratio of the canyon (H/W) increases, s_{lG} values decrease; thus, narrow diurnal variations are obtained.

3.1.7 Distribution of radiation

The scattering process within the canopy layer is considered only once. The shortwave radiation reflected by the walls or the ground is considered to be nearly specular reflection. Once the shortwave radiation reaches the surfaces, part of the received radiation evenly spreads to the surfaces and is reflected as the surface albedo at the same solar zenith angle. The amount of reflected radiation obtained by this process has an intermediate value between complete specular reflection and complete diffused radiation. After the reflection, reflected shortwave radiation is redistributed to each surface according to the sunlight factor, s_{lG}. The reflected shortwave radiation is absorbed completely by the second surfaces regardless of their albedo.

The distribution of longwave radiation is controlled by the averaged sky-view factor at the ground, s_{vG}. The radiations that enter the roof (R_r), walls (R_w), and ground (R_g) are expressed by the following equations:

$$R_r = S^{\downarrow} - \alpha_r S^{\downarrow} + L^{\downarrow} - \sigma T_r^4 \tag{3.16}$$

$$\begin{aligned} R_w = \Big[&(1-S_f)(1-s_{lG})S^{\downarrow} - \alpha_w(1-S_f)(1-s_{lG})S^{\downarrow} + (1-s_{lG})\alpha s_{lG}(1-S_f)S^{\downarrow} \\ &+(1-S_f)(1-s_{vG})L^{\downarrow} - 2(1-S_f)(1-s_{vG})\sigma T_w^4 + (1-S_f)(1-s_{vG})\sigma T_g^4\Big] \\ &/S_f(WAI-1) \end{aligned} \tag{3.17}$$

$$\begin{aligned} R_g = &s_{lG}S^{\downarrow} - \alpha_g s_{lG}S^{\downarrow} + (1-s_{lG})\alpha_w S^{\downarrow} \\ &s_{vG}L^{\downarrow} - \sigma T_g^4 + (1-s_{vG})\sigma T_w^4 \end{aligned} \tag{3.18}$$

R, $S^{\downarrow}$, $L^{\downarrow}$, α, and σ represent net radiation, downward shortwave radiation, downward longwave radiation, albedo, and the Stephen-Boltzmann constant, respectively. The subscriptions of r, w, and g represent the values of roof, walls, and the ground. The emissivity is assumed to be 1 at

this time.

The sunlight caught by walls, the first term in the brackets of right side of the equation (3.17), is simply related to $(1 - S_f)(1 - s_{lG})S^{\downarrow}$ which represents the residual energy flux (in the unit of W) of the sunlight reach the ground surface (Fig. 3.7). The third term in the brackets of right side of the equation (3.17) represents the energy flux to walls after reflection by the ground. These energy fluxes are divided by total area of walls, $S_f(WAI - 1)$, in order to express the energy flux per unit area.

From the reciprocity law, the sky-view factor from the walls can be estimated as $(1 - S_f)(1 - s_{vG})/S_f(WAI - 1)$. Then the longwave flux from the sky to walls shall be the forth term of right side of equation (3.17). The fifth term describes the outgoing longwave flux from the walls to the sky and to the ground. The sixth term is the incoming longwave flux from the ground.

3.1.8 Heat conduction calculation

The temperature inside the roof and walls of the buildings and the temperature of the ground inside the building canyon are calculated by the following heat conduction equations:

$$c(z)\frac{\partial T(t,z)}{\partial t} = -\frac{\partial G(t,z)}{\partial z} \tag{3.19}$$

$$G(t,z) = -\lambda(z)\frac{\partial T(t,z)}{\partial z} \tag{3.20}$$

where T is the temperature at time t and depth z of the building materials or the ground, G represents the heat conduction flux, and c and λ denote the volumetric heat capacity and thermal conductivity, respectively. This equation can be solved numerically with the heat budget at the surface and the temperature at the innermost layer inside the building or the ground as the boundary conditions. The heat budget at the surface is given as the balance of radiation and heat fluxes.

3.1.9 Water storage and precipitation trapping

Because this SPUC scheme is designed to be used with the JMA-NHM for simulation under a wide range of meteorological conditions, we consider the interception of precipitation and water storage on the surfaces of buildings as well. The trapping of precipitation by the wall is controlled by the partition rate, σ_{trap}. The amount of precipitation trapped by each facet is described by following equations:

$$\Delta P_{\mathrm{r}} = \Delta P \tag{3.21}$$

$$\Delta P_{\mathrm{w}} = \frac{1 - S_{\mathrm{f}}}{S_{\mathrm{f}}(WAI - 1)} \sigma_{\mathrm{trap}} \Delta P \tag{3.22}$$

$$\Delta P_{\mathrm{g}} = \left(1 - \sigma_{\mathrm{trap}}\right) \Delta P \tag{3.23}$$

where ΔP represents the precipitation per unit area above the canopy layer. The rain that falls into the canyon spaces is redistributed to walls and the ground by σ_{trap}. Although the σ_{trap} is currently set to a constant value of 0.5, the value is better to be changed according to the wind speed inside the canyon space. The amount of water intercepted by the walls is evenly distributed to all four walls.

The storage of water is controlled separately by the maximum volume of water, W_{max}, at the roof and walls. The overflowing water on the roof is channeled outside the system through a drain, whereas the overflowing water on the walls is assumed to go to the ground, assuming that there are no drains on the walls.

The latent heat flux from the roof and walls are controlled by δ, the wet area ratio. The fractional area of δ on each surface is considered to be coated with water. The wet area ratios of roof and walls are given by the following equations:

$$\delta_{\mathrm{r}} = \min\langle W_{\mathrm{r}} / W_{\mathrm{max,r}}, 1 \rangle \tag{3.24}$$

$$\delta_{\mathrm{w}} = \min\langle W_{\mathrm{w}} / W_{\mathrm{max,w}}, 1 \rangle \tag{3.25}$$

where W represents the volumetric water content per unit area, and W_{max} is the maximum volume of water storage. Using these parameters δ, the latent heat fluxes from the surfaces, E_r and E_w, are described as:

$$E_r = \rho L C_{q\_r} U_{af} \delta_r [q_s(T_r) - q_{af}] \tag{3.26}$$

$$E_w = \rho L C_{q\_w} U_{af} \delta_w [q_s(T_w) - q_{af}] \tag{3.27}$$

The increase of the volumetric water content on the roof and walls is calculated by considering the gain by precipitation and the loss by latent heat flux. The rate of change of the water content on the surfaces is calculated by the following equations:

$$\Delta W_r = \Delta P_r 10^{-3} - (E_r/\rho L)\Delta t \tag{3.28}$$

$$\Delta W_w = \Delta P_w 10^{-3} - (E_w/\rho L)\Delta t \tag{3.29}$$

where Δt is the time interval of the integration. At the ground level, the water content is calculated as in the SLAB scheme (force restore method of Deardorff 1978).

3.2 Evaluations of SPUC on typical weather conditions

To evaluate the performance of the SPUC scheme, a forecasting experiment was executed using a SPUC-coupled JMA-NHM and compared to one performed using a SLAB-coupled JMA-NHM. The settings of SLAB were similar to those of the operational one. The targeted area was the Tokyo Metropolitan area. Figure 3.8 shows a map of the forecasted domain; the distribution of the building area fraction; the location of Kugahara, where the observations of radiation and heat fluxes were conducted; and locations of the four AMeDAS stations discussed later. The horizontal resolution of the two simulations (SPUC run and SLAB run) was 4km x 4km.

For the clear weather condition, the targeted day was 20 August 2005, on which the flux observations were carried out at the Kugahara station (Moriwaki and Kanda 2004) . The initial

time of the simulation was 0900 Japan Standard Time (JST). The forecasting time was 39 h, and the last 24 h were used for analysis. During the earlier forecasting times in the simulations, the temperatures inside the buildings are quite sensitive to the initial conditions. To check the water storage performance, a simulation on 12 and 13 August 2005 was also executed. The forecasting time was expanded to 63 h because a rain event continued over the 2 days. The initial and boundary meteorological data were the operational mesoscale model analysis data set (10-km resolution data). The SPUC scheme was applied only on those grids with more than 50% of the land use designated as urban building area, road area, and bare urban area. (The SPUC-applied grids are those with color shading in Fig. 3.8, right.) For other rural grids, the SLAB scheme was applied. The anthropogenic heat distribution of Senoo et al. (2004) was used in the SPUC run only.

3.2.1 SPUC settings

The heights of buildings were fixed to 10 m, and the building shapes were set as half of a cube (WAI = 3). The area fraction of buildings was evaluated from the Digital National Land Information of the Ministry of Land, Infrastructure, Transport and Tourism of Japan and we assumed that buildings occupied 60% of the area in the " building area " land use category. Based on these parameters, the sky-view factor and the sunlight factor were calculated. Physical properties of the roof and walls of buildings were set to those of wooden residential properties (see Table 3.1). The temperature inside the buildings was assumed to be 25°C.

The parameters of the ground inside the canyon, such as albedo, wetness, heat capacity, and heat conductivity, were calculated by area-averaging of each land use category except the building area. This approach of averaging the parameter settings is the same approach used in the operational SLAB scheme of the JMA-NHM.

3.2.2 Surface air temperature

Figure 3.9 shows the simulation results of daily variation of surface air temperature at the five targeted grid points illustrated in Fig. 3.8. Tokyo is a highly established urban area. Although Nerima has a higher area fraction of buildings than Tokyo, it is actually a residential area. Kugahara is also a dense residential area. Kumagaya was selected as an urban grid with a lower building area fraction than Tokyo. Finally, Hatoyama is a rural site to which we applied the slab scheme in both the SPUC run and SLAB run.

The surface air temperature (i.e., the temperature at 1.5 m height) of the JMA-NHM was calculated by interpolation between the temperature at the lowest atmospheric level and that of the surface (SLAB scheme) or the canyon air (SPUC scheme), considering the stability of the surface layer. Note that the temperature observation height was 1.5 m at AMeDAS stations, but it was 3.0 m at the Kugahara station.

Comparing the results of SPUC scheme with and without considering the anthropogenic heat (indicated as +AH and noAH in Fig. 3.9), a large contribution of anthropogenic heat in better reproduction of surface air temperature can be seen. The anthropogenic heat raises the calculated temperature throughout the day, especially in the dense urban area. Figure 3.10 illustrates the time series of the amount of anthropogenic heat in the form of sensible and latent heat released to the five grids. In Tokyo, a well-established office area, the anthropogenic sensible heat added nearly 80 W m^{-2} during the daytime and about 10 W m^{-2} to the minimum during the nighttime. This heat release introduces some biases on the surface air temperature. With such contribution of anthropogenic heat release, the SLAB scheme would also have similar performances to the SPUC scheme. The comparison on Fig. 3.9 between the runs of SLAB and SPUC without considering anthropogenic heat, however, also shows some differences. These differences are regarded as the result of scheme differences on treatments of radiation distribution, heat exchanges among surfaces and so on. And the SPUC scheme shows some improvements of reproduction of daytime air temperature at Nerima and Kugahara. For Kumagaya, differences were seen between the

SPUC and SLAB runs only during the early morning. Because of the sparser setting of buildings at Kumagaya, that is, the lower S_f value of the grid than at denser grid like at Tokyo, the behavior of the SPUC scheme asymptotically approaches that of the SLAB scheme. This feature can be well adapted to the mixed use of SPUC and SLAB schemes in the JMA-NHM mesoscale model since it prevents large differences between grid cells using SPUC and SLAB schemes. The nighttime temperature rise in the SPUC run compared to that of the SLAB run can also be seen in the rural grid of Hatoyama. Heat advection from neighboring urban grids is considered to be one cause for this difference.

The time series of the temperature at Kumagaya and Hatoyama was not reproduced well by both the SPUC scheme and the SLAB scheme. The JMA-NHM removed clouds over those stations earlier than the observed data during the afternoon, such that the downward shortwave radiation was overestimated. Figure 3.11 shows the observed daylight duration and the simulated downward shortwave radiation at the two AMeDAS stations of Tokyo and Kumagaya. The observed daylight duration suggests that it was clear throughout the day around Tokyo; and based on the simulated downward shortwave radiation, the JMA-NHM could reproduce the clear weather conditions on that day. However, the daylight duration was short in the afternoon, especially after 1500 JST at Kumagaya, suggesting that it was cloudy. But the values of the simulated shortwave radiation remained large after 1500 JST. This discrepancy can explain the overestimation of surface air temperature around Kumagaya (and the nearby station of Hatoyama).

3.2.3 Surface energy balance

Figure 3.12 illustrates the time series of the surface energy balance at Kugahara on 20 August 2005. The in situ flux observation took place there, and some selected data were available for the model evaluation. For the observational data, we calculated the conduction heat flux to the ground (red dots) as the residual of net radiation and sensible and latent heat fluxes. In the SPUC run, the fluxes in Fig. 3.12 are the grid-averaged values, that is, the area-weighted average over

the facets within the grid. Table 3.2 shows mean bias errors and root mean square errors of the simulated radiations and heat fluxes estimated on the 24 observed values.

First, we compare simulation results with the observed data. The net radiations of the SPUC and SLAB runs are underestimated up to 100 W m^{-2} around noon, and the mean bias errors are around from -25 to -28 W m^{-2} (see Table 3.2). By comparing the individual components of radiation, we can see the underestimation of downward shortwave and longwave radiation in both run. This is likely associated with the atmospheric radiation process of the JMA-NHM itself. On the other hand, overestimation of upward shortwave radiation and underestimation of upward longwave radiation can be seen in the SLAB run. This seems to be the result of setting the albedo at too large a value. The large albedo setting makes larger upward shortwave radiation. It also effects the lower surface temperature and then it generates lower upward longwave radiation. The upward radiations were improved in the SPUC run because of the reduced effective albedo in this scheme considering the reflection process in the canopy layer. The latent heat fluxes in the two simulations are much smaller than the observed values (with the mean bias error of -43.0 W m^{-2} in the SLAB run and -53.1 W m^{-2} in the SPUC run), which can cause larger sensible heat flux than the observation. The settings of wetness of the ground surfaces should be refined in both schemes.

As seen above, the SPUC itself improves the outgoing radiative fluxes by reducing their biases. However, Table 3.2 also shows the better performance of the SLAB for both turbulent heat fluxes. It would suggest that the increase in daytime temperature observed in Fig. 3.9 is most likely due to an overestimation of the daytime sensible heat flux from the SPUC; in other word the SPUC is probably performing better in terms of simulated air temperature (Fig. 3.9) but for some reasons of the JMA-NHM performances other than the land surface scheme.

Next, we compare the SPUC run with the SLAB run. The incoming radiation components of the two runs are almost the same, but the upward shortwave and longwave radiations of the SPUC scheme are clearly improved. The mean bias errors changed from 19.3 W m^{-2} to 0.3 W m^{-2} for the upward shortwave radiation, from about -29.6 W m^{-2} to -13.0 W m^{-2} for the upward

longwave radiation. The upward shortwave radiation is modified by the urban canopy structure because of the sunlight factor in the SPUC run, which decreases the upward shortwave radiation (decreases the effective albedo). The upward longwave radiation during daytime was larger in the SPUC run than in the SLAB run because of the higher surface temperature caused by the lower effective albedo.

The turbulent sensible and latent heat fluxes are also modified when using the SPUC (The lower panel of Fig. 3.12). The difference of sensible heat flux can be seen in the daytime between the SPUC and SLAB. Almost 40 W m^{-2} of the daytime anthropogenic heat at Kugahara (see Fig. 3.10) is the main factor. However, the difference between the SLAB run and the SPUC run without anthropogenic heat is also seen. The difference comes from the scheme differences such as the treatment of radiation distribution, heat exchanges among the surfaces, and so on. The large difference also occurred in the latent heat flux in the daytime. The setting of wet area fraction, i.e. the ground area fraction, directly affected this difference. The optimal settings of wet area fraction and wetness of the ground are one of the key for good reproduction of heat fluxes not only in the SPUC scheme but also in the SLAB scheme, though it is very difficult to get representative wetness for each grid of the mesoscale domain. Concerning the anthropogenic latent heat, differences of latent heat flux between the SPUC runs with and without anthropogenic heat is very little. The increase of biases in the run with anthropogenic heat is only about 1.9 W m^{-2} in this study (Table 3.2).

This comparison shows the needs of further studies improving the expression of moisture source among urban area and setting more adequate thermal parameters of the surfaces in both the SPUC scheme and the SLAB schemes with taking the total performance of the JMA-NHM into account. The worse reproduction of turbulent heat fluxes in the SPUC run, in spite of the improvement of radiative fluxes, can be caused by the rough parameterizations of turbulent transfer from the previous vegetation canopy scheme (Eq. 3.7 and 3.8). Further comparative studies of radiation and heat flux balances shall be done between the mesoscale simulation and observation in the urban area.

3.2.4 Water storage performance

In the calculation for 12 and 13 August 2005, a rain event was simulated. Figure 3.13 shows the time series of predicted latent heat flux, water volume on the roof and walls, and the precipitation observed at the AMeDAS station of Nerima and simulated using the SPUC scheme at the corresponding grid. The SPUC scheme reproduced the precipitation quite well. Although we cannot observe any black bar in the bottom of Fig. 3.13, the light rain was reproduced during the early morning of 12 August and the water volume on the roof and walls increased. During the daytime of 12 August, the latent heat fluxes from the roof and the walls were calculated. A heavy rain occurred during the nighttime of 12 to 13 August, and the water volume of the roof and walls increased and reached the maximum volume at around midnight. The latent heat fluxes from the surfaces, however, were very small during the nighttime, because of the small difference between the temperature of the surfaces and that of the canyon air. After sunrise, the latent heat flux from the roof increased to a maximum of 140 W m^{-2}. The walls became dry by noon of 13 August, whereas the roof remained wet until the evening of 13 August. After the roof became dry, no latent heat flux occurred. The evolution of the water storage and latent heat fluxes are physically reasonable.

3.3 Evaluation of the surface air temperature in a 1-month simulation

To estimate the effect on the surface air temperature calculations by coupling the SPUC scheme to the JMA-NHM with the consideration of anthropogenic heat release, we estimated the mean bias errors and their standard deviation from the observations (AMeDAS data) by performing a 1-month simulation for August 2005. The initial time of the simulation was 0900 JST of each day. The forecasting time was 39 h, and the last 24 h were used for analysis, as explained for the previous model evaluation. For comparison with the ordinary SLAB scheme, we set the same domain, initial conditions, boundary conditions, and forecasting times as in the SPUC run.

First, we evaluated the mean bias errors at the four typical observatories (Tokyo, Nerima, Kumagaya, and Hatoyama; see Fig. 3.8). Figure 3.14 shows daily time series of the composite mean of bias errors and standard deviations during the simulation term (1-31 August 2005). It is clear that the SPUC scheme generally improves the negative bias in Tokyo and Nerima, though positive biases appear from 1500 to 1800 JST at Tokyo and from 1800 to 2100 JST at Nerima in the SPUC run. At the central urban area such as Tokyo and Nerima, the anthropogenic heat has a large contribution to the improvement of negative biases. The modifications of radiation distribution and heat exchanges among canyon surfaces in the SPUC scheme, however, have some effects on the improvement during the daytime as evaluated in the previous section. At Kumagaya, the reproduction of surface air temperature by the SPUC run is similar to that by the SLAB run, except that the mean bias error of the SPUC run is higher during the daytime and lower before sunrise. This similarity is expected, as the SPUC scheme asymptotically approaches the SLAB scheme as the building area fraction decreases. At Kumagaya point, the nighttime cooling of SPUC run seems to be larger than that of the SLAB run. Because Kumagaya is one of sparse residential area, the radiative cooling could be larger than the radiative trapping inside the canyon. The settings of wooden housing parameters could also be the causes. The effects of heat storage by wooden housings are weaker than those by concrete condominium buildings. The considerations of spatially variable building types or canopy structure in urban grids are our next task. The higher mean bias errors of the surface air temperature in the SPUC run can be seen even in the rural area of Hatoyama, especially during the evening time and nighttime from 1500 to 2400 JST. The temperature rise at Hatoyama resulted from the advection effect of warmer air from urban grids, as mentioned in the previous section.

Figure 3.15 shows the differences in averaged surface air temperature at Tokyo, Nerima, and Kumagaya in order to emphasize the differences between the SPUC run and the SLAB run. The daily variation patterns of differences are the same during the daytime in the three urban grids, but the patterns are quite different during the nighttime. Because the anthropogenic heat releases in these grids are not very different during the nighttime, it cannot explain the differences in

the patterns. Rather, the large nighttime differences seem to arise from the differences in the radiation redistribution inside the canyon according to the various building coverage ratios, or the differences in heat flux exchanges to the atmosphere may play some role. In the grid with a low density of buildings (Kumagaya), the wind velocity inside the canyon would be larger, as estimated with Eq. (3.7). The energies would be well mixed in the canopy layer and well transferred to and from the atmosphere. Figure 3.16 shows mean bias errors and their standard deviations applied to all AMeDAS data mapped on the urban grids. The panels represent the mean bias errors estimated for (a) all days, (b) the 11 clear days, (c) the 11 cloudy days, and (d) the 9 rainy days, respectively. The weather conditions for each day were based on the AMeDAS observational data. Clear days were defined as follows. First, we calculated the monthly averages and standard deviations of daily total daylight duration at each AMeDAS station. Next, we set flags for clear days at each station if the daily total daylight duration was longer than the monthly average plus half of its standard deviation. Finally, we selected a clear day to analyze when 50% of stations in the forecasting domain had clear-day flags. We defined a rainy day as when 50% of stations in the forecasting domain recorded a daily total rainfall of more than 1 mm. Cloudy days were the rest of the days in the month.

The improvement of the negative mean bias errors in the SPUC run compared to those of the SLAB run was apparent under clear and cloudy conditions especially from afternoon to evening. In other words, surface cooling was suppressed and more realistic surface temperatures were obtained in SPUC compared to SLAB for these weather conditions, though reversed positive biases were partly obtained with SPUC. The larger sensible heat fluxes during afternoon were one of the main causes of it at sparse residential grids. Meanwhile, the addition of anthropogenic heat is relatively important at the center of Tokyo metropolitan area. The smaller standard deviations for the clear days imply that the forecasting scores were more stable than in the other cases because of the better ability of JMA-NHM to reproduce radiation on clear days. To clarify the effect of the SPUC scheme, the time series of differences in mean bias errors between the SPUC and SLAB schemes under each weather condition are shown in Fig. 3.17. The SPUC effect

averaged over all urban grids is quite similar to the Kumagaya pattern shown in Fig. 3.15. Figure 3.17 shows that the patterns are not so different under any weather conditions, but the SPUC effect is rather apparent on the clear days.

The diurnal variation pattern of surface temperature and its mean bias errors in SPUC can be modified by changing some parameters in the SPUC scheme. For example, if we set realistic office building parameters (i.e., the parameters with concretes for roofs and walls) in business district, the temperature decrease during the nighttime becomes more reduced, owing to the larger thermal inertia. Setting a larger value of WAI can also flatten the nighttime cooling trend owing to the increased wall area and the larger effect of redistribution of longwave radiation inside the canopy layer.

Figure 3.18 shows the correlation coefficients at each valid time and the standard deviations during the one month simulations. The differences among the two schemes are small and variability on each day is very large. Slight improvement of correlation coefficients, however, can be seen in the morning times and evening times on the clear days case. In this study, we set the uniform settings of the buildings as wooden housings with same heights, shapes, and thermal parameters to all the urban grids of the domain. The setting having spatial distribution is only the area fraction of the building. The more realistically distributed settings of the building types, shapes, thermal parameters and so on will make more realistic reproduction of surface air temperature and will improve correlation coefficients of surface air temperature.

3.4 Summary

A SPUC scheme was developed and implemented in the mesoscale model, JMA-NHM. Three-dimensional radiation processes in the street canyon (which had almost the same configuration as that of Kanda et al. 2005b) were taken into account, and the precipitation interception by roofs and walls was considered as well. Considering that there are many buildings with various heights in real urban areas, the SPUC scheme models the transfer of sensible and latent heat

fluxes between the building roofs and the canyon air. However the bulk coefficient between the building surfaces and the canyon air is based on the formulation originally proposed for vegetation canopies. This coefficient will need to be re-examined based on flux observations gathered from cities.

From the evaluation with heat flux observations at Kugahara station, the forecasted upward radiations in the SPUC run showed some improvement compared with the SLAB run. The forecasted heat fluxes in the SPUC run, however, showed worse performances. The adequate parameter settings (especially concerning latent heat fluxes) is needed not only in the SPUC scheme but also in the SLAB scheme. In the comparative experiment between the SPUC and SLAB schemes in August 2005, the mean bias errors of the surface air temperature on an urban grid was slightly improved by applying the SPUC scheme. To better compare the performance of the two schemes, however, a period longer than 1 month should be examined.

At this time, we set the physical parameters of buildings to those of wooden houses, whereas real urban areas comprise many types of buildings, such as office buildings and residential reinforced concrete type condominiums. For a more accurate SPUC scheme, these parameter settings should be based on actual information, such as that gathered via high-resolution urban GIS. From the GIS information, we can classify areas into some categories of dense and sparse, office buildings and residential housings and so on. Then we can set building parameters along with those categories.

Table 3.1: Parameters of the building materials. The data are for standard Japanese wooden houses (ECCJ 2005)

Materials	Thickness (m)	Volumetric heat capacity ($J\ m^{-3}\ K^{-1}$)	Thermal conductivity ($W\ m^{-1}\ K^{-1}$)
Roof			
Slate	0.012	1.821×10^6	1.1980
Plywood	0.012	7.137×10^5	0.1860
Air Gap	0.010	1.190×10^3	0.0241
Plasterboard	0.012	1.029×10^6	0.1740
Wall			
Mortar	0.030	1.591×10^6	1.5120
Plywood	0.009	7.130×10^5	0.1860
Air Gap	0.010	1.190×10^3	0.0241
Plasterboard	0.012	1.029×10^6	0.1740

Table 3.2: The mean bias errors and root-mean-square errors of the SLAB run, the SPUC run considering anthropogenic heat (SPUC+AH), and the SPUC run without anthropogenic heat (SPUC noAH) estimated from the observations at Kugahara station on 20 Aug 2005.

	SLAB		SPUC + AH		SPUC noAH	
	Bias	RMSE	Bias	RMSE	Bias	RMSE
$S^{\downarrow}$	-15.4	24.0	-18.4	28.2	-18.3	28.0
$S^{\uparrow}$	19.3	32.2	0.3	13.1	0.3	13.1
$L^{\downarrow}$	-22.4	27.1	-21.0	26.1	-21.7	26.5
$L^{\uparrow}$	-29.6	30.8	-13.0	17.9	-15.4	20.7
R_{net}	-27.5	53.6	-26.7	55.3	-24.9	55.4
$H(+Q_s)$	0.8	39.4	30.4	63.6	13.2	48.1
$LE(+Q_l)$	-43.0	63.3	-53.1	77.7	-55.0	80.0
G	14.8	46.3	19.3	46.7	17.3	45.7

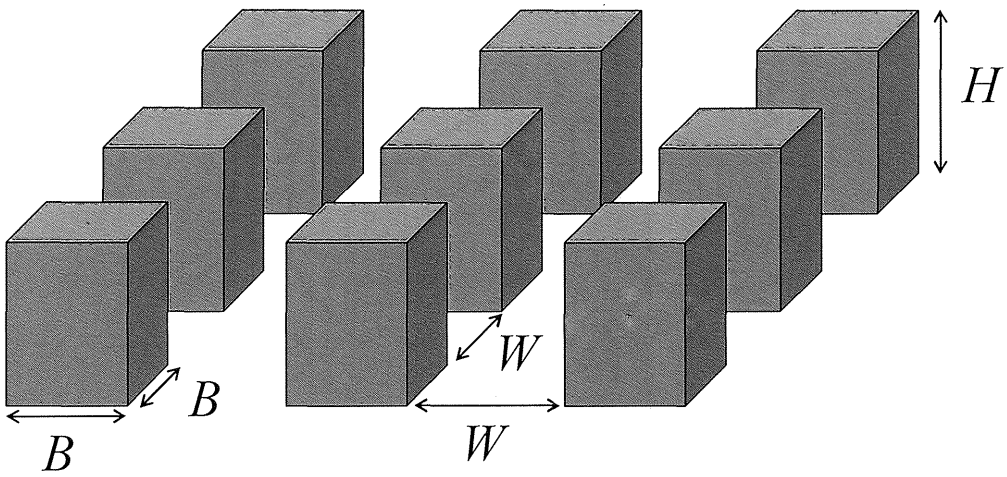

Figure 3.1: A schematic illustration of the dimensions of the scheme. The variables H and B represent the height and width of buildings, respectively; W represents width of the ground area inside the canyon. All building shapes are the same in one grid cell of the atmosphere model having a resolution of several kilometers.

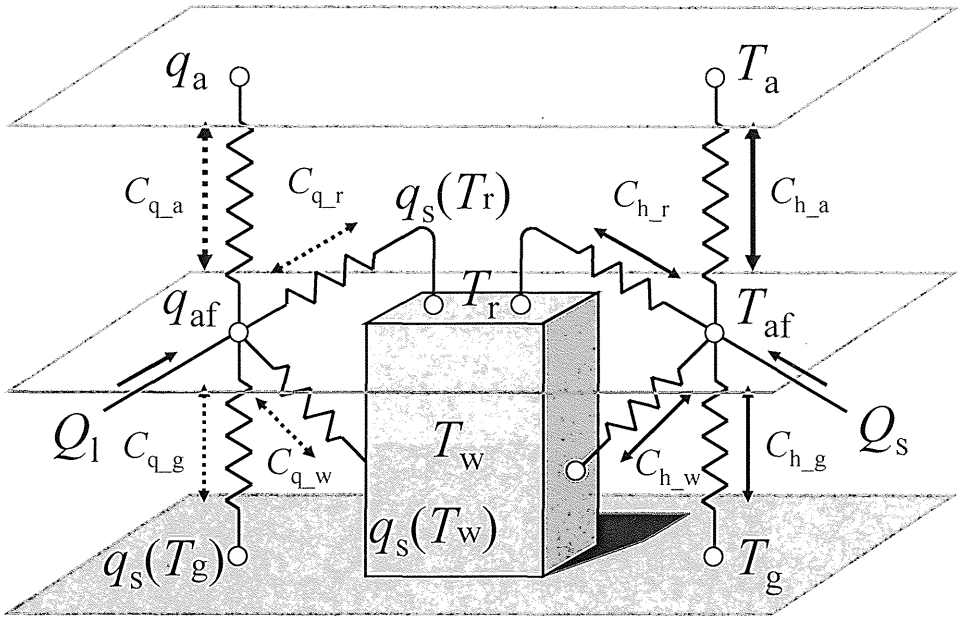

Figure 3.2: Flux circuit schematics, in which T, q, C_h, and C_q represent temperature, specific humidity, and bulk coefficients of sensible and latent heat, respectively. The subscripts a, af, r, w, and g represent the lowest level of the atmosphere, canyon air, roof, wall, and the ground. Here, $q_s(T)$ represents the saturated specific heat at temperature T, Q_s and Q_l represent the anthropogenic heat flux in the forms of sensible heat and latent heat, respectively.

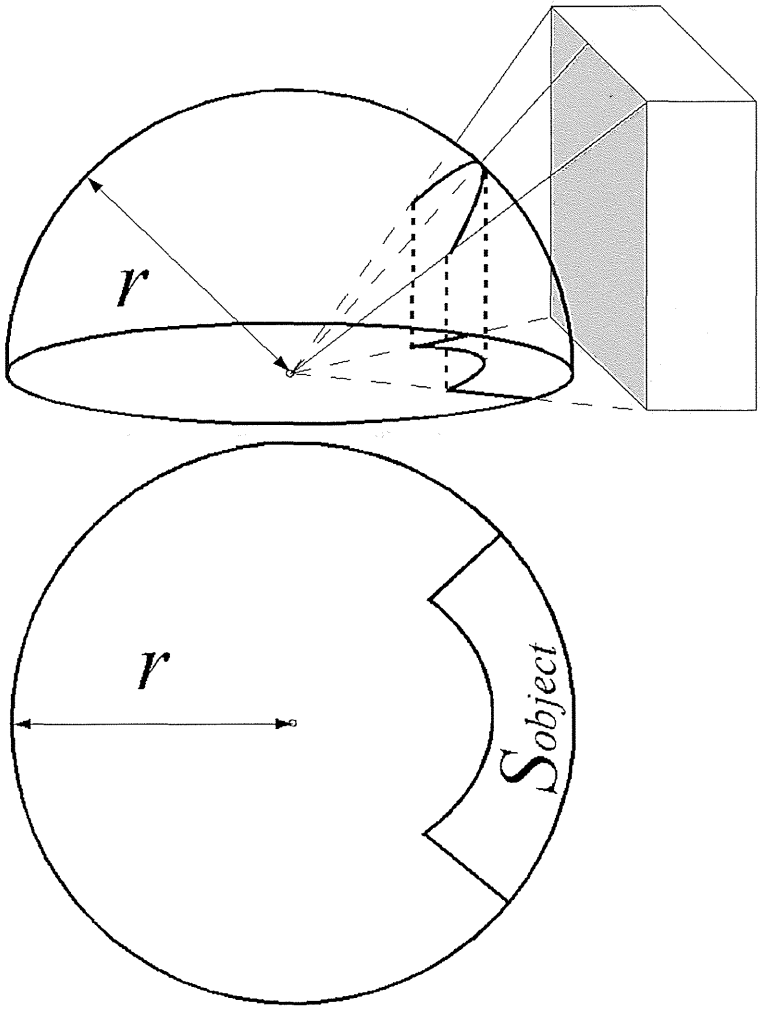

Figure 3.3: A schematic illustration of the sky-view factor. The area on the celestial sphere, with radius r, that is shaded by objects such as buildings is projected onto the horizontal plane orthographically. The sky-view factor is defined as the ratio of the residual area of the projected object S_{object} to the area of the celestial sphere circle πr^2.

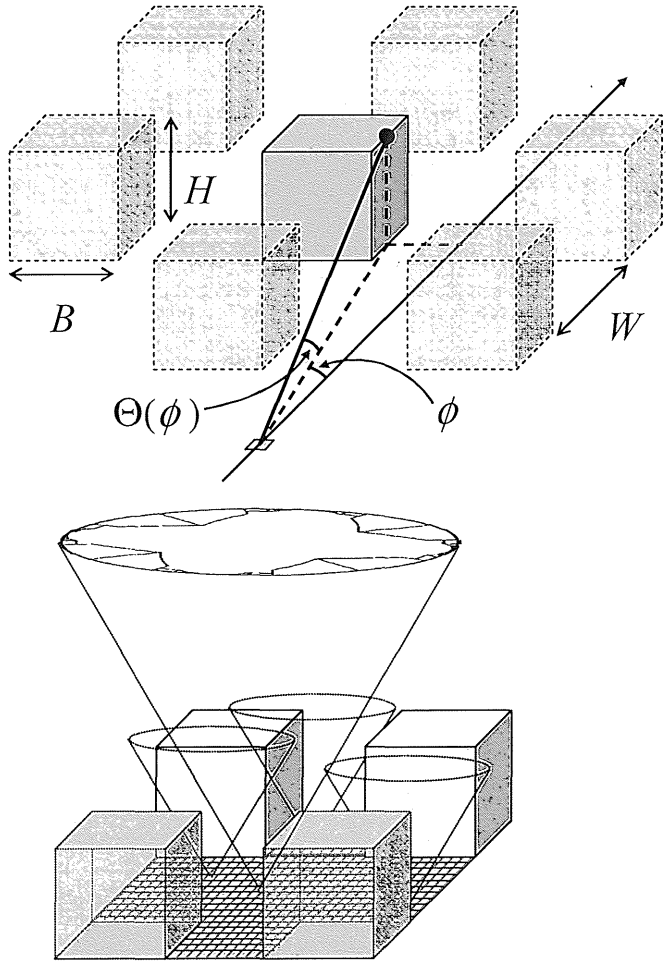

Figure 3.4: (top) A schematic illustration of angle definitions for the calculation of the sky-view factor. With changing azimuth angle ϕ, the envelope of the building roofs and walls can be determined. The envelope is expressed by $\Theta(\phi)$. The variables H, B, and W represent the height of the buildings, width of the buildings, and width of the road. (bottom) The small grid squares on the ground where the calculation of the sky-view factor is performed.

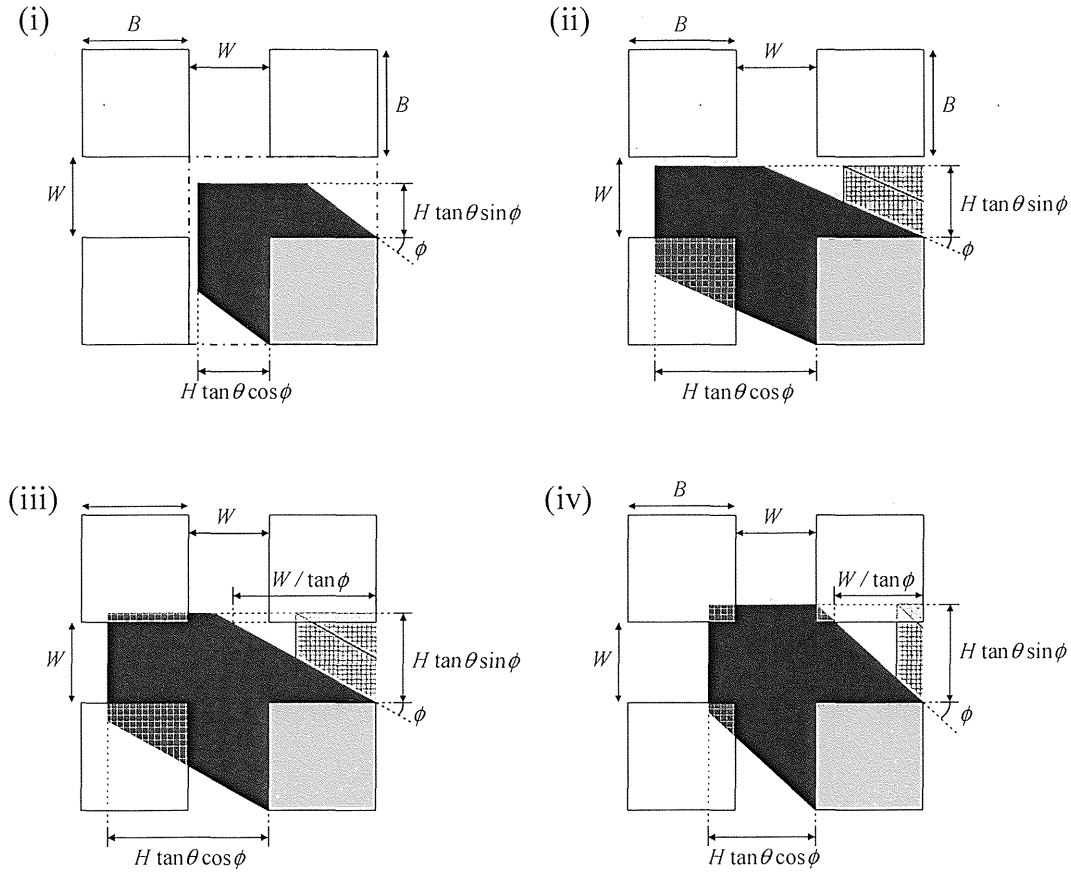

Figure 3.5: The four cases of the shadowing pattern. The dash-dotted square in (i) describes the unit area. Only the shadows that are cast in the unit area are shown. The black area is the shadow from the main building, and the gray hatched areas represent the shadows cast from another building. The variables H, B, W, θ, and ϕ represent the height of the building, width of the building, width of the road, zenith angle of the sun, and azimuth angle of the sun, respectively.

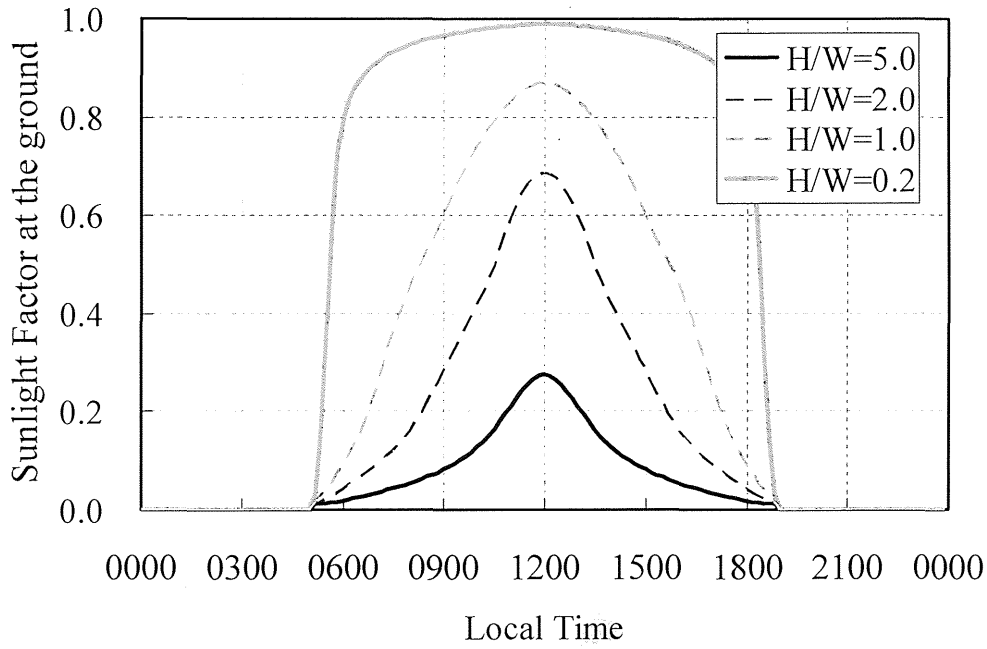

Figure 3.6: Time series of the sunlight factor at ground level. The calculation is performed with the square prism building array aligned regularly. The amount of sunlight that reaches the ground is small in a dense city, which is represented by a larger value of H/W. At dawn and dusk, the sunlight factor becomes small because the area of the shadow made by the buildings becomes large.

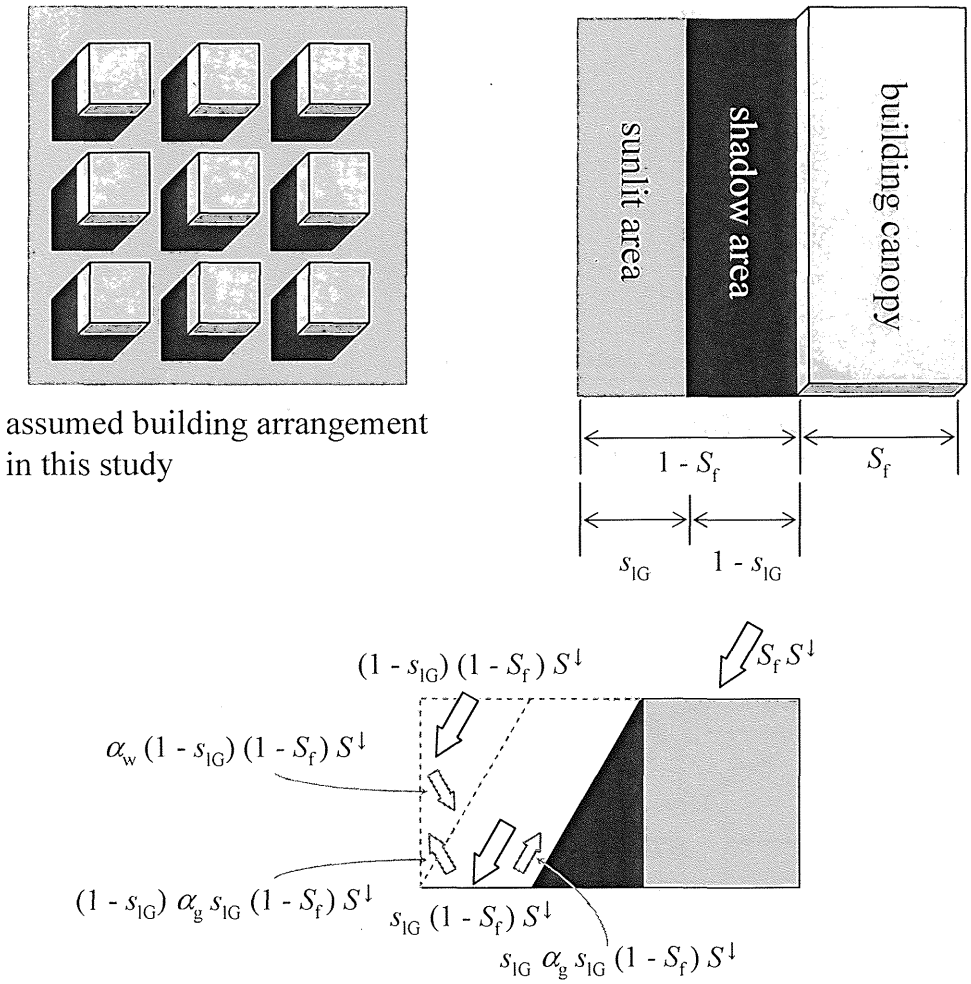

Figure 3.7: A schematic illustration for the distribution of short wave radiation. (left) The building arrangement in this study. (right) The area fraction images. (bottom) An image of short-wave radiation distributions (in Watts). Each term has to be divided by each area, S_f for roof, $S_f(\mathrm{WAI}-1)$ for walls, and $(1-S_f)$ for the ground, to estimate the radiant flux densities (W m^{-2}). The reflections are considered only once.

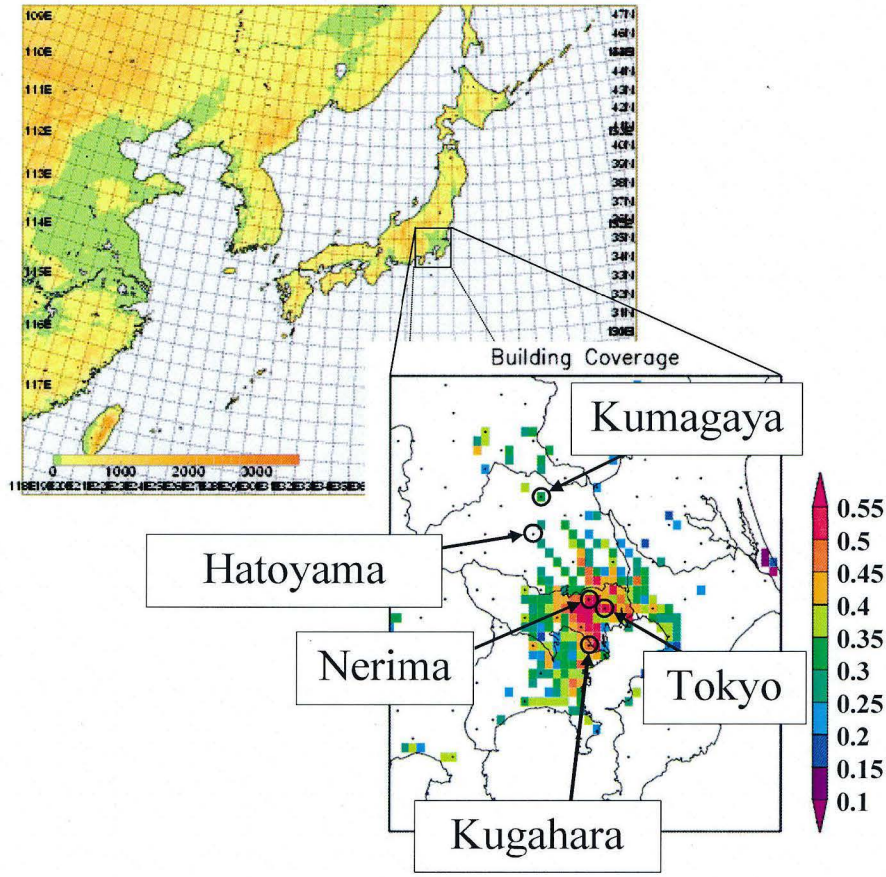

Figure 3.8: A closeup view of the area in Japan for which the simulations were conducted. The targeted area is the Tokyo metropolitan area. The locations of four AMeDAS stations (observatories of the Japan Meteorological Agency) are shown (circles): Tokyo is a dense commercial area, Nerima is a dense residential area, Kumagaya is a sparse residential area, and Hatoyama is a rural area. Radiation and heat fluxes were recorded at the Kugahara station, which is also a dense residential area. The colored grids in the bottom-right panel represent the grids to which the SPUC scheme was applied. The color scales represent the fraction of building coverage.

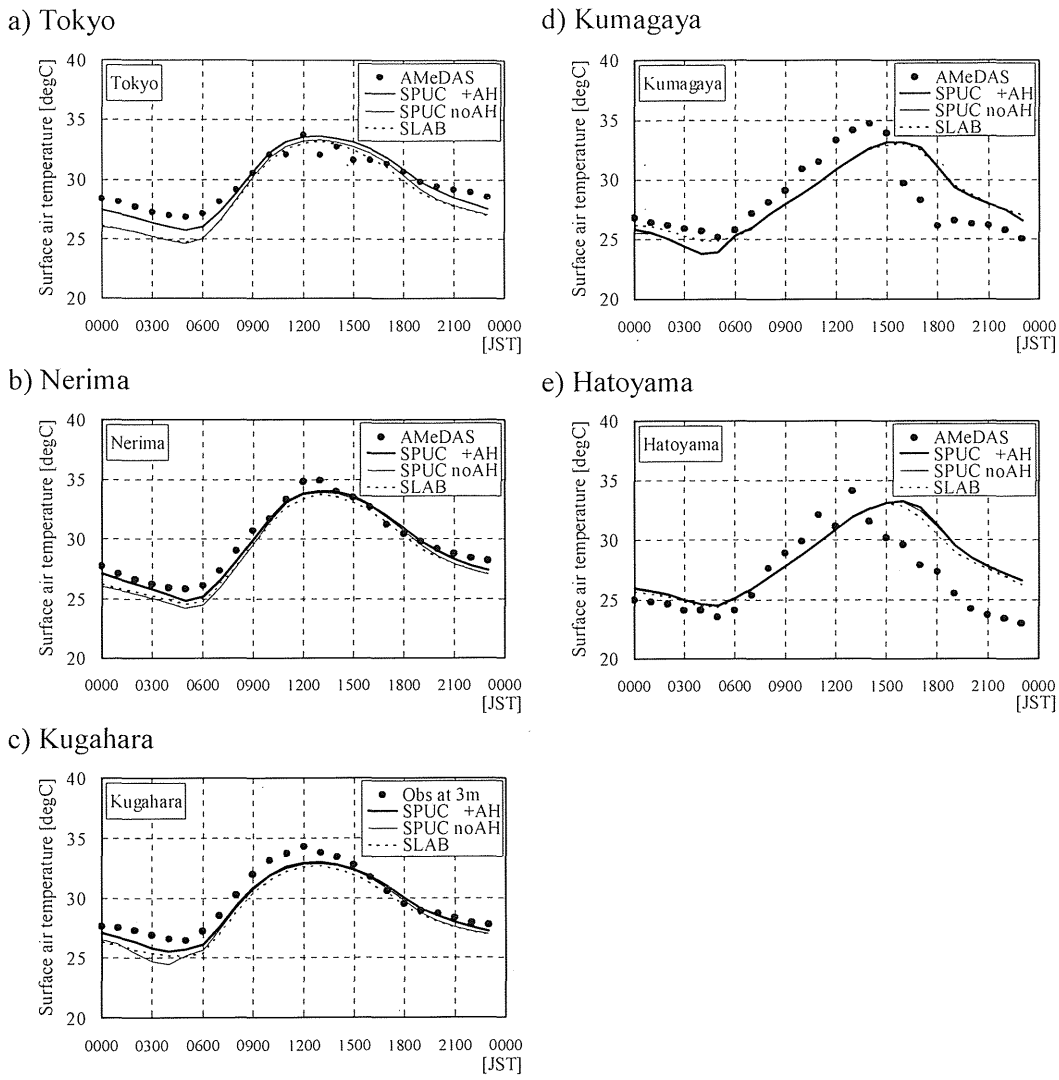

Figure 3.9: Time series of the surface air temperature simulated and observed on a typical clear day (20 Aug 2005) at the five observatories illustrated in Fig. 3.7. Kugahara is the station of the campaign observations of Moriwaki and Kanda (2004). The air temperature at 3-m height (the lowest height of the observations) is plotted for Kugahara, whereas temperature were recorded at 1.5-m height at the other four AMeDAS stations. The notations '+AH' and 'noAH' represent the simulations made with and without considering anthropogenic heat.

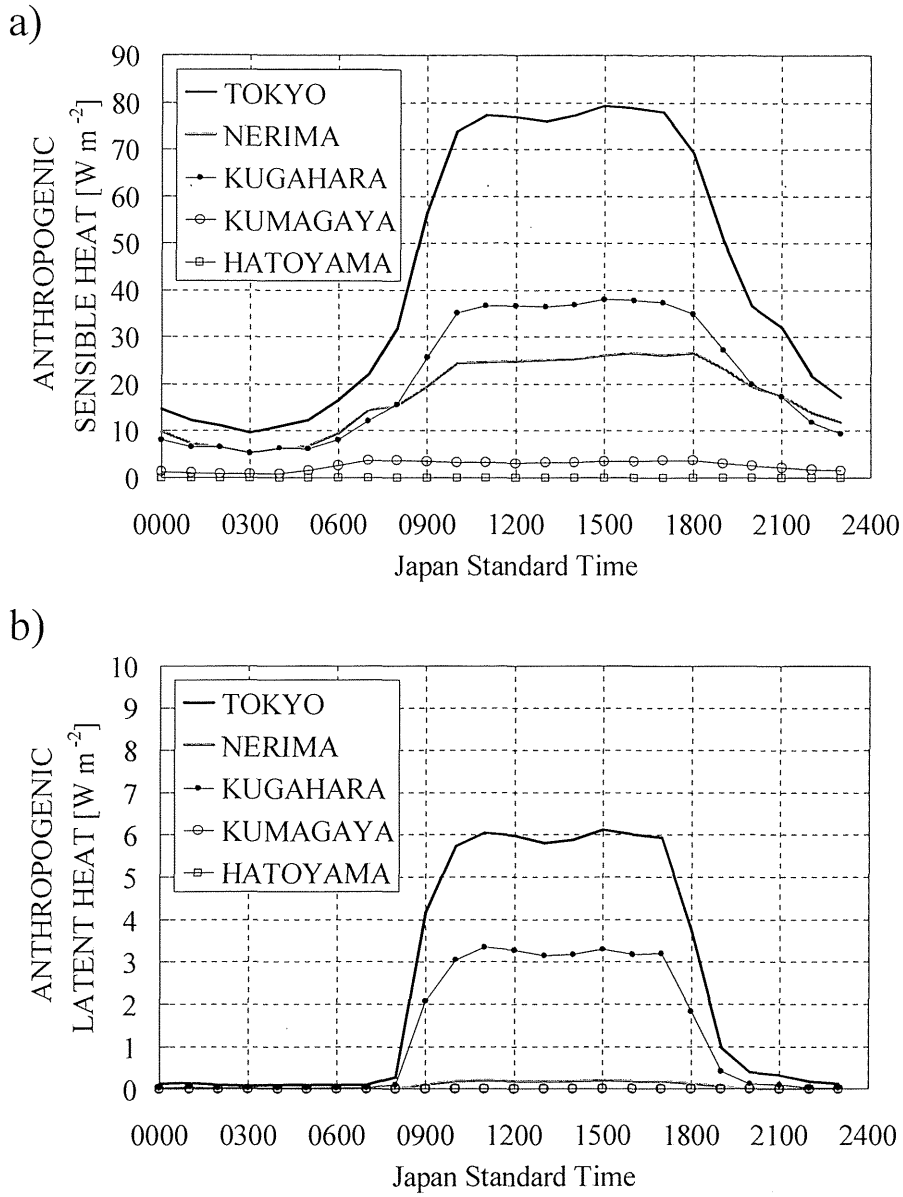

Figure 3.10: The time series of anthropogenic (a) sensible and (b) latent heat release at the Tokyo, Nerima, Kumagaya, and Hatoyama grid points. These values are averaged over each 4 km × 4 km grid.

a) Tokyo

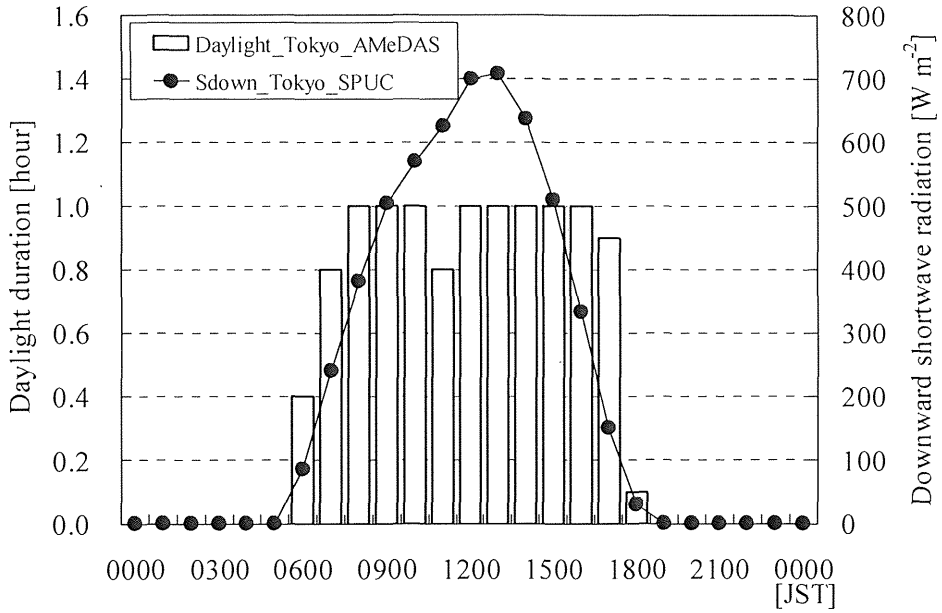

b) Kumagaya

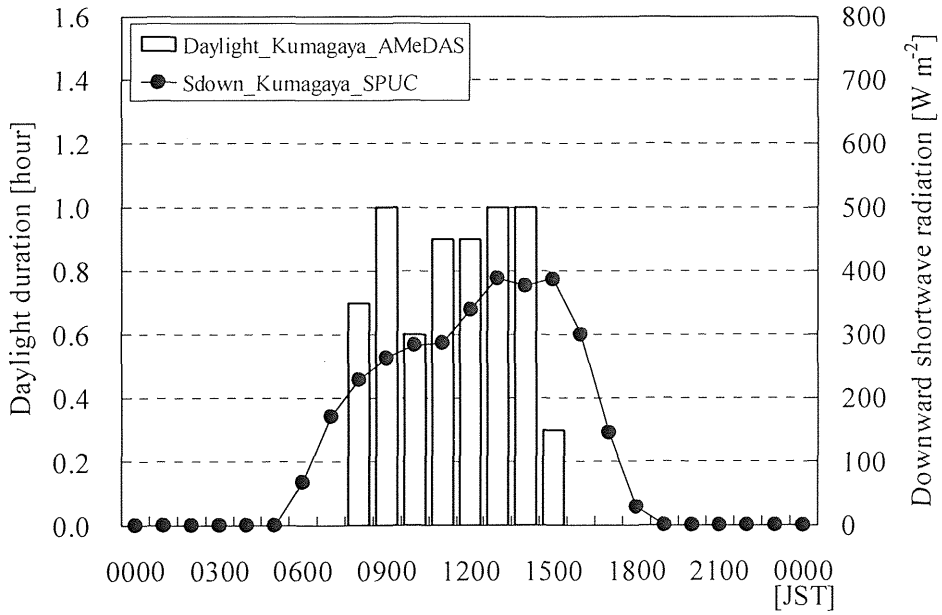

Figure 3.11: Time series of daylight duration (white bars) observed on 20 Aug 2005 at two AMeDAS stations: (a) Tokyo and (b) Kumagaya. The downward shortwave radiation (solid lines with dots) simulated by the SPUC run on the equivalent grid of the AMeDAS stations is also illustrated.

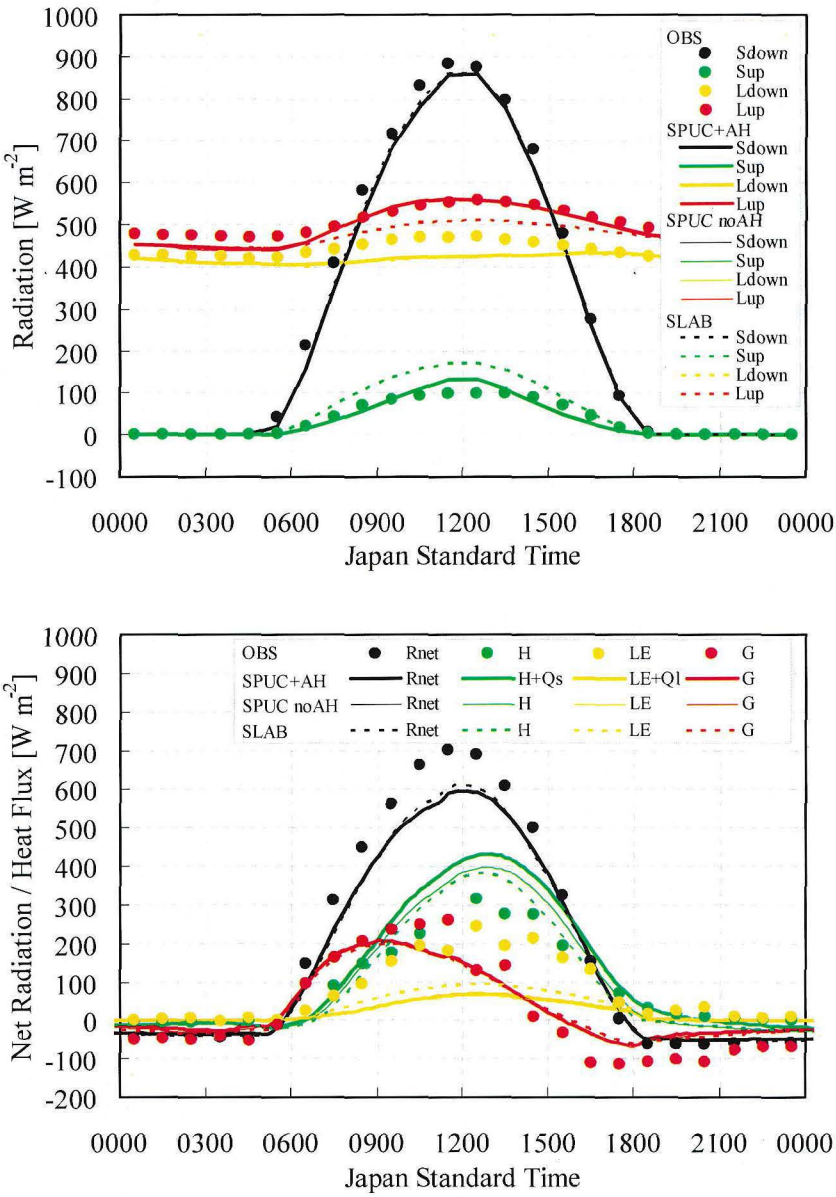

Figure 3.12: Time series of the observational data and simulation results of the (top) radiation balance and (bottom) grid-averaged turbulent heat fluxes at the Kugahara station on 20Aug 2005. In the top panel, S and L represent the shortwave and the longwave radiation, respectively, and 'up' and 'down' represent upward and downward radiation. In the bottom panel, R_{net}, H, LE, and G represent the net radiation, sensible heat flux, latent heat flux, and storage heat flux at the surfaces, respectively, and Q_s and Q_l are anthropogenic sensible and latent heat added to the canyon air. The variables of the SPUC run are averaged values of the roof, walls, and ground in the relevant grid. A notation 'noAH' indicates the results of the simulation made without considering anthropogenic heat.

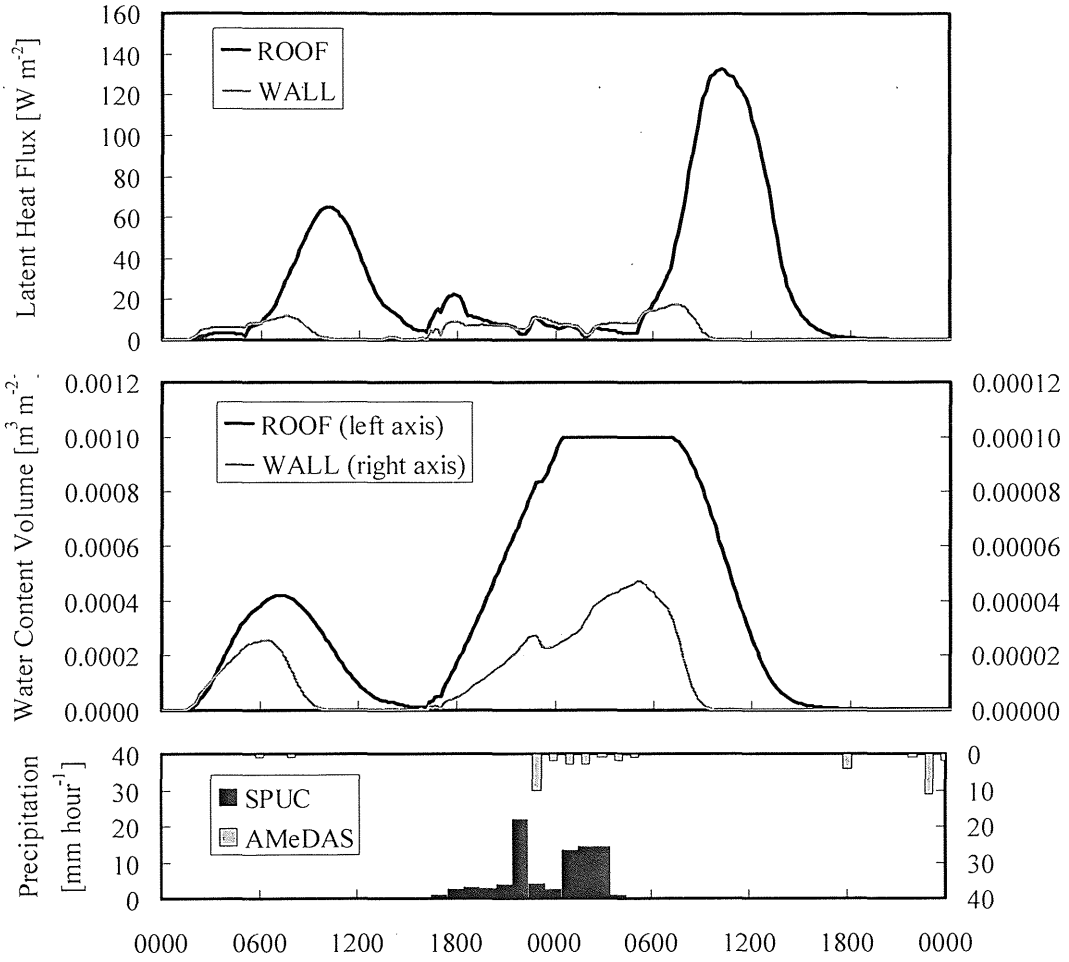

Figure 3.13: (top) Time series of the simulated latent heat fluxes from the roof and walls, (middle) the simulation results of the volumetric water content of the roof and walls, and (bottom) the time series of the precipitation simulated in the SPUC run and observed at the Nerima AMeDAS station.

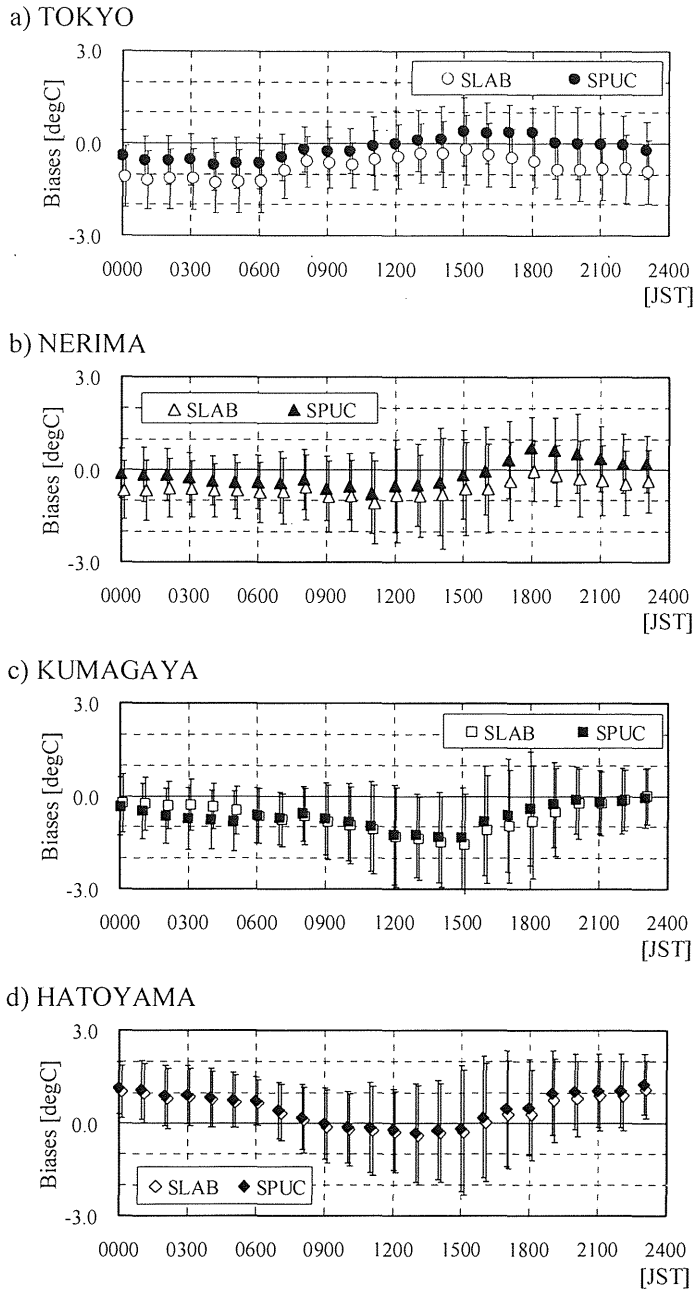

Figure 3.14: Average bias errors of the surface air temperature for the SPUC run and SLAB run for each time at four AMeDAS stations: (a) Toyo is a dense commercial area, (b) Nerima is a dense residential area, (c) Kumagaya is a sparse residential area, and (d) Hatoyama is a rural area. The vertical error bars represent the standard deviations of the mean bias errors for the 1-month simulation (August 2005).

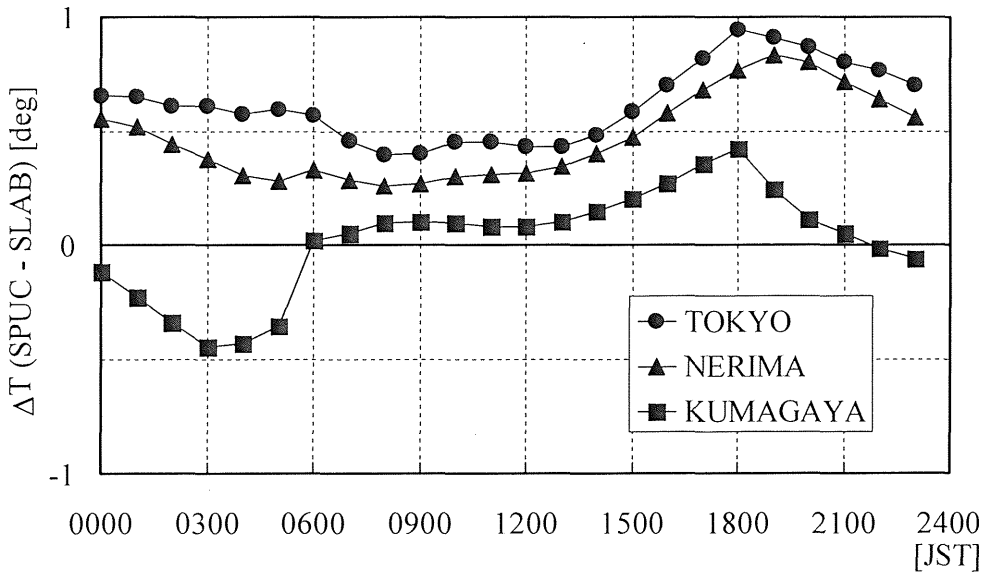

Figure 3.15: The differences in surface air temperature between the SPUC run and SLAB run at each time at the Toyo, Nerima, and Kumagaya stations.

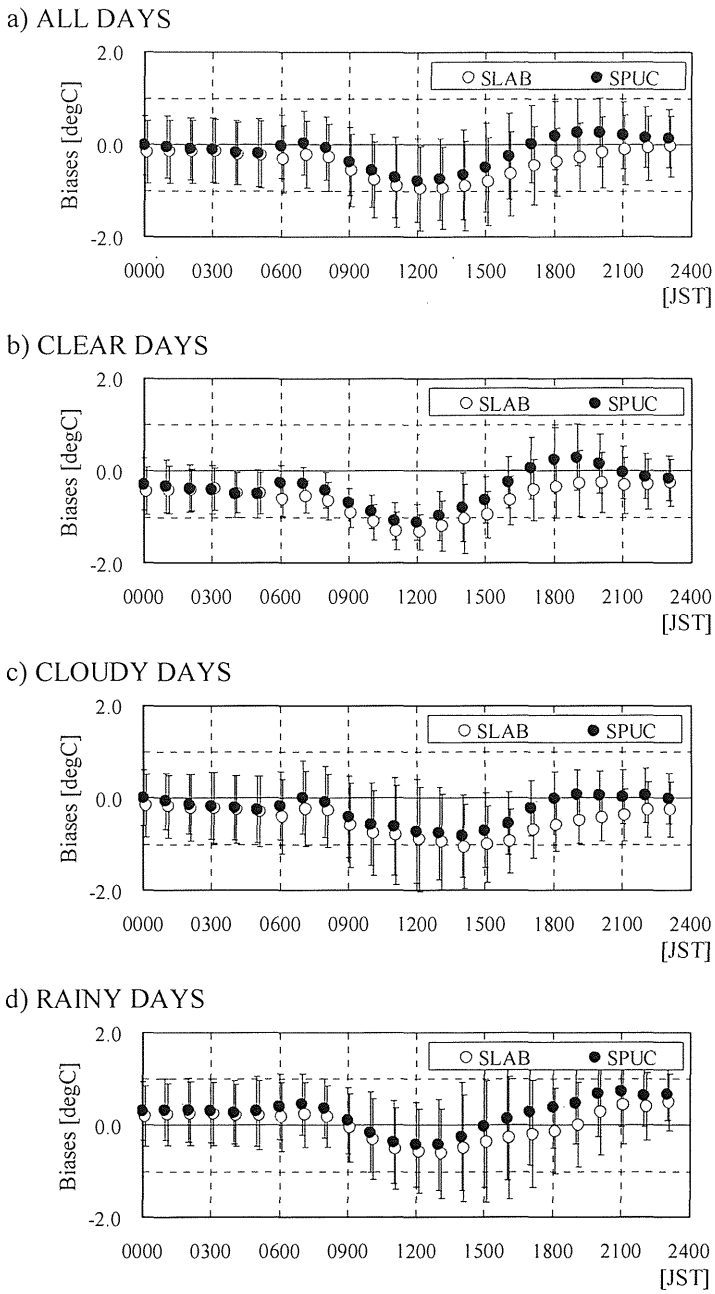

Figure 3.16: Mean bias errors of he surface air temperature by the SPUC run and SLAB run at each time estimated with all AMeDAS data mapped on the urban grids for (a) all days, (b) the 11 clear day,s, (c) the 11 cloudy days, and (d) the 9 rainy days in August 2005. Circles represent composite averages, and the vertical error bars represent the standard deviations of the mean bias errors. See the text for definitions of clear, cloudy, and rainy days.

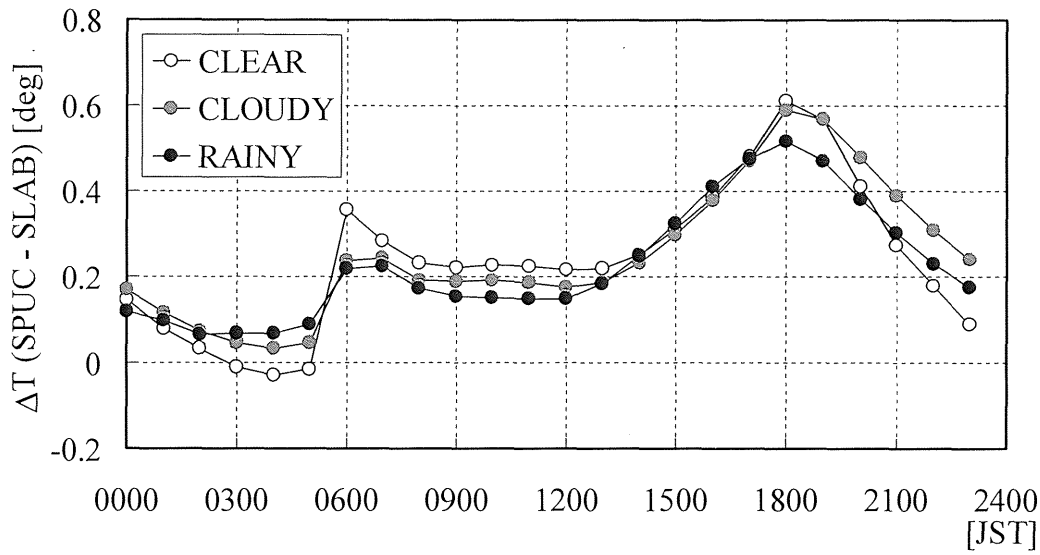

Figure 3.17: Differences in the mean bias errors of surface air temperature between the SPUC run and SLAB run at each time on the 11 clear days, 11 cloudy days, and 9 rainy days in August 2005.

a) ALL DAYS

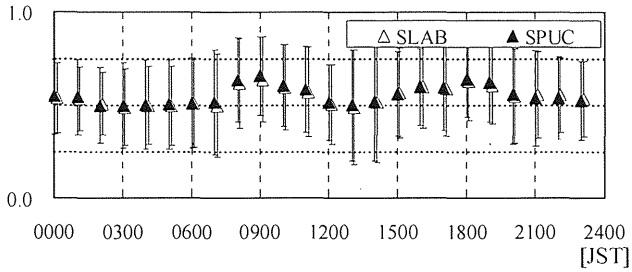

b) CLEAR DAYS

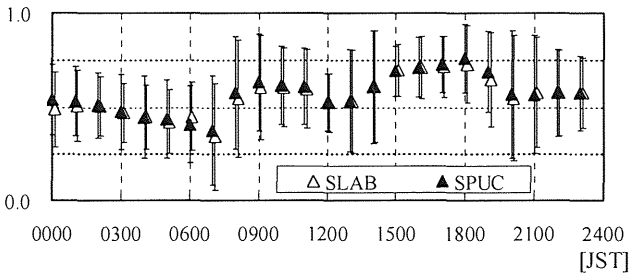

c) CLOUDY DAYS

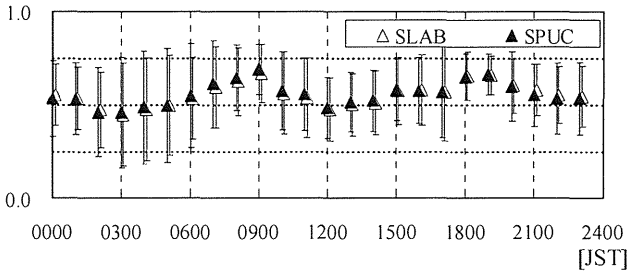

d) RAINY DAYS

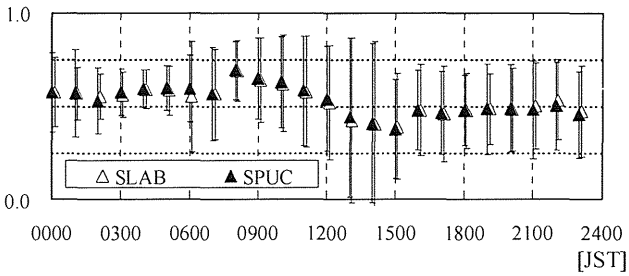

Figure 3.18: As in Fig.3.16, but for the correlation coefficients.

Chapter 4

Reproduction of Urban Warming in Kanto-Koshin Area during Recent 30 Years

4.1 Warming trends in Kanto-Koshin area

We will try to reproduce the warming trends in Kanto-Koshin area during this 30 years and figure out the contributions of each factor induced by the recent urbanization, utilizing the sophisticated urban parameterization scheme introduced in chapter 3. We will make brief review on the warming trends from 1976 to 2006 observed at AMeDAS stations as a first step. Figure 4.1 shows the distributions of seasonally averaged temperature trends for summer (July and August) and winter (January and February) as derived by a simple regression method. Only data without any statistical disconnection during the years of the study period were used. A bigger square represents a warmer trend at the station and a variety of symbols show the t-test significance levels. Table 4.1 lists the trends and significance levels at each station. Simple averaged warming trends were estimated to be a little less than 1.3 °C / 30 years for both summer and winter. Note that all of the trends were positive in both seasons. Among the trends with a significance level of over 80%, 8 stations (station IDs 42251, 48331, 48491, 48606, 48767, 49251, 44131, and 45401) had larger trends in summer than in winter and only 2 stations (41277 and 43156) had warming trends larger in winter than in summer. It can be seen that the inland warming trends were larger

than the coastal ones in both seasons.

Figure 4.2 shows the seasonal daily trends at the individual stations. The seasonal averages over 2 months of the 24-hourly surface air temperatures were determined and their yearly trends were estimated. Stations were classified into 3 types: A) stations with large warming trends during the daytime, B) stations with flat trends throughout the day, and C) stations with small warming trends during the daytime. The classification was performed as follows. First, stations with a standard deviation within 0.1 °C for each of 24 hourly values were categorized as group B. Next, the stations whose averaged trends during daytime (0600 - 1800 LST for summer, 0700 - 1700 LST for winter) were larger than during the night were categorized as group A. Other stations were categorized to group C. Following this procedure, for summer, 27 stations were sorted equally into groups A, B, and C. For winter, however, almost all of the stations were categorized as group C. Figure 4.2D shows the time series of differentials between the 1990's and 1980's climatic surface air temperatures around the Kanto-Koshin area as simulated by the Non-Hydrostatic Regional Climate Model (NHRCM; Ishizaki et al. 2009), downscaled from JRA-25 without any consideration of urban effects. Compared to the observational results, the warming trends of the NHRCM are considerably underestimated in summer and slightly overestimated in winter. Furthermore, the daily variations of the warming trends are very poorly reproduced. Such discrepancies are probably caused by the lack of urban effects in the NHRCM.

Next, by utilizing a meteorological mesoscale model, we investigate whether urbanization effects, such as the decrease of vegetation, increase of anthropogenic heat, and structural changes inside urban areas, can explain the average or the daily variation of these warming trends.

4.2 Experimental setting

The aim of this chapter was to check the reproducibility of the daily variations of observational warming trends during a 30-year period, as described in the previous section, using a sophisticated atmospheric model. In particular, we estimate the contributions of land surface modifi-

cations to the warming by altering the bottom boundary conditions of the atmospheric model. A brief introduction to the atmospheric model and urban parameterization scheme coupled to the model is presented in this section. The specifications of the initial and boundary conditions, the settings, and the data used in the reproduction and some sensitivity experiments are also described.

4.2.1 Atmospheric model

The base model used in this study is the Japan Meteorological Agency Non-Hydrostatic Model (JMA-NHM; Saito et al. 2007). The JMA-NHM is a fully compressible atmospheric model that was adopted as an operational regional mesoscale model at the JMA. The main specifications are described in Table 4.2. We selected the operational settings for almost all of the settings for the model. For urban grids, however, we adopted the single-layered urban canopy scheme of Aoyagi and Seino (2011) instead of the default simple slab type surface scheme. This urban canopy scheme is an extended version of the energy balance scheme of urban canopy models originally proposed by Masson (2000) and Kusaka et al. (2001) . The 3-dimensional consideration of the estimation of radiation distributions by building canopies and the consideration of latent heat fluxes from stored water on the building surfaces are parts of our urban scheme in this study, which we extended from the original models. Figure 4.3 shows schematic images of a flux circuit of this urban canopy scheme and an ordinary slab scheme. The application of the urban canopy scheme enables us to describe urban radiative effects and the modifications of heat fluxes from the canopy surfaces.

Using this atmospheric model, we executed several simulations of the Kanto-Koshin area with a horizontal grid scale of 4 km. Operational mesoscale analysis (MANAL) data of the JMA were used as the initial atmospheric conditions. For summer simulation, MANAL data of 25 June 2006 0000 UTC were used as the initial condition. Continuous integration over about 2 months was executed while providing the 3 hourly MANAL data as lateral boundary conditions

of the simulation. After about 1 week spin-up, the half hourly output from 01 July 2006 0000 UTC to 31 August 2006 2330 UTC was used for the analysis. For winter simulation, MANAL data from 25 December 2006 0000UTC were used as the initial conditions and simulated data from 01 January 2007 0000 UTC to 28 February 2007 2330 UTC were used for the analysis.

4.2.2 Land use settings

The land surface parameters used as the bottom boundary conditions were derived from the 1976 and 2006 versions of the National Land Numerical Information (land use data) provided by the Ministry of Land, Infrastructure, Transport and Tourism of Japan. The area fractions of 11 types of surface categories are stored in the land use dataset with a grid spacing of about 100 m. A stacked bar chart of occupancies and a bar chart of the increase or decrease of each category from 1976 to 2006 in the study area are shown in Fig. 4.4. It is obvious that the building lot area increased significantly and vegetation areas of paddy field, farm area, and forests decreased. Note that the golf area was re-categorized in the newer version of the land use data and thus divided from the forest area. We assumed that the 3 categories of building lots, road, and unclassified area were urban surfaces. The bottom image in Fig. 4.4 shows the horizontal distribution of urban surface fraction differences between 1976 and 2006. Over almost all of the study area, the urban area increased. The increased area of urban surface is clearly seen in the northern part of the Kanto Plain, in the area surrounding Tokyo's 23 wards, along parts of the coastline, and along some of the trunk railway lines and highways. It is noteworthy that the area fraction of urban surfaces did not change in central Tokyo. This implies that by 1976 the urban surfaces had already been saturated in central Tokyo.

The 4-km grids that are covered with over 50% of urban surface are referred to as "urban grids" in this study. We applied the urban canopy scheme to the urban grids in order to consider the effects of buildings on radiation distribution and heat transfer. Buildings were assumed to occupy 60% of the building lots and to be regularly arranged in an urban grid with an average

height of 10 m. The residual 40% of building lots and the other types of surfaces were assumed to be ground area in urban canyons. The parameters of the ground area were set by a weighted average by area of the parameters listed in Table 4.3, such as wetness, albedo, volumetric heat capacity, and thermal conductivity. Table 4.4 shows the parameters of the office buildings considered in the urban canopy scheme. We applied the slab surface scheme for the other non-urban grids. The parameters for the slab scheme were also set by the area-weighted average values of Table 4.3.

4.2.3 Anthropogenic heat load

The heat load due to human activity has one of the largest impacts on the surface air temperature. We used the realistic anthropogenic heat distributions with daily variations proposed by Senoo et al. (2004). This anthropogenic heat model does not consider any heat pump effects as more sophisticated building energy analysis models (Kikegawa et al. 2003; Ohashi et al. 2007) used to estimate the heat released from buildings do. However, the heat transmitted into the building from the exterior environment through roofs and walls was released efficiently in the form of heat fluxes from the surfaces owing to insulation layers and air spaces, as listed in Table 4.4. Although the original dataset was provided with a grid resolution of 10" in latitude and longitude (about 250 m x 300 m), the values were averaged with a resolution of 4 km for this study. Anthropogenic heat was loaded only onto the urban grids in the simulation for 2006. Because the anthropogenic heat dataset had been prepared only for the Tokyo Metropolis and 6 prefectures around Tokyo, the anthropogenic heat was set to 0 for any urban grids in other prefectures. Figure 4.5 shows the horizontal distributions of the average anthropogenic heat in summer and winter. The heat was loaded in the form of sensible and latent heat fluxes. It can be seen that anthropogenic heat is concentrated around central Tokyo. The amount of heat in that area is 10 W m^{-2} larger in winter than in summer. The unique daily variation was considered at each urban grid. As an example, the bottom plots of Fig. 4.5 show time series of the anthropogenic heat at the Tokyo grid.

4.2.4 The building aspect ratio

Modifications of the aspect ratio of urban buildings during the 30-year period were also considered. The urban canopy scheme used in this study assumed that all buildings were square prisms in shape. Thus, the only parameter specifying the building shape was the ratio of height to width (H/B). In the experiments for 2006, the H/B ratios were set from the GIS dataset of the Tokyo Metropolis assessed on 2001 and 2002. The datasets consist of several million polygons, each representing a building in the Tokyo Metropolis. Figure 4.6 shows the horizontal distribution of 100 m grid averaged H/B datasets. It can be seen that the H/B values are larger (about 1 - 3) at the center of the urban area and smaller in the suburban area and in the western rural areas of Tokyo. We averaged these data into 4 km grids. We applied a value of $H/B = 0.75$ (the modal class of the histogram at 0.25 intervals) to the urban grids of the other prefectures, where there was no information on the building aspect ratios. For the simulation of 1976, the Tokyo Metropolitan government (1977) reported that the achievement rate of the plot ratio averaged about one third (33.7%) for the private sector in 1975. Under the assumption that the legal plot ratio remained the same during the 30 years and that buildings have grown high enough to achieve the legal plot ratio, we supposed that the buildings were one third lower in 1976 than in the late 2000's. Thus we took the value of $H/B = 0.25$ for all the buildings in the simulations of 1976.

4.2.5 Experimental cases

Using the above-mentioned atmospheric model and settings datasets, we performed numerical simulations for various cases. Table 4.5 lists the bottom boundary settings for the experimental cases in this study. Note that only EXP2006HR, which used atmospheric data of 2006 (and 2007 for the winter case), the land use distribution of 2006, anthropogenic heat datasets of the 2000's, and building shape distribution data of the 2000's, can be called a "reproductive experiment". The other experiments were sensitivity studies for checking the effects of the bottom boundary conditions.

4.3 Results

4.3.1 Overall effects

The upper panels of Fig. 4.7 show the differentials of the surface air temperature averaged over 2 months between experiments EXP2006HR and EXP1976. Warming biases over almost the entire Kanto-Koshin area can be seen in association with the effects of land use change, anthropogenic heat load, and the increased building height. The positive bias was smaller along the coast and larger around the Tokyo Metropolitan area and in the inland urban area. Although the situations were similar in both summer and winter, the biases were larger in winter than in summer.

To determine the reproducibility of the real temperature trends over the 30-year period (Fig. 4.1), we examined the bottom plots in Fig. 4.7, which show scatter diagrams between the observational trends and the differentials (EXP2006HR - EXP1976) at the grid point where the corresponding station lies. A rough one-to-one relationship can be seen between them, although some points (Tokyo and Takada) deviate by quite a lot from the rest of the population. The correlation coefficients were 0.294 with a significance level of 90% for the summer case and 0.444 with a significance level of 99% for the winter case. The y-intercept around 1.0°C / 30 years can be recognized as the trend without urbanization effects, that is, the global warming trend. This estimated value is consistent with the temperature trend of approximately 0.3 °C per decade in the Northern Hemisphere for 1979 - 2005 reported by the IPCC (2007) .

Figure 4.8 shows the daily variation of temperature differences between EXP2006HR and EXP1976. Spatial averaging among all of the urban grids was performed in both experiments. A smaller temperature rise in the daytime and a larger one during the night, which is the same tendency as that of the observational trends (Fig. 4.2C), can be seen. The magnitude relation of the diurnal range (i.e., the winter case is larger than the summer case) and the magnitude itself are well reproduced if Fig. 4.2C is considered to be typical of daily variations affected by urbanization.

4.3.2 Sensitivity analyses

As mentioned in section 4.2.5, we performed additional experiments to identify how each factor affects the warming trends. The differentials of 2 months' average temperatures are shown in Fig. 4.9. The differentials are A) EXP2006 - EXP1976, B) EXP2006H - EXP2006, and C) EXP2006HR - EXP2006H, which represent the warming effects by the decrease of vegetation, the addition of anthropogenic heat, and the growth of building heights, respectively. Figure 4.10 shows the daily variation of the differentials averaged over all the urban grids for 2006.

The warming effect due to land use change, that is, area fraction changes, was larger in the area surrounding central Tokyo. The effect was also larger in inland urban areas. These areas experienced similar land use changes, namely, large decreases in the vegetation fractions, replaced by urban surfaces. Thus, the warming effect in the daytime can be explained by the well-known Bowen ratio effect. Along with vegetation decrease (the growth of urbanization), the latent heat fluxes from the surfaces become smaller and instead the sensible heat fluxes become larger. The larger sensible heat flux warms up the surface air. From the daily variation of the land use change effect (the lines with closed circles in Fig. 4.10), the variation seems to coincide with the movement of the sun during the day. This synchronous variation with sun movement supports the idea that the temperature rise was caused by the Bowen ratio effect. The result shows the point where the Bowen ratio effect was larger in the moist summer than in the dry winter. The figure also shows slight warming differentials during the night. Increased urban area in place of vegetation intrinsically led to more buildings, which resulted in the slight nighttime warming by inhibition of radiative cooling.

Figure 4.9B shows the horizontal distribution of the differentials of EXP2006H - EXP2006, representing the anthropogenic heat effect on the warming trend. Not surprisingly, the warming area was limited to around the area where anthropogenic heat was released. The warming rate in winter was around 2°C, and was larger than in summer (around 1°C). Figure 4.11 shows a scatter plot with regression lines between the loaded heat amounts versus temperature increases

at the urban grids. The heating efficiency was obviously larger in winter. There are 2 possible causes: the amount of anthropogenic heat was originally larger in winter, or the effect of heat release tended to be stronger in winter when the average height of the atmospheric boundary layer is lower and when a stable stratified surface layer is often formed. Some overheated grids where the rate of temperature rise was much larger than the regression lines can be seen in Fig. 4.11. The closed circles represent grids at which the temperature rose more than 1.5 times more than the regression lines. At these grids, there were probably other atmospheric causes of the overheating.

Figure 4.9C shows the effect of the growth of building heights within the urban area. The effect was larger for grids with a larger urban area fraction, and was larger in winter than in summer. An increase of the building aspect ratio causes the surface temperature to decrease in the daytime by redistributing downward shortwave radiation to the increased surface area. Conversely, it also causes the surface temperature to increase at night by inhibiting radiative cooling in the lower layers of the building canopies. These effects behave as if the effective thermal inertia of the whole surface system becomes larger. Figure 4.12 shows the daily variation of the radiative surface temperature differentials between EXP2006HR and EXP2006H for the Tokyo grid. For this grid, the aspect ratio H/B was assumed to change from 0.25 to 0.88. The surface temperature decreased in the daytime and increased at night as affected by the aspect ratio change. By considering the daily average, the surface temperature change was positive because the warming effect by inhibition of radiative cooling during the night was larger than the cooling effect by redistribution of downward shortwave radiation during the day. The longer nights in winter seemed to increase the surface temperature.

4.3.3 Nonlinear responses of the atmosphere

Since the atmosphere is a nonlinear system, quantitative comparisons of these warming effects should be made carefully. Figure 4.13 shows scatter plots between the differentials (EXP2006HR

- EXP2006H) and (EXP2006R - EXP2006) of all the land grids. These 2 differentials should represent the warming effects of the building aspect ratio changes. The closed circles represent the grids for which anthropogenic heat was added in the heat load experiments (represented by HR and H), and the open circles represent the grids with no heat load in any experiment. Naturally, the points of the no heat load grids are aligned almost along the one-to-one relation line. On the other hand, the temperature rise related to the aspect ratio change was smaller at the grids with anthropogenic heat. This can be explained by the larger vertical mixing processes. If anthropogenic heat is released into the lower part of the atmosphere, the atmosphere will become more unstable stratification condition and the vertical mixing will be slightly larger. Under such a situation, additional heat fluxes caused by other factors, such as the aspect ratio changes, probably tend to easily transfer to the upper atmosphere. With this understanding, we call the warming effects of modifications to the bottom boundary conditions on the surface air temperature derived at the previous section a kind of "warming potential."

4.4 Discussion

We examined warming tendencies caused by land use modifications over a recent 30-year period. Larger warming differentials were seen for inland grids having large land use changes and strong urban growth, with less warming along the coastlines. These warming tendencies were qualitatively in good agreement with the observed warming trends. The features of the daily variation, such as larger warming during the night and smaller warming during the day, were also in good agreement with observations. The correlation factors, however, showed only weak concordance between the simulation and the observation.

First, the discrepancy between the analytical methods used in the simulation and for the observations should be recognized. The warming results from the simulation were simple differences between sensitivity experiments that used the same initial and lateral boundary atmospheric conditions. On the other hand, the warming trends derived from the observations were calculated

using regression analysis. As discussed in the sections on sensitivity analysis and the nonlinear response of the atmosphere, atmospheric stability affects the vertical mixing of heat fluxes. Therefore, there might be easily warmed years and insensitive years. We should keep in mind that the observational trends involve such large-scale interannual variations.

Furthermore, there is probably some room to discuss the applicability of the base settings listed in Table 4.3 for representing each type of land use in 1976, although the parameters are well optimized and are used presently for operational predictions at the JMA. Although we tried to use datasets of anthropogenic heat and building shapes as real as possible for the 2006 simulations, the settings of those for 1976 are a matter of speculation.

For more precise reproduction, we had to downscale using various reanalysis datasets, for example, of JRA-25 (Onogi et al. 2007), as initial and lateral boundary conditions and had to perform numerical integrations over several decades. As no release of anthropogenic heat was assumed in the 1976 study, the effects of anthropogenic heat were probably overestimated. The considerable overestimation for Tokyo seemed to be caused by overestimation of the anthropogenic heat effect. This can be explained by the larger discrepancy in the winter case. We assumed that there was no anthropogenic heat in 1976, but there already could have been a certain amount of heat loaded in a megacity such as Tokyo. On the other hand, the overestimation at Takada in the summer case seemed to be caused by the land use effect. This can be explained by the fact that discrepancy from the observed trend was only observed in the summer case. Actually, the Takada meteorological observatory has larger premises than other typical observatories, with many trees along with a nearby stream, although it is surrounded by urban land. Such a local environment could be a cause of the large difference between the simulation and the observation. This could be a possible limitation of this study.

The area fraction changes of the land use categories over the 30-year period showed a positive impact on the surface air temperature. The warming effect seemed to be mainly caused by the decrease of vegetation. This could be explained by the well-known Bowen ratio effect. The simulations confirmed that the Bowen ratio effect is larger in a moist and sunny summer than

in a dry winter with weak sunshine. From this analogy, this kind of warming effect should be larger in western Japan, where it is humid, than in drier northern Japan. Furthermore, from the aspect of urban planning, the importance of keeping large green spaces is implied if we think that Japan will gain more features of a humid subtropical climate as global warming progresses in the future.

The impact of the anthropogenic heat was larger in winter than in summer. The sensitivity of the atmosphere to the input heat load was larger in winter (Fig. 4.11). This can be explained by the inhibition of vertical mixing in the relatively stable atmosphere of winter seasons. However, in the winter case (Fig. 4.10), the effect of the anthropogenic heat load peaked in the evening and the warming range slightly decreased up through dawn even though the atmosphere must have become more stable during these hours. The decrease of the heat amount during the night by itself likely produced the evening peak. The largest peak in the morning can be explained by the combination of stable atmospheric conditions and the large heat amounts in that time range.

A proportional relation between the heat release and the warming effect can be seen in Fig. 4.11. There are a number of points, however, that obviously deviate from the average proportion. The grey squares in Fig. 4.14 show the grids of these overheated points (indicated by closed circles in Fig. 4.11). It can be seen that they appear in areas surrounding the centers of heat loads. The vectors in the figure show the direction of the average surface wind. The contour lines represent the advection terms of the potential temperature at the lowest atmospheric level, calculated from hourly data and averaged throughout the seasons. Overall, the urban area had negative heat advection. The overheated areas, however, correspond to the less-negative advection areas in both summer and winter. Considering the average wind field, the advection of relatively warm air from the upwind urban area can be one cause of overheating in summer. In winter, the locally larger heat loads in the midwest part of Tokyo, where some bedroom suburbs lie along trunk railways, form the less-negative advection areas around them, although there exist less densely urbanized grids in the upwind area of the overheated grids under the northerly prevailing wind.

We arrived at the possibility that the temperature rise was caused by the increase in the build-

ing aspect ratio from the simulations. The main factor appears to be the temperature rise of the urban surfaces. The effect of the surface warming during the night was larger than the effect of surface cooling during the daytime. The total effect was larger in winter, when nights are relatively longer, than in summer. From this hypothesis, the effect of the aspect ratio changes should be larger in northern Japan because the nighttime is relatively longer there than in other areas. The effect should also be larger in inland basins where radiative cooling occurs effectively.

4.5 Summary

By numerical simulations using the JMA-NHM, we studied how much 3 bottom boundary condition changes, namely, in land use area fraction, anthropogenic heat release, and increased building aspect ratio, could explain the warming trends observed at the AMeDAS stations during a 30-year period (1976 - 2006). Unlike previous sensitivity studies in which the simulations were executed under idealized or other typical atmospheric conditions, we tried to determine the warming effects of the land surface modifications on the average surface air temperature under many weather conditions through longer-time simulations.

From the differentials between simulations with 2 bottom boundary conditions emulating the land surfaces of 1976 and 2006, the possible sources of warming along with the urbanization were determined. The correlation coefficients between the simulated differentials and the observational trends at the grids of the AMeDAS stations showed a lower correlation (0.294 with a significance level of 90%) in the summer case and fairly good correlation (0.444 with a significance level of 99%) in winter.

A sensitivity study of land use modification, i.e., the spread of urban area, showed a warming effect on average, and that the effect was larger in grids where the land use modification rate was larger. The effects were very small in central Tokyo because the urban area fraction was already saturated there by 1976. This effect was larger in summer when the Bowen ratio is originally small.

The warming effect of anthropogenic heat was concentrated to the central urban area where the heat was mainly loaded. The effect was larger in winter owing to relatively stable atmospheric conditions. Maximum warming was observed in the morning and a secondary peak was seen in the evening if we set the heat to vary realistically with time.

The increase of the aspect ratio of the buildings also had a warming effect on the surface air temperature. It was mainly caused by the inhibition of radiative cooling during nighttime, and the effect was larger in winter. The daily variation of this effect had a single peak in the morning.

Secondarily, the simulations in this study showed that there would be large discrepancies in the results depending on the settings of the bottom boundary conditions, although the dependency did not seem to affect the whole atmosphere system so much. The results of this study illustrate the importance of more precise land surface settings when we assess the environment of the surface layer, which is the most important layer for human activities.

Table 4.1: AMeDAS stations in the study area (the Kanto-Koshin region). The trends and their significances derived from 31 years (1976-2006) of observational data are also listed.

		Trend [°C/30 years]		Significance[%]	
Station ID	Station Name	summer	winter	summer	winter
36476	KOORIYAMA	1.69	1.52	95	98
36667	SHIRAKAWA	1.16	1.31	87	95
40201	MITO	1.28	1.3	89	96
41141	OTAWARA	1.12	1.33	88	96
41166	OKUNIKKO	1.26	1.01	96	82
41277	UTSUNOMIYA	1.64	2.05	96	99
42251	MAEBASHI	1.67	1.36	95	96
42266	KIRYU	0.92	1.14	76	93
43056	KUMAGAYA	1.86	1.67	97	99
43156	CHICHIBU	1.43	1.55	94	98
44131	TOKYO	1.53	1.48	94	98
45147	CHOSHI	0.81	0.97	77	85
45212	CHIBA	1.74	1.75	97	99
45371	KATSUURA	0.71	1.22	79	94
45401	TATEYAMA	1.05	0.82	92	84
46106	YOKOHAMA	1.43	1.44	95	98
48156	NAGANO	1.06	1.14	89	87
48256	UEDA	0.5	0.62	54	61
48331	KARUIZAWA	1.59	1.37	98	92
48361	MATSUMOTO	1.46	0.94	97	78
48491	SUWA	1.55	1.33	99	87
48606	KISOFUKUSHIMA	1.59	1.09	99	82
48767	IIDA	1.65	0.92	99	80
49142	KOFU	1.72	1.65	99	99
49251	KAWAGUCHIKO	1.67	1.37	99	94
50206	MISHIMA	1.49	1.4	98	97
50281	AJIRO	1.06	1.02	88	91
50331	SHIZUOKA	1.03	1.16	91	94
50456	HAMAMATSU	1.28	1.31	96	94
50551	OMAEZAKI	0.67	1.45	74	96
50561	IROZAKI	0.68	0.9	75	86
54651	TAKADA	1.09	1.25	89	94

Table 4.2: Principal specifications of the JMA-NHM.

Governing equations	Fully compressible non-hydrostatic equations
Horizontal discretization	Grid point method
Treatment of advection term	Fourth-order flux form (advection corrected)
Map projection	Lambert conformal projection
Vertical grid series	Hybrid z*-coordinate of Ishida (2008)
Topography	GTOPO30
Sea-Land distributions	National Land Numerical Information
Cloud microphysics	Bulk scheme with ice phase (predict qv, qc, qr, qi, qs, qg)
Cumulus parameterization	Kain-Fritsch & Cloud microphysics
Turbulent closure	Improved Mellor-Yamada Level 3
Cloud radiation	Kitagawa (2000)
Clear sky radiation	Yabu et al. (2005)
Clouds in radiation processes	Partial condensation scheme (Hara 2008)
Solid water content	Force restore method
Surface parameters	Proportional distribution by land use area
Surface scheme	Beljaars and Holtslag (1991) + Urban canopy scheme (urban grids only)

Table 4.3: Parameter list for each land use type used in the land surface schemes of the JMA-NHM.

Type	Wetness *	Albedo	Volumetric heat capacity [J K^{-1} m^{-3}]	Thermal diffusivity [m^2 s^{-1}]	Roughness *
paddy	0.8 / 0.3	0.18	1.7×10^6	0.7×10^{-6}	0.3 / 0.2
paddy	0.8 / 0.3	0.18	1.7×10^6	0.7×10^{-6}	0.3 / 0.2
farm	0.4 / 0.3	0.2	1.7×10^6	0.5×10^{-6}	0.3 / 0.2
forest	0.35 / 0.3	0.2	1.7×10^6	0.5×10^{-6}	3.0 / 3.0
wasted	0.1 / 0.1	0.25	1.6×10^6	1.4×10^{-6}	0.1 / 0.1
building	0.02 / 0.02	0.2	2.0×10^6	1.5×10^{-6}	3.0 / 3.0
road	0.03 / 0.03	0.25	2.0×10^6	2.0×10^{-6}	1.0 / 1.0
other	0.1 / 0.1	0.25	2.0×10^6	1.0×10^{-6}	0.5 / 0.5
river & lake	0.65 / 0.65	0.1	4.2×10^6	0.8×10^{-6}	0.05 / 0.05
coast	0.5 / 0.5	0.15	2.9×10^6	0.74×10^{-6}	0.1 / 0.1
sea	1.0 / 1.0	0.1	1.9×10^6	1.3×10^{-6}	0.001 / 0.001
golf	0.35 / 0.25	0.15	1.8×10^6	0.5×10^{-6}	0.4 / 0.1

*(summer / winter)

Table 4.4: Parameters for the office building materials used in the urban canopy scheme as quoted from ECCJ (2005) .

	Material	Thickness [m]	Volumetric heat capacity [J m^{-3} K^{-1}]	Thermal conductivity [W m^{-1} K^{-1}]
Roof	Lightweight concrete	0.06	1.607×10^6	0.779
	Polystyrene board	0.025	3.516×10^4	0.037
	Asphalt	0.01	9.209×10^5	0.11
	Ordinary concrete	0.15	1.934×10^6	1.395
	Air space	0.01	1.19×10^3 *1	0.0241 *2
	Plasterboard	0.009	1.633×10^6	0.791
	Asbestos acoustic board	0.012	2.512×10^5	0.064
Wall	Tile	0.008	2.009×10^6	1.279
	Mortar	0.02	1.591×10^6	1.512
	Ordinary concrete	0.15	1.934×10^6	1.395
	Air space	0.01	1.19×10^3 *1	0.0241 *2
	Plasterboard	0.012	1.633×10^6	0.791

*1 estimated from the density and constant pressure specific heat of air at 25 °C.

*2 value for air at 0 °C.

Table 4.5: List of the experiments performed for this study. The last 3 experiments were for sensitivity studies.

EXP.NAME	Land use information	Anthropogenic heat release	Building aspect ratio Height : Width
EXP1976	1976	Not Considered	1 : 4
EXP2006HR	2006	Considered	3 : 4 *
EXP2006	2006	Not Considered	1 : 4
EXP2006H	2006	Considered	1 : 4
EXP2006R	2006	Not Considered	3 : 4 *

* Aspect ratios in the Tokyo Metropolis were determined from the GIS dataset.

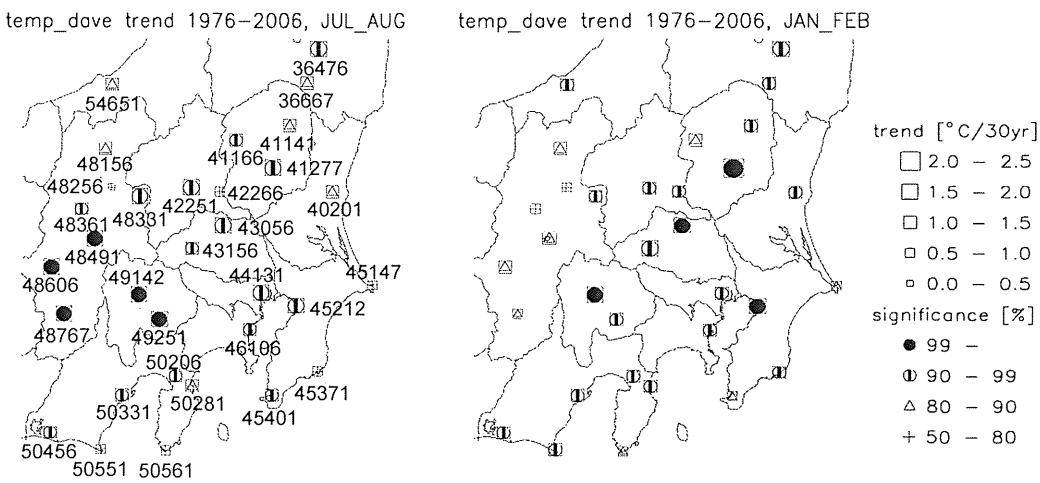

Figure 4.1: Daily average temperature trends and their significances at AMeDAS stations. The size of the square represents the trend. The indicated marks represent the significance levels of the trends.

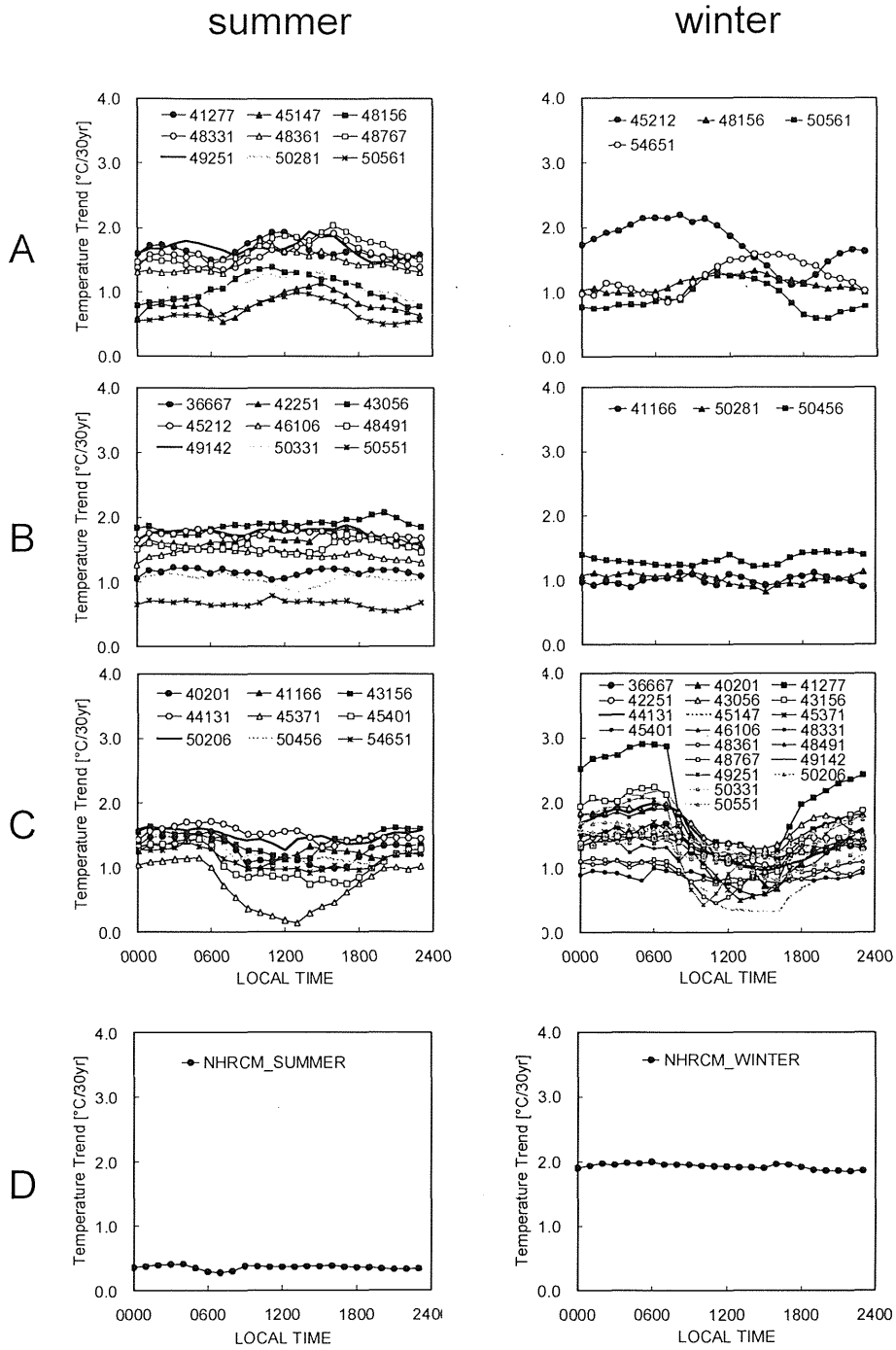

Figure 4.2: Daily variation of temperature trends. (A) Groups of observatories having trends with an upward convex shape, (B) with flat daily variation, and (C) with a downward convex shape. (D) Daily variation of the temperature trends derived from the 20 years dataset (1981-2000) of the NHRCM-20km simulation results, downscaled from JRA-25.

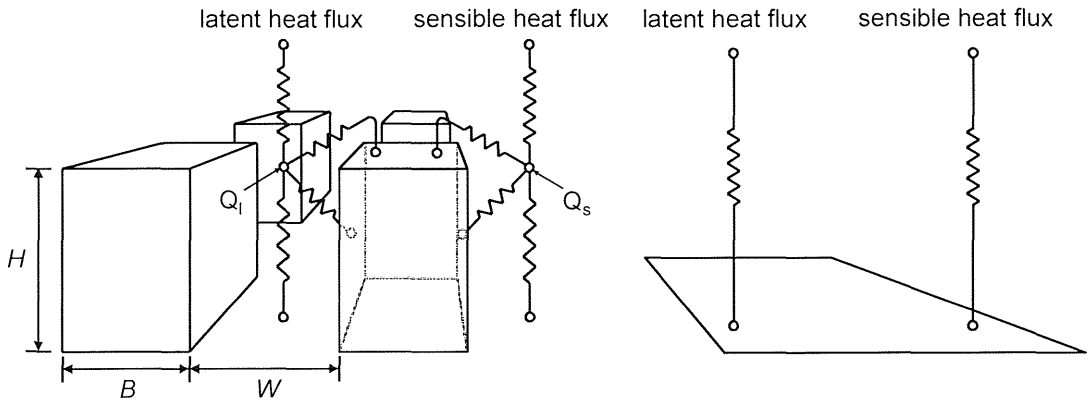

Figure 4.3: Schematic images of the flux circuits. The left image represents the urban canopy scheme used for the urban grids. The right image represents the slab surface scheme used otherwise for the non-urban grids.

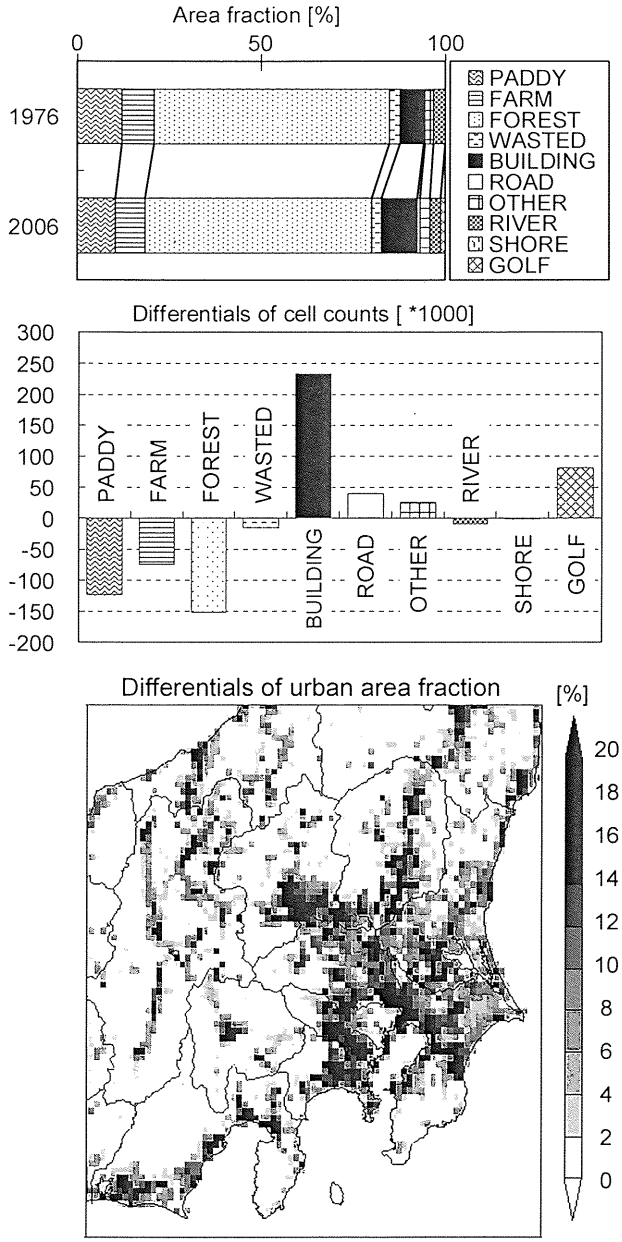

Figure 4.4: The area fraction differences between the 1976 and 2006 land use datasets (top). The increase or decrease of each land use type in the form of cell (approximately 100 m ×100 m) counts stored in the original National Land Numerical Information datasets (middle). The horizontal distribution of the increases and decreases of the urban area fraction in 4 km × 4 km grids, which were used in the numerical simulations executed in this study (bottom).

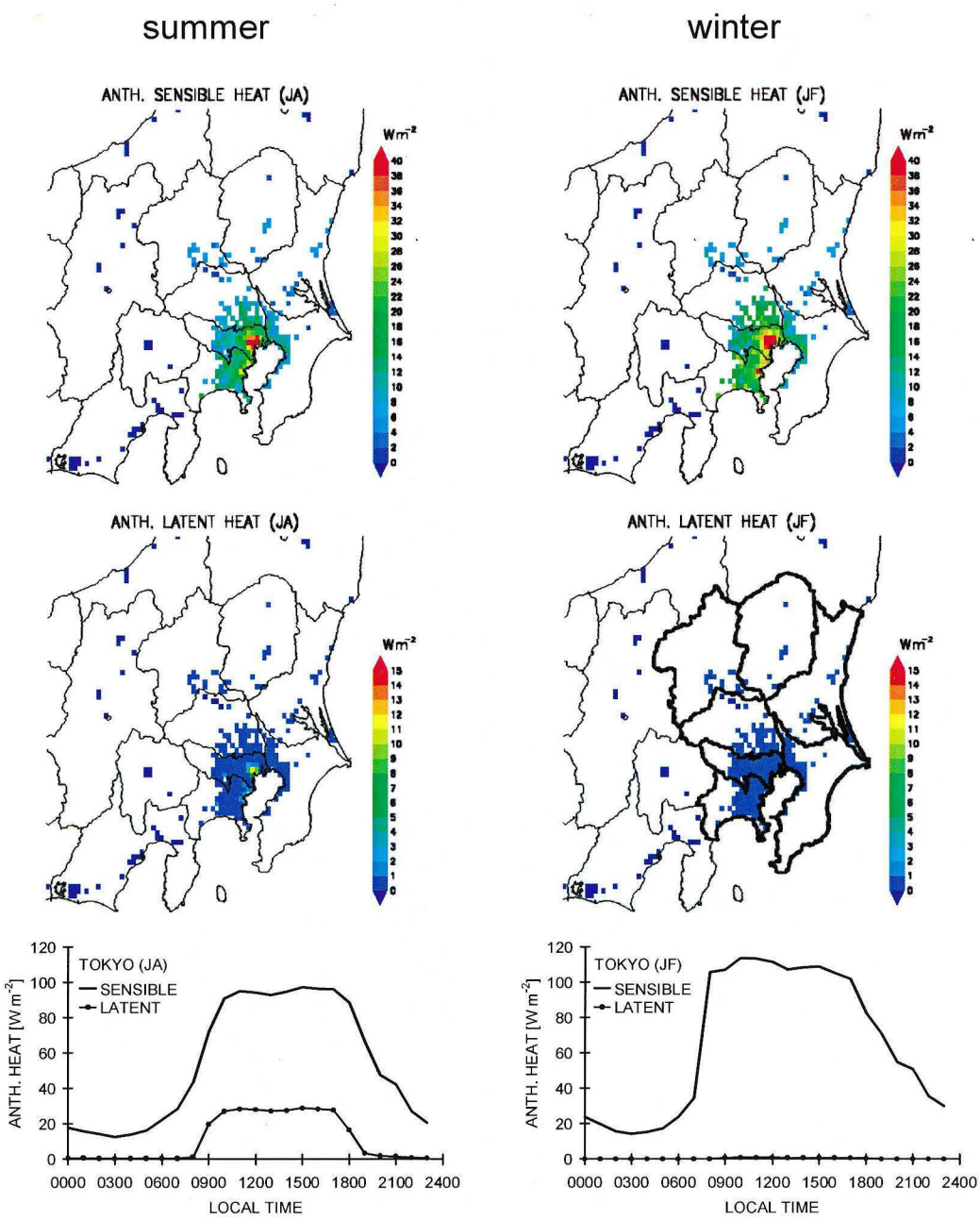

Figure 4.5: Horizontal distributions of the seasonal averaged anthropogenic heat in the form of sensible heat (top) and latent heat (middle). As an example, the bottom plots represent the time variations of anthropogenic heat added to the Tokyo grid.

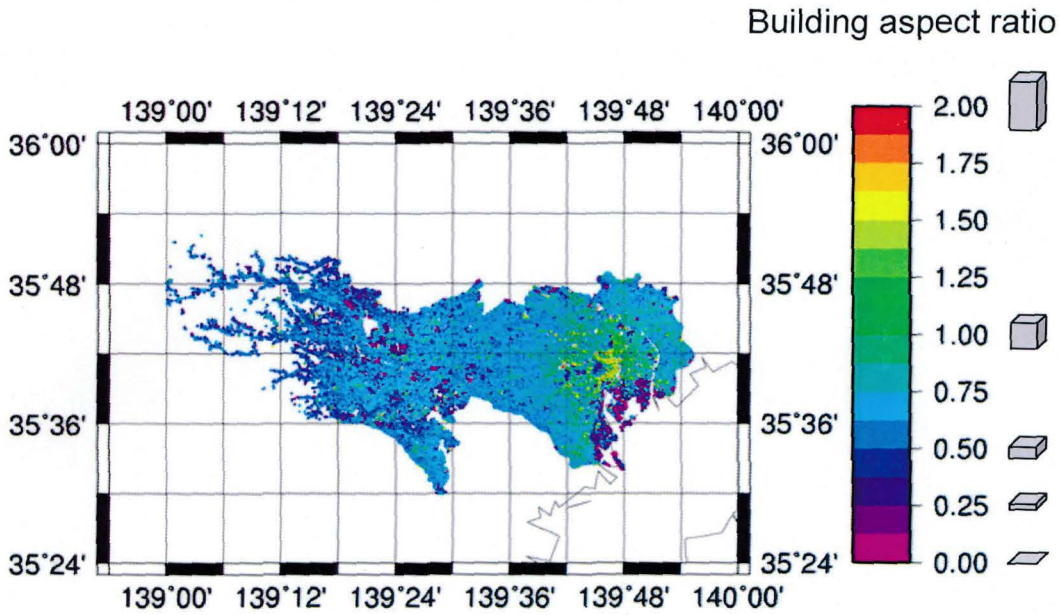

Figure 4.6: Distribution of building aspect ratios in the Tokyo Metropolis derived from the GIS dataset compiled by the Tokyo metropolitan government.

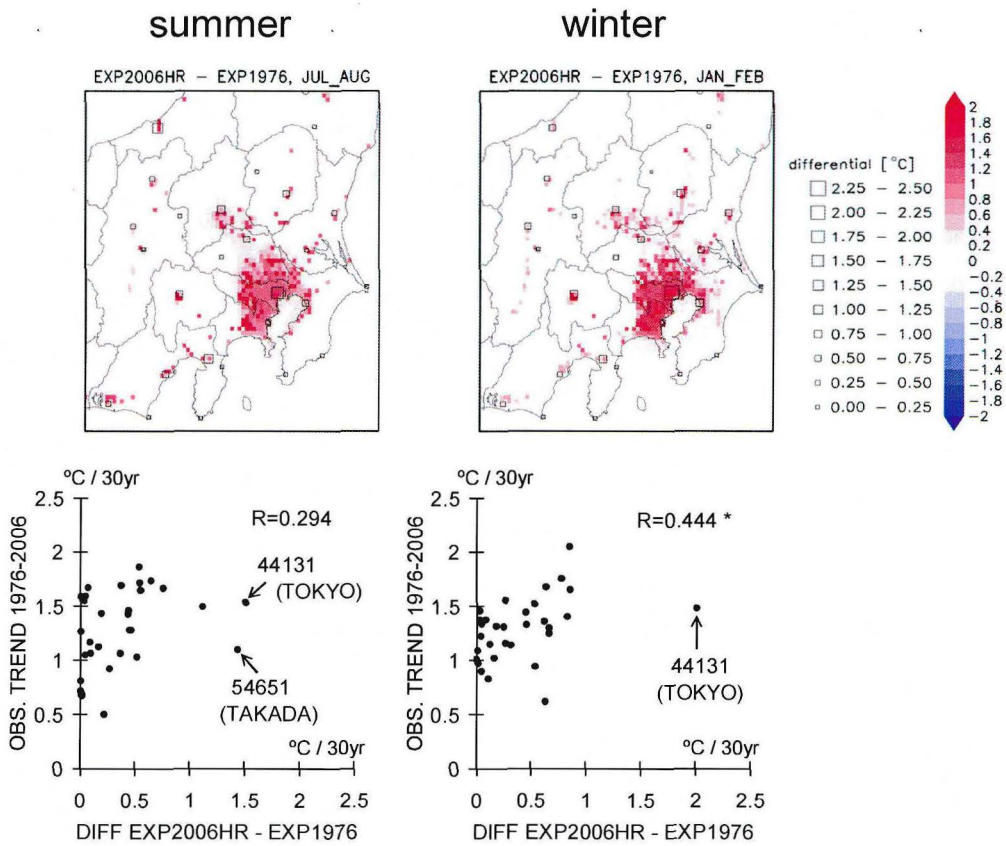

Figure 4.7: Differentials of the averaged surface air temperature between the simulations of EXP2006HR and EXP1976. The bottom scatter plots show the correlations between the observe trends and the temperature differentials at the corresponding grids of the AMeDAS stations.

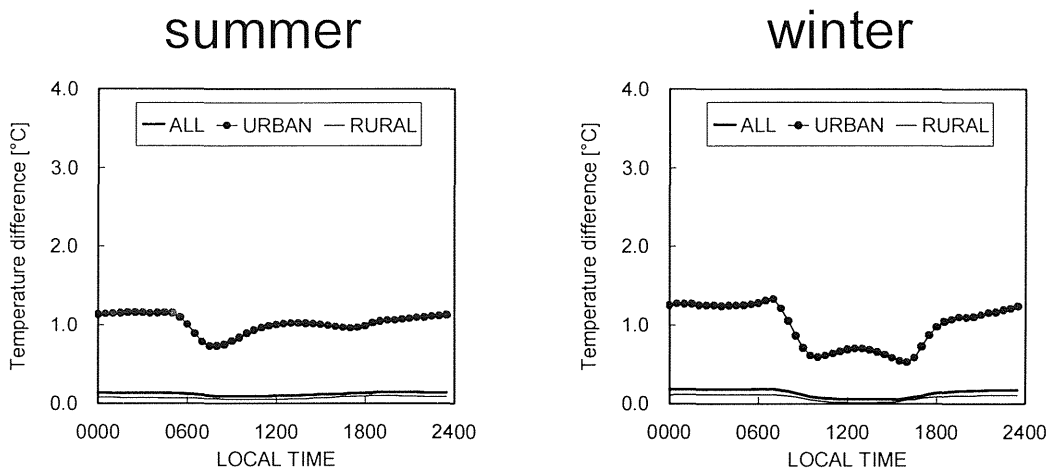

Figure 4.8: Daily variations of the temperature differential between EXP2006HR and EXP1976 for summer and winter. Dotted lines thin lines, and thick lines describe the results averaged over urban grids, rural grids, and all over the land grids, respectively.

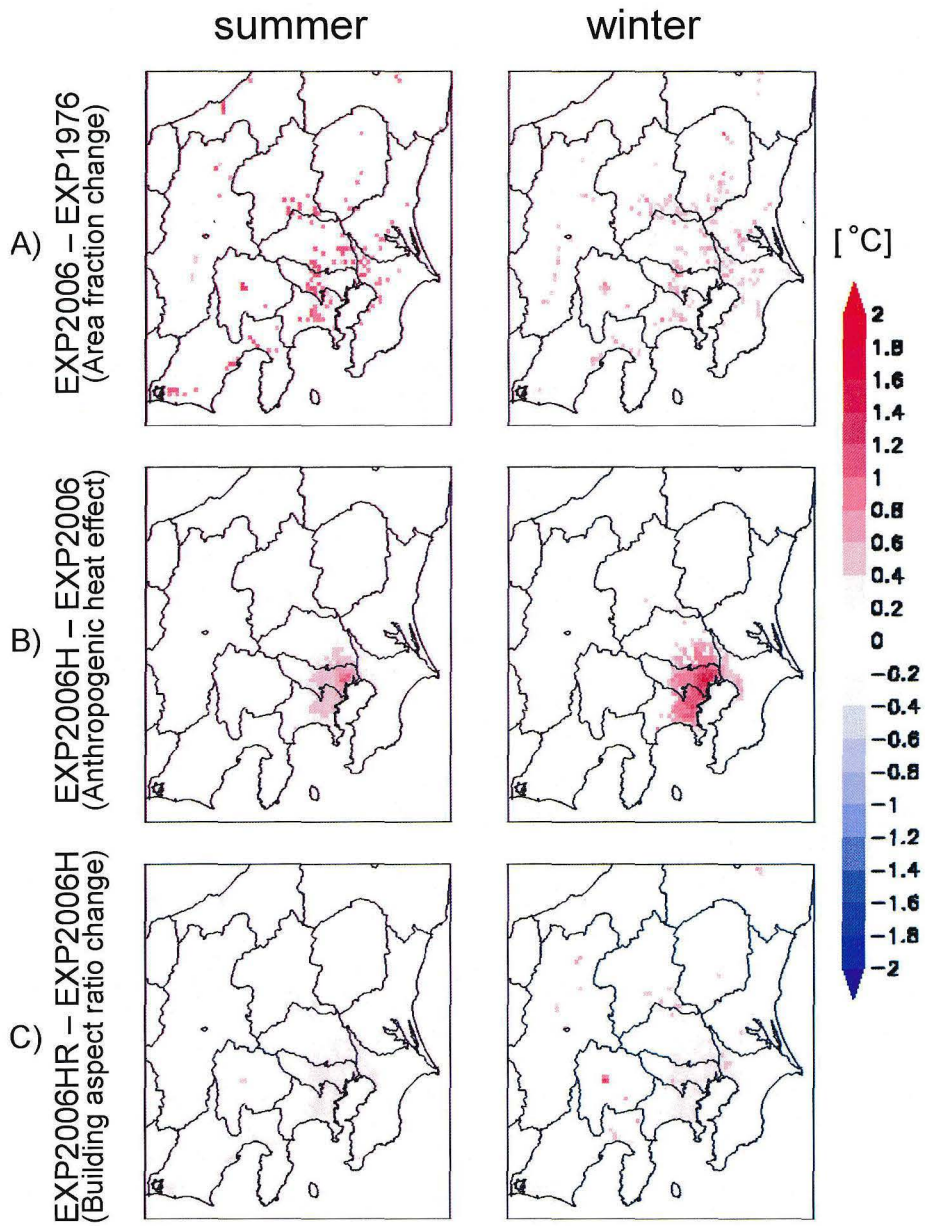

Figure 4.9: Differentials of the averaged surface air temperature between the experiments of (A) EXP2006 and EXP1976, representing the effects of the land use area fraction changes; (B) EXP2006H and EXP2006, representing the effects of the anthropogenic heat releases; and (C) EXP2006HR and EXP2006H, representing the effects of the building aspect ratio changes.

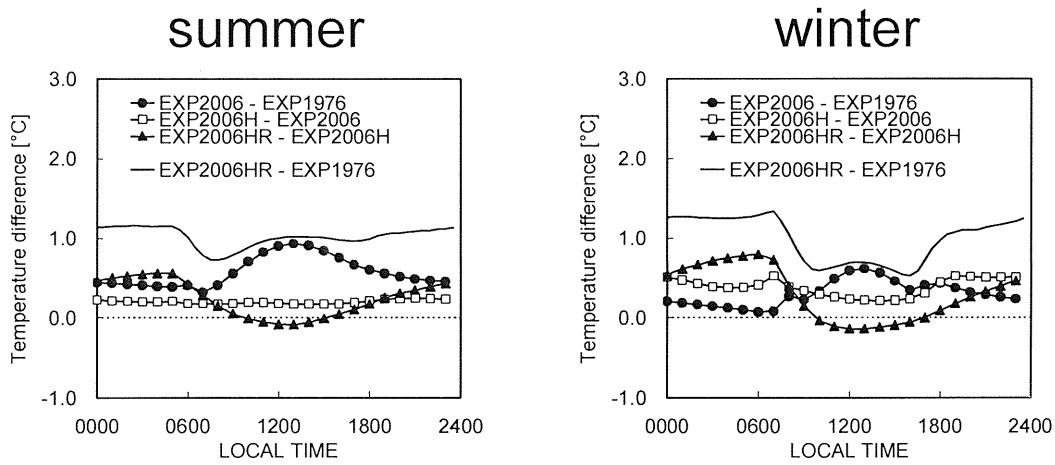

Figure 4.10: Time variations of the temperature differences averaged between the experiments. The differentials were averaged over all urban grids.

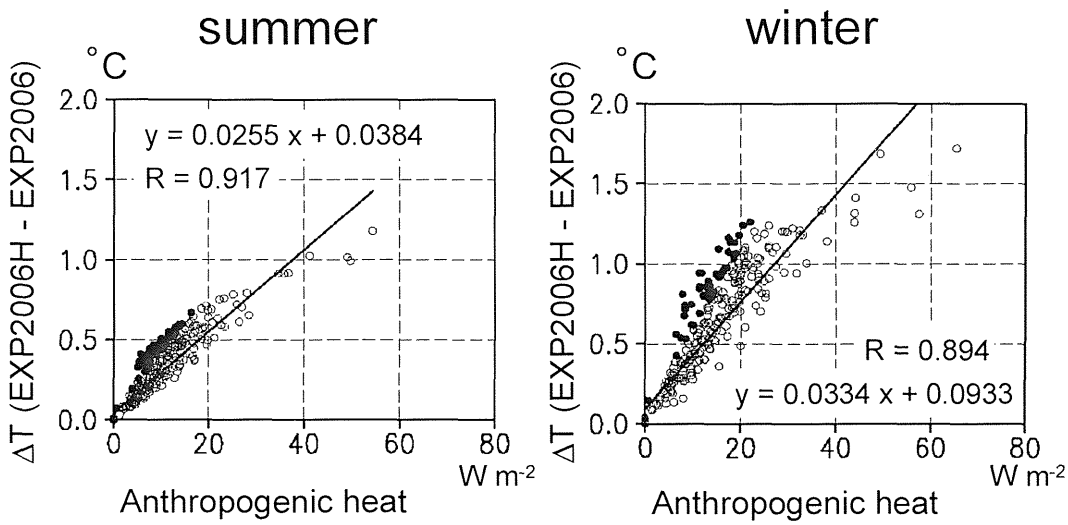

Figure 4.11: Scatter diagrams between the anthropogenic heat amounts added to the urban grids and the temperature increases at the grids. The closed circles indicate grids whose temperature rose more than 150 % more than the regression lines.

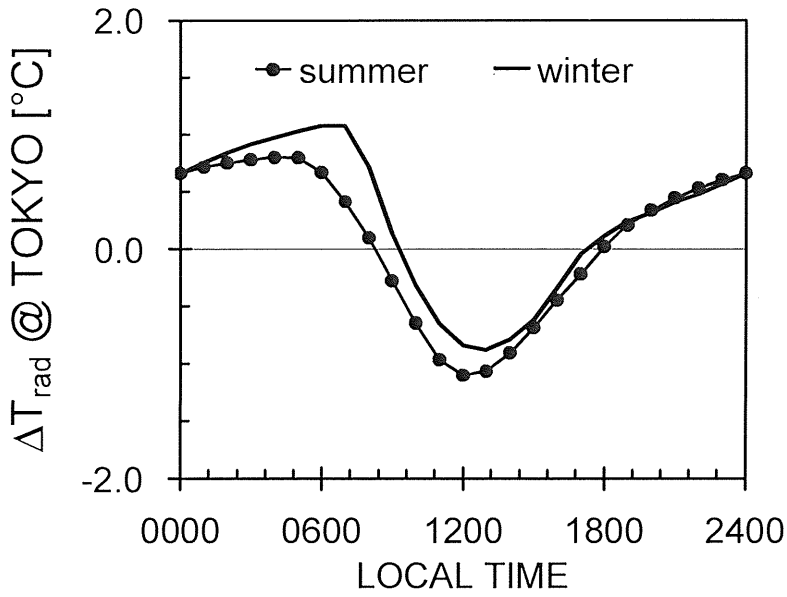

Figure 4.12: Differences in radiative surface temperature between the experiments of EXP2006HR and EXP2006H for the Tokyo grid. The radiative surface temperature was estimated from the surface temperatures of the roofs, walls, and the ground as defined in the urban canopy scheme. The dotted and solid lines represent the summer and winter cases, respectively.

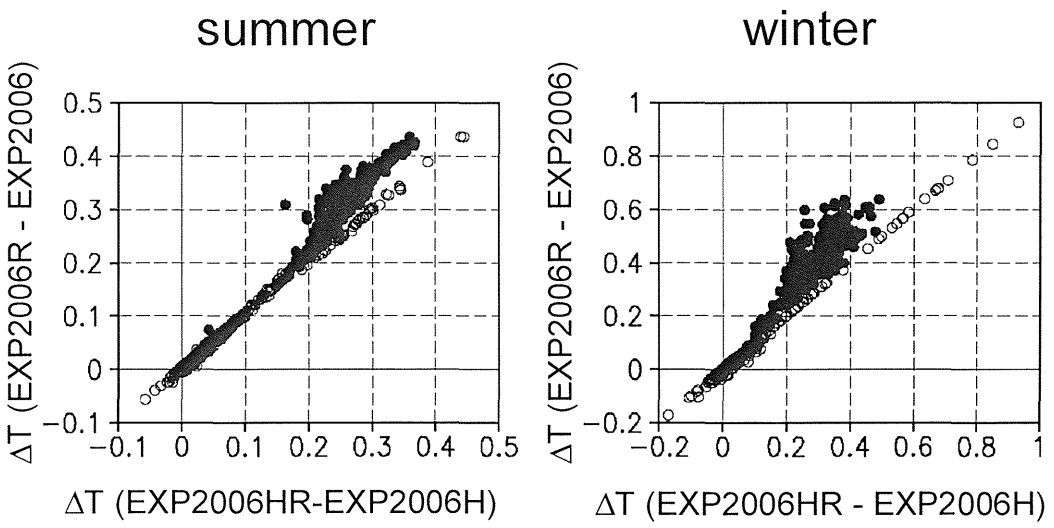

Figure 4.13: Scatter plots between the temperature differentials of (EXP2006HR - EXP2006H) and (EXP2006R - EXP2006). These differentials both represent the warming effects of the building aspect ratio changes. Open circles are the grids without any anthropogenic heat in the simulations. Closed circles are the grids onto which anthropogenic heat was loaded.

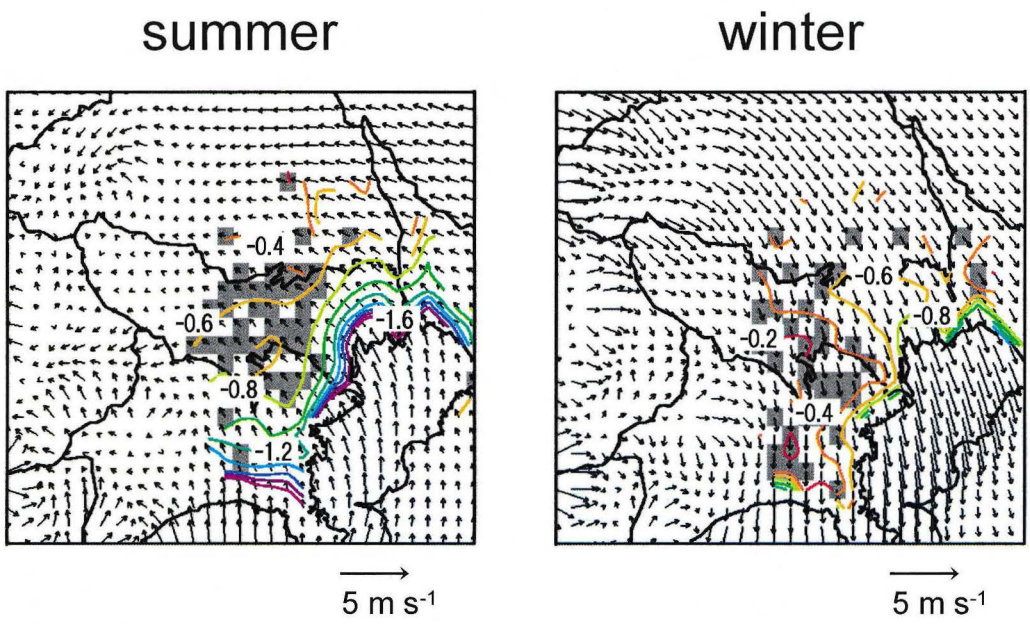

Figure 4.14: Horizontal distributions of the overheated grids (closed circles in Fig. 4.12). The vectors represent the 2 months' averaged vectors of the surface winds at 10 m. The contour lines represent the advection term of the potential temperature at the lowest atmospheric level.

Chapter 5

Conclusions

Analyses on the local climate change attributed to the land use modifications during this 30 years were employed in this study. The effect of such land use modification appears as the result of various factors such as the modifications of radiation balances, surface heat balances (including the Bowen ratio change, modifications of heat fluxes amounts and heat flux routings). Firstly, we considered the concrete blocks emulating the urban building canopies, and confirmed how much the temperatures of block surfaces will rise in the radiative equilibrium state only modified the radiative balances, that is no consideration of anthropogenic heating, no heat fluxes. Secondly, we developed an urban canopy scheme called SPUC applicable to the land surface scheme of the JMA-NHM and checked its reproducibility performance. Finally, using the JMA-NHM coupled with the SPUC urban canopy scheme, we succeeded to simulate and estimate the seasonal mean temperature rises during this 30 years based on the more realistic land use datasets, anthropogenic heating data, and the distribution of building aspect ratio data derived from real GIS polygons. Each founding can be summarized as below:

5.1 Surface Warming Induced by the Building's Morphological Change

An urban multilayer radiation scheme based on the radiosity method was developed in order to express sophisticatedly how the urban building morphology changes radiative environment inside the urban canyon. The exact estimation of net radiation, considering full multiple scatterings of both shortwave and longwave radiation, at each surface element of building wall can be done with this scheme. Assembling this urban multilayer radiation scheme, the equations determining the daily variation of solar radiation, and heat conduction equation forecasting inside temperature of each surface element, we built up a numerical model to estimate the surface temperature of supposed blocks. Simulation results using this model were compared with the earlier observational results of Aida (1982) and Kanda et al. (2005a) , which observed daily variations of effective albedo of building-like block arrays, and the simulation showed a good reproducibility. How to provide the innermost boundary condition of building element is most important for such urban energy balance models. Then the comparison with observations of two COSMO scale models (1.5m and 0.5m on a side) was also employed. The comparison showed an important suggestion that the insulated boundary condition is preferable when the blocks are hollow, and a constant value setting (e.g. mean temperature) shows good reproducibility of temporal variation for solid blocks. Eventually, it was shown that the USWP (Urban Surface Warming Potential) will be increased depending with the decreases of the sky-view factors as shown in Fig. 2.10. This USWP was confirmed as an useful index to assess pure effects of radiation balance changes not depending on the building's thermal properties. Moreover, the figure also reaffirmed the applicabilities of single layer urban radiation schemes, such as Masson (2000) and Kusaka et al. (2001) , on the radiation balance estimation in the sparse urban area over 0.5 of sky-view factor.

5.2 Development of An Urban Canopy Scheme for the JMA's Mesoscale Model

An urban canopy scheme for mesoscale atmospheric model was developed by adding the consideration of heat fluxes to the urban radiation scheme. A single layered architecture was selected because of its light calculation cost on the mesoscale simulations. The representation of precipitation interception and latent heat fluxes during and after a precipitation event can be considered by the scheme. From the comparison with observational results at Kugahara station of Moriwaki et al. (2004) on typical clear summer days of August 2005, considerable improvements on the representation of upward short- and longwave radiation could be seen. The newer representation of time-dependent effective albedo considered to contribute better representation of the upward shortwave. Representation of upward longwave radiation was also improved through the better forecasts of the surface temperature. The representations of sensible and latent heat fluxes, however, was changed for the worth. The sensible heat flux was overestimated and the overestimation seemed to bring down worth underestimation of the latent heat fluxes. The monthly mean bias of the surface air temperature was improved with the SPUC scheme than with the slab scheme under the one month reproduction experiment for August 2005. The addition of anthropogenic heat was largely contributed to dissolve the negative bias feature of the slab scheme. However, certain improvements on the representation of surface air temperature from dusk to dawn by only the SPUC scheme were seen from the comparative experiments with and without the anthropogenic heat. As stated above, the availability of SPUC scheme for the JMA-NHM was confirmed although there are some room to improve yet on how to set the appropriate parameters and heat transfer efficiencies. Densifications of land use information, addition of the buildings' morphological and material information from the higher resolution dataset such as geographical information systems (GIS) will be needed for the better reproduction of the radiation balance and the heat balance that are characteristic of urban areas.

5.3 Numerical Simulation on the Urban Warming in Kanto-Koshin Area

The final challenge of this study went to the representation of urban warming trends induced by the land use changes during this 30 years. Firstly, the temperature warming trends derived by the AMeDAS observation were shown. It was shown that the all observatories had positive warming trends and the inland observatories had larger positive trends than the coastal observatories. Some sensitivity studies using the SPUC-coupled JMA-NHM were executed in order to check how much the positive warming trends could be explained by the effect of land use modifications. As the result, a certain correlation could be seen between the differentials of seasonal mean surface air temperature derived from the simulation with two bottom boundary conditions of 2006 and 1976 cases and the long term warming trends of surface air temperature estimated from the AMeDAS observation datasets from 1976 to 2006. The warming effect of the land use changes, that is the Bowen ratio changes induced by the surface modifications from the vegetation to the urban surfaces, was larger in summer than winter season and larger at the surroundings of urban center. Warming with the anthropogenic heat formed concentric distribution centered on highly urbanized area. The warming effect had daily variation of double peaked shape at early morning and evening times. The effect of radiation balance changes induced by the verticalization of urban buildings could be expressed by the SPUC scheme. The warming by the buildings' verticalization was larger at the urban center and larger during nighttime. As that is because the larger inhibition effect of radiative cooling at night, the warming effect was clearer in winter season when the stable stratification is easily formed and the radiation balance tends to be more important than the turbulent heat fluxes.

This study figured out the important fact that the effect of land use modification on the surface air temperature warming is too large to ignore even in the shorter period of 30 years. This study also showed that the simulation models with an urban parameterization scheme is usable for the

environmental assessment on land use modification when we use the detailed and proper datasets of land use change history, anthropogenic heat distribution, and the buildings' morphological information.

The previous researches, such as Kimura and Takahashi (1991) and Ichinose et all. (1999) , had already figured out qualitative effects of land use change and anthropogenic heat on surface air temperature using simulation technique. Their simulations, however, were limited to some typical or idealized atmospheric conditions. Therefore, their results could not be compared simply to the warming trends derived from the long-term observations which must contain many weather conditions. On this point, this study was very new on that the relatively long term (seasonal) simulations with the real land surface datasets of recent years and 30 years ago was compared with the observed datasets during the same period and the comparison showed a certain correlation between the simulated urban warming and the temperature rising trends observed. This study states the substantial importance of bottom boundary settings of atmospheric models on the reproduction experiments of current climates and on the forecasting studies of future climate change. For the reproduction of current climate, the more realistic land surface settings enables us to reproduce the warming trends found in the observational data, this study suggested. Especially, it is an important finding that the climatic warming can be occurred only by the changes of internal structure of urban area, such as the Manhattanization of buildings. Based on the findings of this study, the future land use scenario should be considered to be essential for the future climate simulations, especially for the finner scale regional climate simulations. These new findings of this study shall contribute to the future urban climate study.

Acknowledgements

The author would like to express his gratitude to Prof. Hiroshi L. Tanaka of the Center for Computational Sciences, the University of Tsukuba for invaluable advices and supports while compiling this dissertation. Special thanks are extended to Dr. Masao Mikami of the Meteorological Research Institute, who opened author's way to get PhD degree.

The author also thanks to Dr. Naoko Seino of the Meteorological Research Institute and Shunji Takahashi, the director of Nagano Local Meteorological Observatory. The researches in this dissertation could not completed without their helpful suggestions and kind supports. Many valuable discussions with Prof. Hiroyuki Kusaka of the University of Tsukuba and Dr. Fumiaki Fujibe of the Meteorological Research Institute, and many fruitful comments on this dissertation from Prof. Yasutaka Wakazuki of the University of Tsukuba are greatly appreciated, too.

The author acknowledges Dr. Izuru Takayabu and Dr. Shinji Nakagawa of former heads of the author's research laboratory for their encouragements; Masaru Chiba, Masahiro Hosaka of the Meteorological Research Institute, Prof. Mitsuo Ohizumi of the Meteorological College and Masashi Ujiie, Nobuyuki Kayaba, Takashi Yamada, Tabito Hara, Hiroshi Kusabiraki, and Hiroshi Hasegawa of the Japan Meteorological Agency for helpful discussions; Dr. Hiroyuki Naoe of the Japan Meteorological Agency for many kind supports on scientific writing; Dr. Tsuyoshi Kinouchi of Tokyo Institute of Technology for providing anthropogenic heat release dataset.

The author's acknowledgements are extended to all members of the Atmospheric Environment and Applied Meteorology Department, the Meteorological Research Institute for giving excellent research environment.

Finally, the author would like to express his heartfelt gratitude to his wife and children for their encouraging supports.

References

Adachi, S. and F. Kimura, 2010: A factor analysis on the nighttime warming trends in the Kanto area of Japan. *J. Jpn. Study Group Clim. Impact Appl.*, **28**, 5–13, (in Japanese).

Aida, M., 1982: Urban albedo as a function of the urban structure - a model experiment. *Bound.-Layer Meteor.*, **23**, 405–413.

Aida, M. and K. Gotoh, 1982: Urban albedo as a function of the urban structure - a two-dimensional numerical simulation. *Bound.-Layer Meteor.*, **23**, 415–424.

Aoyagi, T. and N. Seino, 2011: A square prism urban canopy scheme for the NHM and its evaluation on summer conditions in the Tokyo Metropolitan area, Japan. *J. Appl. Meteor. Climatol.*, **50**, 1476–1496.

Arnfield, A., 2003: Two decades of urban climate research: a review of turbulence, exchanges of energy and water, and the urban heat island. *Int. J. Climatol.*, **23**, 1–26.

Beljaars, A. and A. Holtslag, 1991: Flux parameterization over land surface for atmospheric models. *J. Appl. Meteor.*, **30**, 327–341.

Best, M., 2005: Representing urban areas within operational numerical weather prediction models. *Bound.-Layer Meteor.*, **114**, 91–109.

Brown, M. and M. Williams, 1998: An urban canopy parameterization for mesoscale meteorological models. *Preprints, Second Symp. on the Urban Environment*, Albuquerque, NM, American Meteorological Society, 144–147.

Chen, F., et al., 2010: The integrated WRF/urban modeling system: development, evaluation, and applications to urban environmental problems. *Int. J. Climatol.*, DOI 10.1002/joc.2158.

Cullen, M., 1993: The Unified Forecast / Climate Model. *Meteor. Mag.*, **122**, 81– 94.

Deardorff, J., 1978: Efficient prediction of ground surface temperature and moisture, with inclusion of a layer of vegetation. *J. Geophys. Res.*, **83**, 1889–1903.

Dupont, S. and P. Mestayer, 2006: Parameterization of the urban energy budget with the submesoscale soil model. *J. Appl. Meteor. Climatol.*, **45**, 1744–1765.

Dupont, S., T. Otte, and J. Ching, 2004: Simulation of meteorological fields within and above urban and rural canopies with a mesoscale model (MM5). *Bound.-Layer Meteor.*, **113**, 111–158.

ECCJ, 2005: *Report of survey on the effect of energy conservations to mitigation of heat island phenomena.* the Energy Conservation Center, Japan, 266 pp., (in Japanese).

Fernando, H., D. Zajic, D. Di Sabatino, R. Dimitrova, and B. Hedquist, 2010: Flow, turbulence, and pollutant dispersion in urban atmosphere. *Phys. Fluids*, **22**, 051 301.

Fortuniak, K., 2008: Numerical estimation of the effective albedo of an urban canyon. *Theor. Appl. Climatol.*, **91**, 245–258.

Fujibe, F., 1994: Long-term falling trends of pressure over the Kanto plain as evidence of increasing heat content in the lower atmosphere in the daytime of the warm season. *J. Meteor. Soc. Japan*, **72**, 785–792.

Fujibe, F., 2003: Long-term surface wind changes in the Tokyo metropolitan area in the afternoon of sunny days in the warm season. *J. Meteor. Soc. Japan*, **81**, 141–149.

Fujibe, F., 2009: Detection of urban warming in recent temperature trends in Japan. *Int. J. Climatol.*, **29**, 1811–1822.

Fujibe, F., 2010: Urban warming in Japanese cities and its relation to climate change monitoring. *Int. J. Climatol.*, **31**, 162–173.

Fujibe, F., N. Yamazaki, M. Katsuyama, and K. Kobayashi, 2005: The increasing trend of intense precipitation in Japan based on four-hourly data for a hundred years. *SOLA*, **1**, 41–44, doi10.2151/sola.2005–012.

Grimmond, C., et al., 2010: The international urban energy balance models comparison project first results from Phase 1. *J. Appl. Meteor. Climatol.*, **49**, 1268–1292.

Hamdi, R. and G. Schayes, 2007: Validation of Martilli's urban boundary layer scheme with measurements from two mid-latitude European cities. *Atmos. Chem. Phys.*, 7, 4513–4526.

Hamdi, R. and G. Schayes, 2008: Sensitivity study of the urban heat island intensity to urban characteristics. *Int. J. Climatol.*, **28**, 937–982.

Hara, M., H. Kusaka, F. Kimura, and Y. Wakazuki, 2010: Effect of global climate change on urban heat island intensity of Tokyo metropolitan area - winter season case -. *Nagare*, **29**, 353–361, (in Japanese with English abstract).

Hara, T., 2008: Radiation Processes. *Separate volume of annual report of NPD*, Japan Meteorological Agency, Vol. 54, 133–137, (in Japanese).

Harman, I., M. Best, and S. Belcher, 2004: Radiative exchange in an urban street canyon. *Bound.-Layer Meteor.*, **110**, 301–316.

Holt, T. and J. Pullen, 2006: Urban canopy modeling of the New York City metropolitan area a comparison and validation of single- and multilayer parameterizations. *Mon. Wea. Rev.*, **135**, 1906–1930.

Ichinose, T., K. Shimodozono, and K. Hanaki, 1999: Impact of anthropogenic heat on urban climate in Tokyo. *Atmos. Environ.*, **33**, 3897–3909.

Ikeda, R. and H. Kusaka, 2010: Proposing the simplification of the multi-layer urban canopy model: inter-comparison study of four models. *J. Appl. Meteor. Climatol.*, **49**, 902–919.

Inoue, T. and F. Kimura, 2004: Urban effects on low-level clouds around the Tokyo metropolitan area on clear summer days. *Geophys. Res. Lett.*, **31**, L05 103, doi10.1029/2003GL018 908.

Inoue, T. and F. Kimura, 2007: Numerical experiments on fair-weather clouds forming over the urban area in northern Tokyo. *SOLA*, **3**, 125–128.

IPCC, 2007: *Climate change 2007: the physical science basis. In Contribution of Working Group I to the Fourth Assessment Report of the IPCC.* Solomon S., Qin D., Manning M., Chen Z., Marquis M., Averyt K., Tignor M., Miller H.L. ed., Cambridge University Press, New York, 1056 pp.

Ishida, J., 2008: The governing equations of the JMA-NHM and the implementation of the hybrid terrain following vertical coordinates. *Separate volume of annual report of NPD*, Japan Meteorological Agency, Vol. 54, 27–43, (in Japanese).

Ishizaki, N. and I. Takayabu, 2009: On the warming events over Toyama Plain by using NHRCM. *SOLA*, **5**, 129–132.

Johnson, G., T. Oke, T. Lyons, D. Steyn, I. Watson, and J. Voogt, 1991: Simulation of surface urban heat islands under 'ideal' conditions at night part 1: theory and tests against field data. *Bound.-Layer Meteor.*, **56**, 275–294.

Kanae, S., T. Oki, and A. Kashida, 2004: Changes in Hourly Heavy Precipitation at Tokyo from 1890 to 1999. *J. Meteor. Soc. Japan*, **82**, 241–247.

Kanda, M., 2007: Progress in urban meteorology: a review. *J. Meteor. Soc. Japan*, **85B**, 363–383.

Kanda, M., T. Kawai, M. Kanega, R. Moriwaki, K. Narita, and A. Hagishima, 2005a: A simple energy balance model for regular building arrays. *Bound.-Layer Meteor.*, **116**, 423–443.

Kanda, M., T. Kawai, and K. Nakagawa, 2005b: A simple theoretical radiation scheme for regular building arrays. *Bound.-Layer Meteor.*, **114**, 71–90.

Kawai, T. and M. Kanda, 2003: Three dimensional radiation model for urban canopy. *Ann. J. Hydr. Eng.*, **47**, 55–60, (in Japanese).

Kawai, T. and M. Kanda, 2010: Urban energy balance obtained from the comprehensive outdoor scale model experiment Part I: Basic feaures of the surface energy balance. *J. Appl. Meteor. Climatol.*, **49**, 1341–1359.

Kawai, T., M. Kanda, K. Narita, and A. Hagishima, 2007: Validation of a numerical model for urban energy-exchange using outdoor scale-model measurements. *Int. J. Climatol.*, **27**, 1931–1942.

Kawase, H., T. Yoshikane, M. Hara, F. Kimura, T. Yasunari, B. Ailikun, H. Ueda, and T. Inoue, 2009: Intermodel variability of future changes in the Baiu rainband estimated by the pseudo global warming downscaling method. *J. Geophys. Res.*, **114**, D24 110, doi10.1029/2009JD011 803.

Kikegawa, Y., Y. Genchi, H. Yoshikado, and H. Kondo, 2003: Development of a numerical simulation system toward comprehensive assessments of urban warming countermeasures including their impacts upon the urban building's energy demands. *Appl. Energy*, **76**, 449–466.

Kimura, F. and S. Takahashi, 1991: The effects of land-use and anthropogenic heating on the surface temperature in the Tokyo metropolitan area A numerical experiment. *Atmos. Environ.*, **25B**, 155–164.

Kitagawa, H., 2000: Radiation Processes. *Separate volume of annual report of NPD*, Japan Meteorological Agency, Vol. 46, 16–31, (in Japanese).

Kobayashi, T. and T. Takamura, 1994: Upward longwave radiation from a non-black urban canopy. *Bound.-Layer Meteor.*, **69**, 201–213.

Kondo, A., M. Ueno, A. Kaga, and K. Yamaguchi, 2001: The influence of urban canopy configuration on urban albedo. *Bound.-Layer Meteor.*, **100**, 225–242.

Kondo, H., Y. Genchi, Y. Kikegawa, Y. Ohashi, H. Yoshikado, and H. Komiyama, 2005: Development of a multi-layer urban canopy model for the analysis of energy consumption in a big city structure of the urban canopy model and its basic performance. *Bound.-Layer Meteor.*, **116**, 395–421.

Kusaka, H., F. Chen, M. Tewari, M. Duda, J. Dudhia, Y. Miya, and Y. Akimoto, 2009: Performance of the WRF model as a high resolution regional climate model model inter comparison study. *Extended abstracts of the 7th Int. Conf. on Urban Climate,*, Yokohama, Int. Assoc. for Urban Climate, 3–25.

Kusaka, H. and F. Kimura, 2004a: Coupling a single-layer urban canopy model with a simple atmospheric model Impact on urban heat island simulation for an idealized case. *J. Meteor. Soc. Japan*, **82**, 67–80.

Kusaka, H. and F. Kimura, 2004b: Thermal effects of urban canyon structure on the nocturnal heat island Numerical experiment using a mesoscale model coupled with an urban canopy model. *J. Appl. Meteor.*, **43**, 1899–1910.

Kusaka, H., F. Kimura, H. Hirakuchi, and M. Mizutori, 2000: The effects of land-use alteration on the sea breeze and daytime heat island in the Tokyo metropolitan area. *J. Meteor. Soc. Japan*, **78**, 405–420.

Kusaka, H., H. Kondo, Y. Kikegawa, and F. Kimura, 2001: A simple single-layer urban canopy model for atmospheric models comparison with multi-layer and slab models. *Bound.-Layer Meteor.*, **101**, 329–358.

Lemonsu, A., C. Grimmond, and V. Masson, 2004: Modeling the surface energy balance of the core of an old Mediterranean city Marseille. *J. Appl. Meteor.*, **43**, 312–327.

Lemonsu, A. and V. Masson, 2002: Simulation of a summer urban breeze over Paris. *Bound.-Layer Meteor.*, **104**, 463–490.

Liu, Y., F. Chen, T. Warner, and J. Basara, 2006: Verification of a mesoscale data-assimilation and forecasting system for the Oklahoma city area during the Joint Urban 2003 field project. *J. Appl. Meteor. Climatol.*, **45**, 912–929.

Martilli, A., A. Clappier, and M. Rotach, 2002: An urban surface exchange parameterisation for mesoscale models. *Bound.-Layer Meteor.*, **104**, 261–304.

Mashiko, W., H. Niino, and T. Kato, 2009: Numerical Simulation of Tornadogenesis in an Outer-Rainband Minisupercell of Typhoon Shanshan on 17 September 2006. *Mon. Wea. Rev.*, **137**, 4238–4260.

Masson, V., 2000: A physically-based scheme for the urban energy budget in atmospheric models. *Bound.-Layer Meteor.*, **94**, 357–397.

Masson, V., C. Grimmond, and T. Oke, 2002: Evaluation of the town energy balance (TEB) scheme with direct measurements from dry districts in two cities. *J. Appl. Meteor.*, **41**, 1011–1026.

Matheson, M. and Y. Ashie, 2008: The effect of changes of urban surfaces on rainfall phenomenon as determined by a non-hydrostatic mesoscale model. *J. Meteor. Soc. Japan*, **86**, 733–751.

Montávez, J., J. González-Rouco, and F. Valero, 2008: A simple model for estimating the maximum intensity of nocturnal urban heat island. *Int. J. Climatol.*, **28**, 235–242.

Moriwaki, R. and M. Kanda, 2004: Seasonal and diurnal fluxes of radiation, heat, water vapor and carbon dioxide over a suburban area. *J. Appl. Meteor.*, **43**, 1700–1710.

Ohashi, Y., Y. Genchi, H. Kondo, Y. Kikegawa, and Y. Hirano, 2007: influence of air-conditioning waste heat on air temperature in Tokyo during summer Numerical experiments

using an urban canopy model coupled with a building energy model. *J. Appl. Meteor. Climatol.*, **46**, 66–81.

Oke, T., G. Johnson, G. Steyn, and I. Watson, 1991: Simulation of surface urban heat islands under 'ideal' conditions at night part 2: diagnosis of causation. *Bound.-Layer Meteor.*, **56**, 339–358.

Oliveira Panão, M., H. Gonçalves, and P. Ferrão, 2007: A matrix approach coupled with Monte Carlo techniques for solving the net radiative balance of the urban block. *Bound.-Layer Meteor.*, **122**, 217–241.

Onogi, K., et al., 2007: The JRA-25 reanalysis. *J. Meteor. Soc. Japan*, **85**, 369–432.

Otte, T., A. Lacser, S. Dupont, and J. Ching, 2004: Implementation of an urban canopy parameterization in a mesoscale meteorological model. *J. Appl. Meteor.*, **43**, 1648–1665.

Ratti, C., S. Di Sabatino, and S. Britter, 2012: Urban texture analysis with image processing techniques: winds and dispersion. *Theor. Appl. Climatol.*, **84**, 77–90.

Ratti, C., S. Di Sabatino, S. Britter, M. Brown, F. Caton, and S. Burian, 2002: Analysis of 3-D urban databases with respect to pollution dispersion for a number of European and American cities. *Water Air Soil Pollut. : Focus*, **2**, 459–469.

Saito, K., J. Ishida, K. Aranami, T. Hara, T. Segawa, M. Narita, and Y. Honda, 2007: Nonhydrostatic atmospheric models and operational development at JMA. *J. Meteor. Soc. Japan*, **85B**, 271–304.

Saito, K., et al., 2006: The operational JMA nonhydrostatic mesoscale model. *Mon. Wea. Rev.*, **134**, 1266–1298.

Sakakibara, Y., 1996: A numerical study of the effect of urban geometry upon the surface energy budget. *Atmos. Environ.*, **30**, 487–496.

Sasaki, H. and K. Kurihara, 2008: Preliminary experiments of reproducing the present climate using he non-hydrostatic regional climate model. *SOLA*, **4**, 25–28.

Seino, N., H. Sasaki, J. Sato, and M. Chiba, 2004: High-resolution simulation of volcanic sulfur dioxide dispersion over the Miyake Island. *Atmos. Environ.*, **38**, 7073–7081.

Senoo, H., M. Kanda, T. Kinouchi, and A. Hagishima, 2004: Estimation of anthropogenic heat and vapor emission, and the impact on local meteorology. *Ann. J. Hydr. Eng.*, **48**, 160–174, (in Japanese).

Siegel, R. and J. Howell, 1981: *Thermal radiation heat transfer.* Hemisphere Publishing Corporation, New York, 862 pp.

Sparrow, E. and R. Cess, 1978: *Radiation heat transfer.* Hemisphere Publishing Corporation, Washington, DC, 306 pp.

Sugawara, H. and T. Takamura, 2006: Longwave radiation flux from an urban canopy: evaluation via measurements of directional radiometric temperature. *Remote Sens. Environ.*, **104**, 226–237.

Tokyo Metropolitan government, 1977: *A summary of urban planning 1976 (Toshi Keikaku Gaiyou 1976).* Tokyo Metropolitan government, 336 pp., (in Japanese).

Yabu, S., S. Murai, and H. Kitagawa, 2005: Clear-sky radiation scheme. *Separate volume of annual report of NPD*, Japan Meteorological Agency, Vol. 51, 53–64, (in Japanese).

Zhang, H., N. Sato, T. Izumi, K. Hanaki, and T. Aramaki, 2008: Modified RAMS-urban canopy model for heat island simulation in Chongqing, China. *J. Appl. Meteor. Climatol.*, **47**, 509–524.